

JUACEP Summer Program 2016 at Nagoya University



Japan-US Advanced Collaborative Education Program

Nagoya University

Table of Contents

<1> About the Program

(a) Overview	-----	4
(b) Participants	-----	5
(c) Schedule	-----	6

<2> Classes & Events

(a) Japanese Course Syllabus	-----	8
(b) Hands-on Exercise	-----	10
(c) Tour for the Disaster Mitigation Research Center		11
(d) Meet-up for JUACEP Students	-----	12
(e) Field Trip	-----	13
(f) Research Internship -Research Reports-	-----	14
(g) The 17 th JUACEP Workshop –Presentations-	-----	71

<3> Reports and Questionnaires on JUACEP

(a) Findings through JUACEP	-----	98
(b) Questionnaires	-----	107

<4> Appendix

(a) Photo Collection	-----	112
(b) Handout Materials	-----	117

<1> About the Program

- (a) Overview
- (b) Participants
- (c) Schedule

(a) Overview

Summer 10-week course 2016 for the students of University of Michigan and UCLA

Duration: June 17 – August 26, 2016

Research presentations: The 17th JUACEP Workshop on August 26, 2016

This program was designed for graduate students at University of Michigan and at University of California, Los Angeles.

Each participant chose a laboratory at Nagoya University according to his/her research interest and carried out a research project with the lab members under the supervisor. At the same time most of them attended the Japanese language class, the hands-on engine assembly course and some special lectures organized by the program.

During the program period, they took part in the labs' events such as seminars, sessions, trips, casual parties, and so on. Teaching assistants assigned by the program supported the participants not only in researches but also in daily life.

At the end of the program, they submitted the research report and gave the final presentation at the workshop. Based on the evaluations by the supervisors, the students earned 2-3 credits, which will be transferred as graduation credits for UM students.



Orientation at ES Building on June 17, 2016

(b) Participants

	Name	Adviser & Teaching Assistant at NU
1	Chih-Kang CHAN Robotics, University of Michigan	Prof. Yasuhisa HASEGAWA TA: Yuichiro SATO (Micro-Nano Systems Engineering)
2	Sandeep Kumar INGERSAL Global Automotive and Manufacturing Engineering, University of Michigan	Prof. Eiji SHAMOTO TA: Hidenori IGETA (Mechanical Science and Engineering)
3	Xiaojin SHEN Nuclear Engineering and Radiological Science, University of Michigan	Prof. Youichi ENOKIDA TA: Seo UCHIMURA (Quantum Science and Energy Engineering)
4	Carlos Alberto GAMEZ VILLEGAS Mechanical and Aerospace Engineering, UCLA	Assoc. Prof. Yasuyuki MORITA TA: Takuma WAKIMOTO (Mechanical Science and Engineering)
5	Chen-Hsi HUANG Materials Science and Engineering, UCLA	Assoc. Prof. Wataru SHINODA TA: Yusuke MIYAZAKI (Applied Chemistry)
6	Raymond Niko ROMAN Mechanical Engineering, UCLA	Assoc. Prof. Yasumasa ITO TA: Taichi GOYODANI (Mechanical Science and Engineering)
7	Itsui YAMAYOSHI Mechanical Engineering, UCLA	Prof. Tatsuya SUZUKI TA: Hyuntai CHIN (Mechanical Science and Engineering)
8	Matthew Aung YEE Materials Science and Engineering, UCLA	Prof. Yutaka OHNO TA: Fu Wen TAN (Electrical Engineering)
9	Bonan ZHOU Mechanical and Aerospace Engineering, UCLA	Prof. Susumu HARA TA: Takamasa HORIBE (Aerospace Engineerig)

Japanese Course Instructor

Ms. Sumie YASUI
TA: Shun ARAKANE

Coordinators of Partner Universities

Prof. Katsuo KURABAYASHI
Mechanical Engineering, University of Michigan

Prof. Jenn-Ming YANG
Materials Science and Engineering, UCLA

JUACEP Members

Prof. Noritsugu UMEHARA
Mechanical Science and Engineering

Prof. Yang JU
Mechanical Science and Engineering

Assoc. Prof. Yasumasa ITO
Mechanical Science and Engineering

Tomoko KATO
Administrative staff

(c) JUACEP Summer Program 2016 Schedule

Day	Date	8:45-10:15	10:30-12:00	13:00-14:30	14:45-16:00	16:15-
1	June 16	Thu	Arrival at International Residence Yamate			
2	June 17	Fri	10:20 Reception, 11:00 Orientation @ ES Meeting Room	Welcome Lunch	13:00 Stipend @ ES Meeting Room	Lab introduction @ each Lab
3	June 18	Sat				
4	June 19	Sun				
5	June 20	Mon	Research at Lab		Research at Lab	
6	June 21	Tue	Japanese Class① @ EB-3, 441		Disaster Mitigation Research Center	
7	June 22	Wed	Research at Lab		Research at Lab	
8	June 23	Thu	Japanese Class② @ EB-3, 441		Research at Lab	
9	June 24	Fri	Research at Lab		Research at Lab	
10	June 25	Sat				
11	June 26	Sun				
12	June 27	Mon	Research at Lab		Research at Lab	
13	June 28	Tue	Japanese Class③ @ EB-3, 441		Research at Lab	
14	June 29	Wed	Field Trip (Toyota Kaikan Museum, Toyota Factory, Railway Park Museum)			
15	June 30	Thu	Japanese Class④ @ EB-3, 441		Research at Lab	
16	July 1	Fri	Research at Lab		Research at Lab	
17	July 2	Sat				
18	July 3	Sun				
19	July 4	Mon	Research at Lab		Research at Lab	
20	July 5	Tue	Japanese Class⑤ @ EB-3, 441		Research at Lab	
21	July 6	Wed	Research at Lab		Research at Lab	Meet-up, #347, EB-2, 3F
22	July 7	Thu	Japanese Class⑥ @ EB-3, 441		Research at Lab	
23	July 8	Fri	Research at Lab		Hands-on Exercise A @ EB-N Creation Plaza, 10F	
24	July 9	Sat				
25	July 10	Sun				
26	July 11	Mon	Research at Lab		Research at Lab	
27	July 12	Tue	Japanese Class⑦ @ EB-3, 441		Research at Lab	
28	July 13	Wed	Research at Lab		13:00 Stipend @ ES 031	Research at Lab
29	July 14	Thu	Japanese Class⑧ @ EB-3, 441		Research at Lab	
30	July 15	Fri	Research at Lab		Hands-on Exercise B @ EB-N Creation Plaza, 10F	
31	July 16	Sat				
32	July 17	Sun				
33	July 18	Mon	Marine Day			
34	July 19	Tue	Japanese Class⑨ @ EB-3, 441		Research at Lab	
35	July 20	Wed	Research at Lab	UMich. Meeting	Research at Lab	
36	July 21	Thu	Japanese Class Final @ EB-3, 441		Research at Lab	
37	July 22	Fri	Research at Lab		Research at Lab	
38	July 23	Sat				
39	July 24	Sun				
40	July 25	Mon				
41	July 26	Tue				
42	July 27	Wed	Research at Lab		Research at Lab	
43	July 28	Thu				
44	July 29	Fri				
45	July 30	Sat				
46	July 31	Sun				
47	August 1	Mon				
48	August 2	Tue				
49	August 3	Wed	Research at Lab		Research at Lab	
50	August 4	Thu				
51	August 5	Fri				
52	August 6	Sat				
53	August 7	Sun				
54	August 8	Mon	Research at Lab		Research at Lab	
55	August 9	Tue	Research at Lab		Research at Lab	
56	August 10	Wed	Research at Lab		13:00 Stipend @ ES 031	Research at Lab
57	August 11	Thu	Mountain Day			
58	August 12	Fri	Research at Lab		Research at Lab	
59	August 13	Sat				
60	August 14	Sun				
61	August 15	Mon	Bon Holidays			
62	August 16	Tue				
63	August 17	Wed				
64	August 18	Thu	Research at Lab		Research at Lab	
65	August 19	Fri				
66	August 20	Sat				
67	August 21	Sun				
68	August 22	Mon				
69	August 23	Tue	Research at Lab		Research at Lab	
70	August 24	Wed				
71	August 25	Thu				
72	August 26	Fri	Research at Lab		17th Workshop @ NIC Meeting Room, 3F	Farewell Party (TBD)
73	August 27	Sat	Departing Nagoya University			

JUACEP event
Japanese class
Stipend payment
Holiday

<2> Classes and Events

- (a) Japanese Course Syllabus
- (b) Hands-on Exercise
- (c) Tour for the Disaster Mitigation Research Center
- (d) Meet-up for JUACEP Students
- (e) Field Trip
- (f) Research Internship ---Research Reports
- (g) The 17th JUACEP Workshop ---Presentations

(a) Japanese Course Syllabus

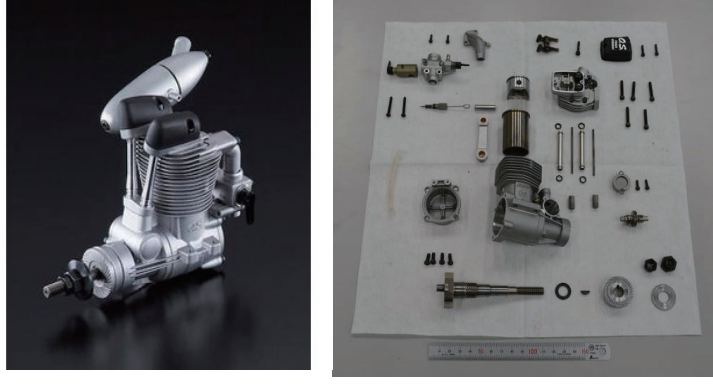
Course name	Japanese Language		
Teaching staff	Ms. YASUI Sumie		
Course period	June 21 - July 21, 2016		
Weekly timetable	Tuesday & Thursday 1st (45 min) & 2nd period (90 min) (9 : 40-12 : 00)		
Classroom	#3 Engineering Building, room 441 (4 th floor, EB-3)		
Textbook	<p>“GENKI, An Integrated Course in Elementary Japanese” I (The Japan Times)</p> <p>This textbook is a comprehensive approach to developing the four basic language skills (listening, speaking, reading and writing) in order to cultivate overall Japanese-language ability. *Some teaching material will be given in class.</p>		
Course Contents	<p>Course outline</p> <p>The purpose of this course is to introduce the most essential Japanese words and expressions for everyday life. Students will learn writing system (Hiragana & Katakana), the basic grammar, expressions of Japanese.</p> <p>Classroom activities</p> <p>Basic communication skills required in everyday life will be taught by introducing new vocabulary, new grammar, and practicing listening, conversation and role-playings.</p> <p>Homework and Quiz</p> <p>You are expected to submit your homework by the deadline. Quizzes will be given every day in class.</p> <p>1. Hiragana 2. Katakana 3. Dictation 4. Conjugation</p>		
Evaluation	1. Homework	20%	S=100-90
	2. Quizzes	30%	A=89-80
	3. Oral exam.	50%	B=79-70
		100%	C=69-60
	More than 80% attendance is required.		F(fail)=59-0
	You will be officially awarded 1 credit of Nagoya University.		

Course
schedule

1. 6/21(Tue)
Greeting Expressions, Hiragana 1
Introducing yourself, Noun sentences 1, Occupation,
Nationality, Age, Numbers 1-100
2. 6/23(Thu)
Classroom expressions, Hiragana 2
Shopping, Noun sentences 2, Price, Numbers 101-1,000,000
3. 6/28(Tue)
Hiragana 3
Describing where things are, Locations
Placing an order at a restaurant
4. 6/30(Thu)
Hiragana 4
Talking about your daily life
Verbal sentences 1, Time reference, Adverbs
5. 7/5(Tue)
Hiragana 5
Invitations, Suggestions, Desires
Verbal sentences 2, Days/Weeks/Months/Years, Counting
6. 7/7(Thu)
Katakana 1
Talking about your family
Adjectives, Likes or Dislikes, Degree expressions, Family terms
7. 7/12(Tue)
Katakana 2
Talking about your week-end, Past tense, Time words
8. 7/14(Thu)
Katakana 3
Making a request (Verb-Te-form), Progressive actions,
Describing your status
9. 7/19(Tue)
Asking permission, Prohibition, Negative request
Describing two things
Talking about your interests
Plain form
10. 7/21(Thu)
The Final Examination (speaking)

(b) Hands-on Exercise

“Disassembly and Assembly of Internal Combustion Engine”



Group A: July 8, Fri	Sandeep Kumar	Xiaojin Shen
Chih-Kang Chan	Raymond Roman	Chen-Hsi Huang

Group B: July 15, Fri	Bonan Zhou	Carlos Gamez
Itsui Yamayoshi	Matthew Yee	

Time: 13:00 – 16:00

Place: Creation Plaza, 10th floor of IB-North

Staff: Prof. Yasuhiko Sakai, Director of Creation Plaza

Asst. Prof. Kaneko Kazue, Creation Plaza

Technical staff.... Koji Yamamoto, Masafumi Nakakimura,

Shintaro Goto, Kiyonori Saito, and others

Contents:

- Opening remarks
- Introduction to the basis of the Internal Combustion Engine and other engines
(History, Characteristics, Operation principle, Practice engines)
- Disassembling → Assembling → Adjustment
- Performance test and Jet engine demonstration
- Discussion

(c) Tour for Disaster Mitigation Research Center

Meet at the entrance of DMRC building 13:00, June 21, Tuesday



About the Disaster Mitigation Research Center (DMRC)

The Disaster Mitigation Research Center (DMRC), Nagoya University, was founded in January 2012. Nagoya City and the surrounding Chukyo area are vulnerable to natural hazard risks, particularly colossal earthquakes along the Nankai Trough plate boundary. The Japanese government estimates that there is a 60-70 % chance of a massive earthquake occurring during the next 30 years. The area also has a history of damaging floods and storms. Since this area is the center of industrial production in Japan, the natural hazard risks have the potential to cause a serious crisis at the national level. The DMRC brings together experts from various academic fields, such as engineering, earth science, social science, and humanities as a means of promoting cooperative multidisciplinary research aimed at developing and applying a state-of-the-art disaster mitigation model to ensure that the local community is safe and secure. The DMRC provides a cooperative framework for local government, companies, and citizens to improve the preparedness of the local community for future natural hazards. In addition, the DMRC offers disaster mitigation training courses for local public officers and volunteers. The Disaster Mitigation Research Building (Gensai-kan) where the DMRC is located has an exhibition hall and a library, which offer the public information about natural disasters and their mitigation.

(d) Meet-up for JUACEP Students



ROUND-TABLE DISCUSSION FOR JUACEP STUDENTS

16:00- WED, JULY 6, 2016

AEROSPACE MTG ROOM #347, 3F EB-2

Let's meet up to get info for the life of study abroad!

- ★ *To reduce anxieties of your life abroad*
- ★ *To know what you need for the beginning of your life abroad*
- ★ *To have dependable friends in your life abroad...*

Inquiry to JUACEP Office: juacep-office@engg.nagaoya-u.ac.jp
Phone 052-789-2799 (内線 2799)

(e) Field Trip

Date: June 29, Wednesday

Escorts: Asst. Prof. Takehiro Hayasaka
Tomoko Kato, JUACEP



Visiting spots:

- Toyota Kaikan Museum
http://www.toyota.co.jp/en/about_toyota/facility/toyota_kaikan/museum/
- Toyota Motor Factory
http://www.toyota.co.jp/en/about_toyota/facility/toyota_kaikan/index.html
- SCMAGLEV and Railway Park
<http://museum.jr-central.co.jp/en/>
- BBQ (dinner)

Schedule:

Time	Event	Transportation
9:10	Meeting at Toyoda Auditorium	
9:20	Departure from Nagoya University	Hired bus
10:30	Toyota Kaikan Museum	
11:00	Toyota Factory	
13:00	Leaving Toyota and Lunch in the bus	Hired bus
13:40	SCMAGLEV and Railway Park	
17:00	Leaving the Park	Hired bus
17:30	BBQ at Yanagibashi	
19:30	Breakup at Nagoya Station	

*Schedule above is tentative and may be changed.

*Wear sports shoes for safety of Toyota factory tour.

*Photo is not allowed in the factory.



(f) Research Internship ---Research Reports

Page	Name	Report title	Adviser at Nagoya Univ.
15	Chih-Kang CHAN	Intuitive User Interface for Surgical Tool Operation	Prof. Yasuhisa Hasegawa <i>Micro-Nano Systems Engineering</i>
20	Sandeep INGERSAL	Effect of Direction of Cutting on Mode-Coupling Chatter Stability in Milling	Prof. Eiji Shamoto <i>Mechanical Science and Engineering</i>
25	Xiaojin SHEN	Experimental and Computational Analyses for the Molten Borosilicate Glass with/without Crystalline Materials	Prof. Youichi Enokida <i>Quantum Science and Energy Engineering</i>
33	Carlos GAMEZ	Temperature Dependent Thermal-Electrical-Structural Finite Element Analysis around Crack Tip under High Current Density Electropulsing	Assoc. Prof. Yasuyuki Morita <i>Mechanical Science and Engineering</i>
39	Chen-Hsi HUANG	Mechanical Properties of Lipid Vesicle Studied by Molecular Dynamics Simulations (Undisclosed)	Assoc. Prof. Wataru Shinoda <i>Applied Chemistry</i>
40	Raymond ROMAN	Investigation of Time-Dependent Hemodynamics in Stented and Unstented	Assoc. Prof. Yasumasa Ito <i>Mechanical Science and Engineering</i>
49	Itsui YAMAYOSHI	Path Tracking Using LIDAR Localization and Mapping	Prof. Tatsuya Suzuki <i>Mechanical Science and Engineering</i>
54	Matthew YEE	Carbon Nanotube Thin Film Transistors on Flexible Plastic Films	Prof. Yutaka Ohno <i>Electrical Engineering</i>
58	Bonan ZHOU	Estimation of the Region of Attraction for Optimization of Design Parameters in Nonlinear Control Systems	Prof. Susumu Hara <i>Aerospace Engineerig</i>

INTUITIVE USER INTERFACE FOR SURGICAL TOOL OPERATION

Chang Chih-Kang

Robotics Program, University of Michigan
chihkang@umich.edu

Supervisor: Prof. Hasegawa Yasuhisa

Department of Micro-Nano System Engineering, Nagoya University
hasegawa@mein.nagoya-u.ac.jp

ABSTRACT

The pituitary gland is a small organ, located at the base of the brain, regulating several physiological processes. A tumour in the pituitary gland can cause symptoms such as acromegaly, cushing's disease, or prolactinoma by either releasing too much or too little hormone. It may also cause symptoms such as a visual field defect by pressing the structures surrounding the gland. To remove the tumour, the surgeon works through the nostrils with an endoscope and long instruments in the endonasal approach. The goal of this research is to develop a new robotic neurosurgical tool with an intuitive user interface to assist the surgeon and to provide high precision and dexterity of tool handling during the surgical operation. In this report, we use a haptic device for the user interface to control the surgical tool. The corresponding force feedback is applied on the device to simulate the surgical tool operation. We implement contact force feedback with virtual objects and tool constraint force feedback in a simulated virtual environment. As a result, a basic structure is built and prepared for further development and improvement of our proposed robotic neurosurgical system.

1. INTRODUCTION

1.1 ENDOSCOPIC TRANSNASAL PITUITARY SURGERY

The endoscopic transnasal pituitary surgery is performed through the nose to remove tumours from the pituitary gland and the skull base. In this minimally invasive surgery, the surgeon works through the nostrils with a thin endoscopic camera to remove tumours using long instruments (Fig. 1) [1].

The pituitary gland, located at the base of the brain, is a small organ about the size of an acorn. The pituitary gland is sometimes referred to as the "master gland" because it releases substances which control the basic functions of growth, metabolism, and reproduction. A tumour in the pituitary gland can cause symptoms such as acromegaly, cushing's disease, or prolactinoma by either releasing too much or too little hormone by pressing the gland. A pituitary

tumour may also cause symptoms such as a visual defect by growing and pressing the structures such as the nerves to the eyes surrounding the gland. [2]

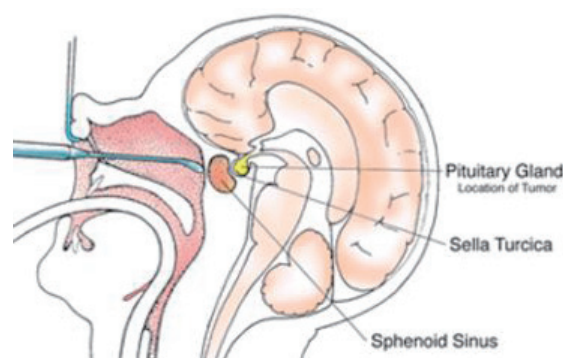


Fig. 1 Endoscopic transnasal pituitary surgery [1]

1.2 ROBOTIC SURGERY

Robotic surgery is an advanced form of minimally invasive or laparoscopic (small incision) surgery where surgeons use a computer-controlled robot to assist them in certain surgical procedures. The robot's "hands" have high degrees of dexterity, providing surgeons with the ability to operate in very tight and narrow spaces in the body that would otherwise only be accessible through open (long incision) surgery.

Compared to open surgery (traditional surgery with long incisions), robotic and minimally invasive surgery typically cause smaller incisions with less pain and scarring, resulting in shorter hospitalization and less risk of infection.

Robotic surgery allows surgeons to perform complex surgical tasks through small incisions using robotic technology. Surgical robots are actuated and computer-controlled devices that can be programmed to aid in the positioning and manipulation of surgical instruments. This provides surgeons with better accuracy, flexibility and control. [3]

1.3 SURGICAL SYSTEM STRUCTURE

Fig. 2 shows a conceptual structure of the robotic surgical system with an intuitive user interface we consider in this research.

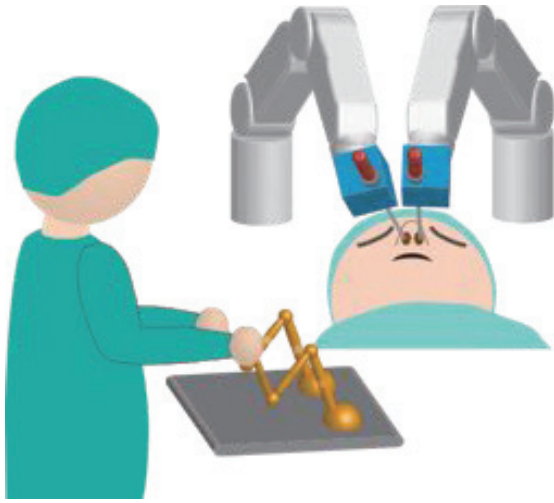


Fig. 2 The robotic surgical tool structure

The robotic surgical tool is controlled with a haptic device. In this research, Phantom Omni (Fig. 3), the device with 6 DoF position sensing and 3 DoF translation force feedback developed by Sensable Technologies, is used due to its easy access and wide application. The device measures the motion of the surgeon's operation including the position and orientation and sends such data to drive the surgical tool. The robotic arm (DENSO VS050 shown in Fig. 4) is controlled by a 3D mouse (Fig. 5) and moved to the desired location before the operation to hold the surgical tool during the surgery. The main topic of this report is the implementation of the haptic device.



Fig. 3 Phantom Omni



Fig. 5 3D Mouse



Fig. 4 DENSO VS050

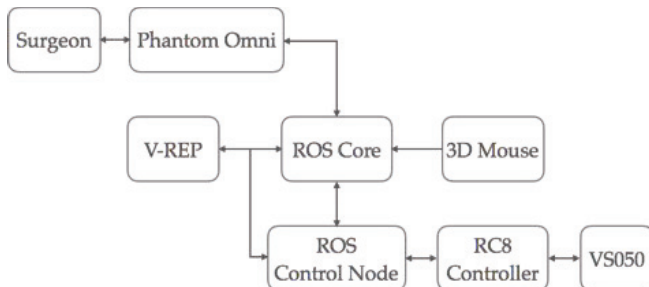


Fig. 6 System architecture of the robotic surgical tool

Fig. 6 shows the system architecture. The ROS (Robot Operating System) core is the main data exchange platform. The ROS is a flexible framework for developing robot software. It is a collection of tools, libraries, and conventions that aim to simplify the task of creating complex and robust robot behavior across a wide variety of robotic platforms [4]. The data can be published to a channel with a ROS publisher, and a ROS subscriber can subscribe to the data from the channel. Thus cross-platform communication can easily be possible and straightforward.

To simulate the robotic system, we use V-REP as a simulator. V-REP is a robotic simulator with various functions, features, and elaborated APIs. With an integrated development environment, it is based on a distributed control architecture: each object/model can be individually controlled via an embedded script, a plugin, a ROS node, a remote API client, or a custom solution. [5]

The surgeon operates Phantom Omni with force feedback which makes the operation precise and intuitive. The data from Phantom Omni and 3D mouse are sent to ROS core and the configurations of the virtual robotic tool in V-REP are updated accordingly. After the dynamic calculation, V-REP sends the control parameters to the ROS control node, which controls the controller RC8 for DENSO VS050.

2. METHOD

2.1 VIRTUAL OBJECT

To achieve intuitive and precise operation, a sense of touch is desirable for the surgeon. When operating the haptic device, providing force feedback would be beneficial so that the surgeon could feel the tool touching the tissues to avoid overreaching. Since the actual tool and force sensor are not implemented yet, a virtual object is built and tested for haptic feedback.

It is usual to model an object in a finite number of elements based on its local property. A mass-and-spring lattice represents an elastic object, which is effective if the variety of generated motion is limited and computation time is available [6]. In this research, the simplest model is adopted. The surface of object is modeled as a spring which generates a force proportional to the penetration distance and normal to the surface (Fig. 7).

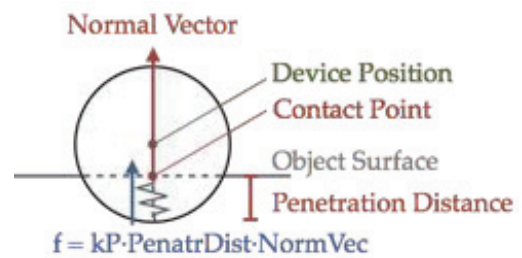


Fig. 7 Spring model of virtual object

2.2 TOOL CONSTRAINT

Besides a sense of touch, the haptic device needs to simulate the preferred movement of the surgical tool with constrained degrees of freedom (DoFs). With 3 orientational DoFs and 1 translational DoF, the surgical tool can rotate freely around a pivot and translate along the direction as shown in Fig. 8. Since Phantom Omni had 6 DoFs, specific constraints had to be added to keep the position and orientation of Phantom Omni in the range of workspace of the surgical tool.

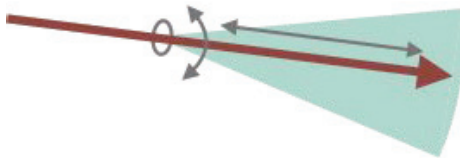


Fig. 8 DoFs and workspace of the surgical tool

As shown in Fig. 9, a spring model is used to implement such constraint. The penetration distance is defined as the distance from the “pivot” point to the “close” point. The close point is the closest point on the extended line of the device to the pivot point, i.e., it is the point projected from the pivot point on the line passing through the device position with the direction of device pointing vector. The normal vector is defined as the vector from the close point to the pivot point.

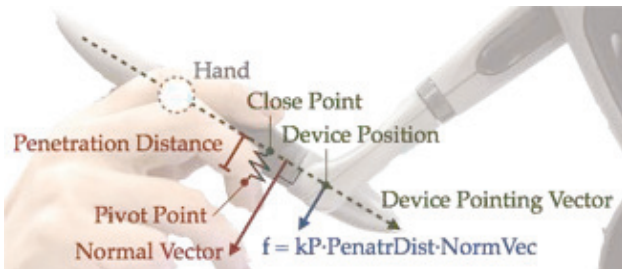


Fig. 9 Tool constraint force feedback

3. EXPERIMENT RESULTS

3.1 VIRTUAL OBJECT

To test the feasibility of the spring model, a cube object is built in the V-REP environment. A sphere is controlled by the Phantom Omni through the ROS node and moved freely in the space (Fig. 10). When the sphere touches the cube, the force is applied according to the spring model. The result of the force applied according to the penetration distance (“depth” for short, same in the following paragraphs) is shown in Fig. 11.

As observed in Fig. 11, the resultant virtual contact force is not continuous and the operator felt bumpy when moving around on the surface. The reason is that the update rate of V-REP providing the contact point, normal vector and the depth (red items in Fig. 7) is around 35-50 ms per loop in this project due to dynamic and graphical calculation, while the update rate of Phantom Omni is

around 1 ms per loop. Since the depth is kept at the same value of the last update but not the actual depth, the value of depth instantly changes when it is updated.

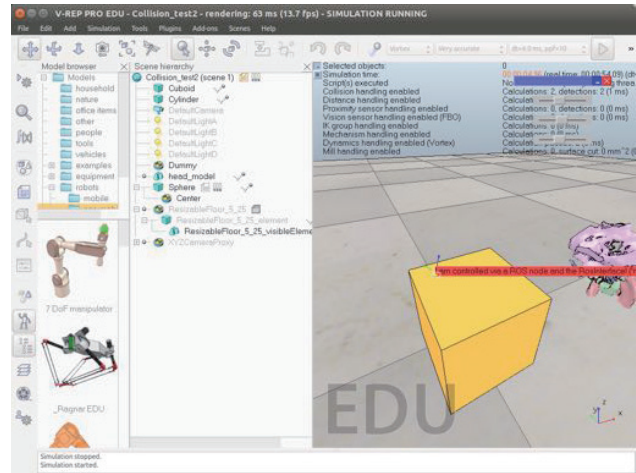


Fig. 10 V-REP environment

To resolve the problem, the depth should be updated according to the device position. However, the contact point and the normal vector are not provided at every control loop of Phantom Omni since the object model is built in V-REP with a slower update rate. In order to improve the response of force feedback, we assume that the surface is flat when the device moves around. As shown in Fig. 12, the “deep” point can be calculated with the device position, normal vector and radius of the sphere. An estimated depth is then calculated by projecting the vector from the deep point to the contact point on the normal vector. The result of the force response is shown in Fig. 13. The force profile is continuous and the operator could feel the surface in a smooth manner.

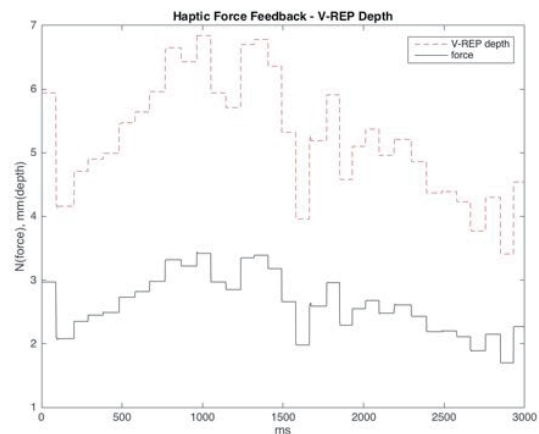


Fig. 11 Force and depth

After this initial testing, a skull model is imported and tested in V-REP (Fig. 14). The result is shown in Fig. 15. The resultant force is not continuous because the surface of the skull model is not flat and the updated contact point and normal vector do not exactly match the estimated ones.

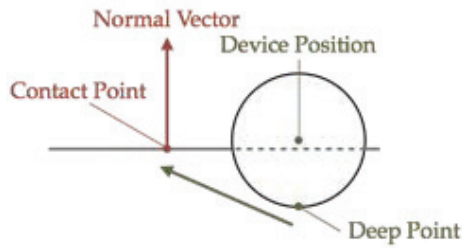


Fig. 12 Estimated depth with flat surface assumption

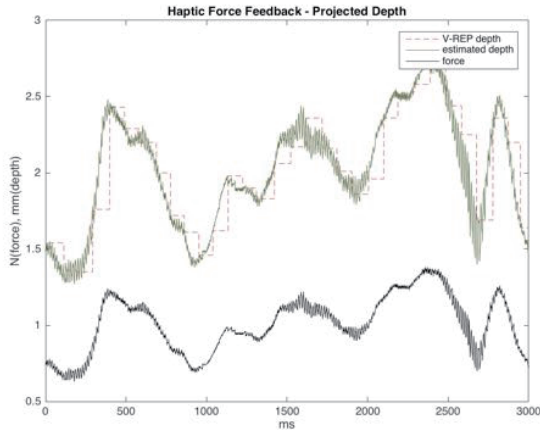


Fig. 13 Force and estimated depth

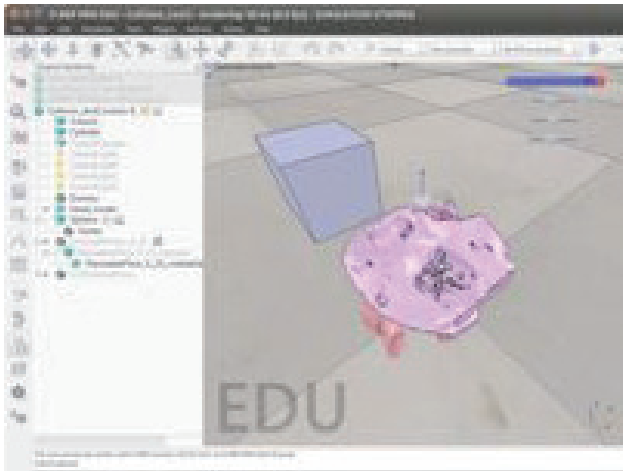


Fig. 14 Skull model in V-REP

3.2 TOOL CONSTRAINT

The test result of the tool constraint presented in Section 2.2 is shown in Fig. 16, where the parallel distance indicates the distance from the close point to the device position in Fig. 9. The penetration distance is less than 5 mm and the operator felt that the device could only move around the virtual pivot.

However, when the parallel distance is negative, i.e., the device is pulled backward behind the pivot point, the device becomes unstable and moves in an oscillatory manner. As shown in Fig. 17, when the device is beyond the pivot, the distance from operator's hand, which is relatively stable, to the close point is shorter than the distance to the device

position, where the force is applied. Thus when the force is applied, having operator's hand as the fulcrum, the close point with shorter lever arm moves less than what is needed. On the other hand, when the device is behind the pivot, the distance from operator's hand to the close point is longer than the distance to device position. Thus when the force is applied, the close point with longer lever arm moves more than what is needed and starts bouncing.

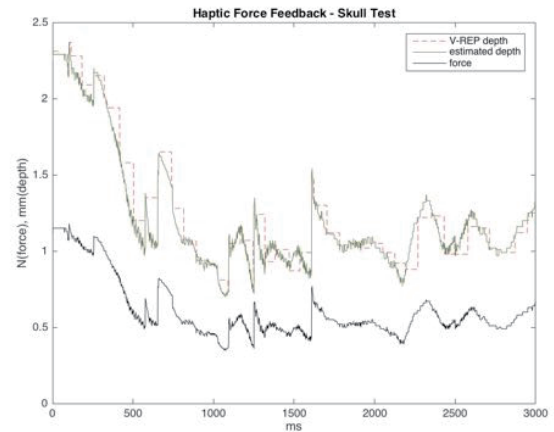


Fig. 15 Force and estimated depth on skull model

To solve the problem, instead of keeping the tool constraint, a new constraint is added when the device is pulled behind the pivot. When the device is behind pivot, a force is applied to pull the device back to the pivot. As a result, the device can not be pulled behind pivot and it stops there to avoid instability.

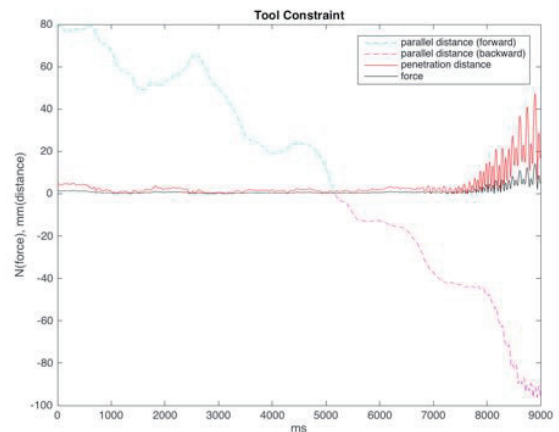


Fig. 16 Result of tool constraint implementation

4. DISCUSSION

The research has focused on the implementation of haptic device as an intuitive user interface for surgical tool operation. We applied a spring model and successfully created haptic force feedback which helped the user feel the virtual object. We also added a constraint to the haptic device and simulated the tool movement with constrained

DoFs. Combining these two, the user could fully control the surgical tool with the haptic device.

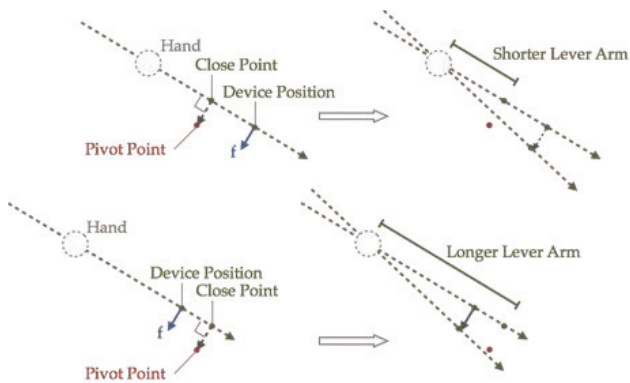


Fig. 17 Response when the device was beyond/behind the pivot

Nevertheless, further improvement will be necessary. As discussed in Section 3.1, the haptic feedback was not smooth and continuous on a curved surface. It could be improved by sending more information about object models, such as local shape and curvature, to the haptic device to obtain an accurate estimation between the updates of V-REP. In addition, in this report, only one contact point was considered when touching the object. However, especially when the tool is in the nasal cavity, there could be multiple contact points. Therefore, in order to address this issue, further investigation and testing will be needed.

As to the tool constraint implementation, despite that the device were to simulate the DoFs of the tool, the user did not feel like operating the tool because the device moved too freely to imagine there was a realistic tool. Adding virtual damping and/or other constraints might be effective to achieve more realistic responses.

Beyond the haptic device implementation, to complete the whole system of our surgical tool system, the robotic arm and the tool should be combined and they should be controlled individually with 3D mouse and haptic device. The frame translation would be applied to integrate different components. Once working system integration is completed in the virtual environment, one could start testing on the actual surgical tool system. Surgeon's opinion should also be included to improve the interface.

ACKNOWLEDGEMENTS

This research was supported by Japan-US Advanced Collaborative Education Program. I would like to thank Prof. Hasegawa Yusuhisa and Prof. Nakanishi Jun who provided advice on this research with expertise and made the research possible. I would also like to thank Jacinto Enrique Colan Zaita for his assistance with code development and V-REP simulation, and Sato Yuichiro for his assistance with mechanical design and lab affairs.

REFERENCES

- [1] Mayfield Clinic, Endoscopic pituitary surgery (transsphenoidal), <http://www.mayfieldclinic.com/PE-EndoPitSurg.htm>
- [2] Lillian S. Wells, Pituitary Tumors, <http://neurosurgery.ufl.edu/patient-care/diseases-conditions/pituitary-tumors/>
- [3] University of Cincinnati Medical Center, Benefits of Robotic Surgery, <http://uhealth.com/services/robotic-surgery/patient-information/benefits/>
- [4] ROS official website, <http://www.ros.org/about-ros/>
- [5] v-rep official website, <http://www.coppeliarobotics.com/>
- [6] Shinya MIYAZAKI, Takami YASUDA, Shigeki YOKOI, and Junichiro TORIWAKI, Modeling and Implementation of Elastic Object Manipulation in Virtual Space, Electronics and Communications in Japan Part 3: Fundamental Electronic Science, pp.1919-1926 (1998)

Effect of Direction of Cutting on Mode-Coupling Chatter Stability in Milling

Sandeep Kumar Ingersal

Department of Integrated Systems + Design, University of Michigan
ingersal@umich.edu

Professor Eiji Shamoto

Department of Mechanical Science and Engineering
Graduate School of Engineering, Nagoya University
shamoto@mech.nagoya-u.ac.jp

Associate Professor Takehiro Hayasaka

Department of Mechanical Science and Engineering
Graduate School of Engineering, Nagoya University
takehiro-h@upr.mech.nagoya-u.ac.jp

Abstract

Manufacturing of automotive dies and moulds, requires deep and narrow groove milling which is performed using long and slender end mills. These end mills are prone to chatter vibration due to regenerative and mode-coupling effect. Many studies have been carried in the control of regenerative chatter, but not in suppressing mode-coupling chatter. In this study, the regenerative chatter is controlled by a conventional method using variable end-mill pitch cutter and it concentrates on the dynamics of mode-coupling chatter in milling. This paper analysis the variation in the stability limit for the change in the direction of cutting. The proposed study is verified analytically and the analytical results are experimentally validated.

Introduction

In order to reduce the weight and material consumption, thin and tall ribs are used in many parts. This results in the need of deep and narrow groove milling to manufacture its dies and moulds. Due to long and slender end mills used in performing this operation, chatter vibration occurs and leaves a non-smooth surface on the milling surface. For a certain machine-tool-workpiece combination, the main factors that affect the removal rate are axial and radial depth of cut, spindle speed and feed rate. The chatter vibrations are primarily induced by regenerative and mode-coupling effect. There are many proven methods to control regenerative vibration like utilizing variable pitch ends at appropriate conditions [1] [2], by applying the speed difference method in multiple-milling operations [3] etc. Due to asymmetric design of the machine, the dynamics of the system in the X and Y direction varies. This contributes to the stability changes based on the direction of cutting. The technique discussed in this paper suggests the effective direction of milling to reduce the mode-coupling chatter for the considered machine and it also confirms the effect of direct compliance and the cross compliance factors on the stability limit. Milling of a rectangular block workpiece is considered to verify and validate the proposed study.

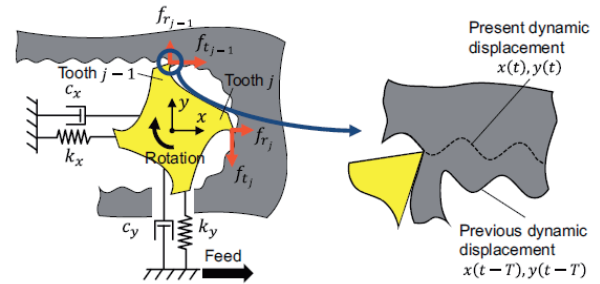


Fig. 1 Schematic illustration of long-shank end milling process with chatter vibration; Source: [1]

Proposed study and analytical prediction

Milling is an intermitted cutting operation having one or more teeth. In deep groove machining, the radial immersion is usually large and the stiffness is nearly equal in both the axis, $K_x \cong K_y$. For example, if there is vibration in the x direction, chip load fluctuates at the j^{th} tooth in Fig. 1. The cutting force varies and excites the slender end mill especially in the y direction, since the tangential force f_{tj} is usually dominant. Then, the vibration in the y direction changes the chip load and the tangential force at the $(j-1)^{\text{th}}$ tooth, and it generates the vibration in the x direction again. Through this closed loop, the vibration grows up easily and generates chatter. The block diagram [5] shows the variables and functions involved in the regenerative and mode-coupling effect.

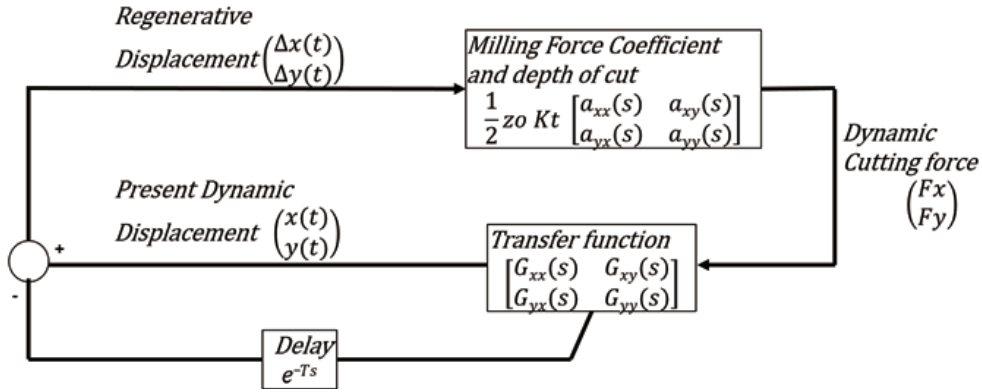


Fig. 2: Block Diagram of regenerative chatter in end milling process

To determine the dynamic displacement of the end mill, the frequency response function or the transfer function (the matrix G in the block diagram) should be determined. The transfer function or the frequency response function is nothing but the displacement per unit force

$$G(s) = \frac{y(s)}{F(s)} \quad (1)$$

where $y(s)$ is the displacement of the end mill, $F(s)$ is the impulse force applied on the end mill. The transfer function is determined by the impulse test. The impulse test was conducted in a static setup with the end mill attached to the spindle. Due to the asymmetric nature of the machine, the frequency response functions G_{xx} and G_{yy} , referred as the direct-compliance factors varies in the X and Y direction. Similarly, the cross-compliance factors G_{xy} and G_{yx} also vary due to the relative effect. The force matrix is obtained by

$$\begin{Bmatrix} F_x \\ F_y \end{Bmatrix} = \frac{1}{2} a K_t \begin{bmatrix} a_{xx} & a_{xy} \\ a_{yx} & a_{yy} \end{bmatrix} \begin{Bmatrix} \Delta x \\ \Delta y \end{Bmatrix} \quad (2)$$

Where $\Delta x(t)$ & $\Delta y(t)$, dynamic displacement of the cutter at the present and previous tooth period, a = axial depth of cut, K_t = cutting force coefficient, $\begin{bmatrix} a_{xx} & a_{xy} \\ a_{yx} & a_{yy} \end{bmatrix}$ = directional dynamic coefficient matrix which is the function of immersion angle ϕ . The transfer function matrix found using impulse test $G(i\omega)$ determines the displacement. The cross compliance factors G_{xy} , G_{yx} have lesser amplitude compared to the direct compliance factors but they carry an effect on the mode-coupling chatter. To study the mode-coupling dynamics, the critical immersion angle is determined to identify the mode-coupling effect region. The immersion angle is related to radial depth of cut. The delay factor e^{-Ts} , generates the regenerative effect due to the phase difference between the waves of the cut created by the current teeth and the

previous teeth. Eliminating the delay factor in the loop provides the critical immersion angle at which the mode-coupling effect begins to occur for a fixed spindle speed. The graph in the Fig. 3 shows the critical immersion angle for the considered end mill.

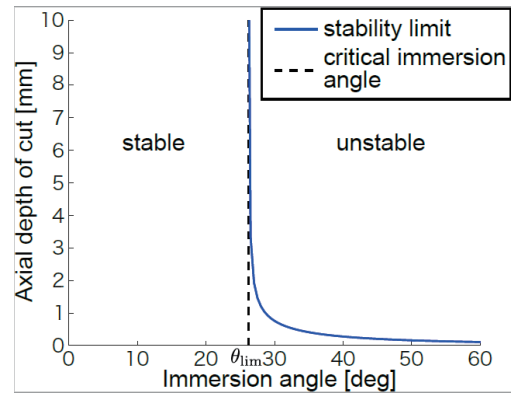


Fig. 3: Critical immersion angle eliminating regenerative chatter

The stability limit is generated by solving the zero order solution equation [5]

$$\det \left\{ [I] - \frac{1}{2} K_t a \sum_{j=0}^{N-1} (1 - e^{-i\omega T_j}) [A_0] [G(s)] \right\} = 0 \quad (3)$$

$\sum_{j=0}^{N-1} (1 - e^{-i\omega T_j})$ represents the delay factor for the variable pitch cutter used in the experiment and $[A_0]$ is the directional dynamic coefficient matrix defined in equation (2). The number of teeth N in the end mill cutter is 2.

Consider milling a rectangular block piece, the direction of cutting changes the orientation of the axis of the cutting tool as shown in the Fig. 4. Two different directions of milling are referred as side and the bottom cut in this paper as seen in the Fig. 4. This alter the transfer function matrix.

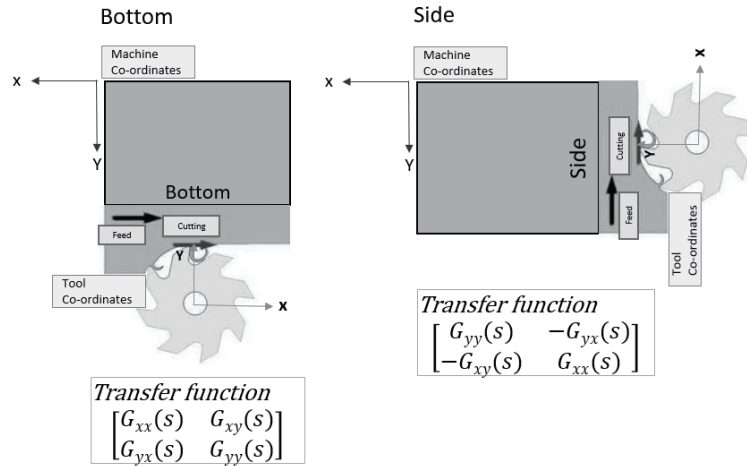


Fig. 4: Schematic representation of side and bottom cut tool axis change and its transfer functions

The direct compliance factors G_{xx} and G_{yy} switches its position in the matrix and the cross-compliance factors G_{xy} and G_{yx} changes its sign and position. The stability limit graphs are generated using the equation (3) for both directions. Since the critical immersion angle determined is 27deg, the stability limit graph is generated for an immersion angle of 40deg where the mode-coupling effect would occur. The stability chart generated analytically shows that the bottom cut has higher stability limit than side cut. For example, for a spindle speed of 5600 rpm, the bottom cut would become unstable after an axial depth of cut of $a = 0.6$ mm and side cut at $a = 0.45$ mm. Change in the stability limit is observed due to change in the transfer function matrix. The cross-compliance factor in the matrix also contributes to the difference in the stability.

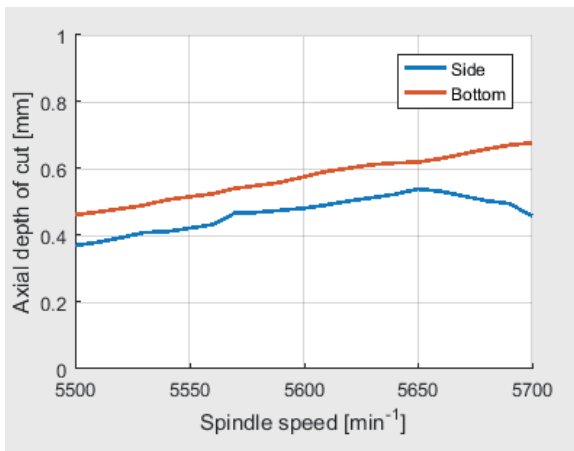


Fig. 5: Stability Limit Graph

Experimental Validation

An experiment is conducted by milling a brass rectangular block to verify the analytical results. A rectangular block is milled in the side and bottom using a variable pitch end mill cutter as seen in the Fig. 6 Fig. 1

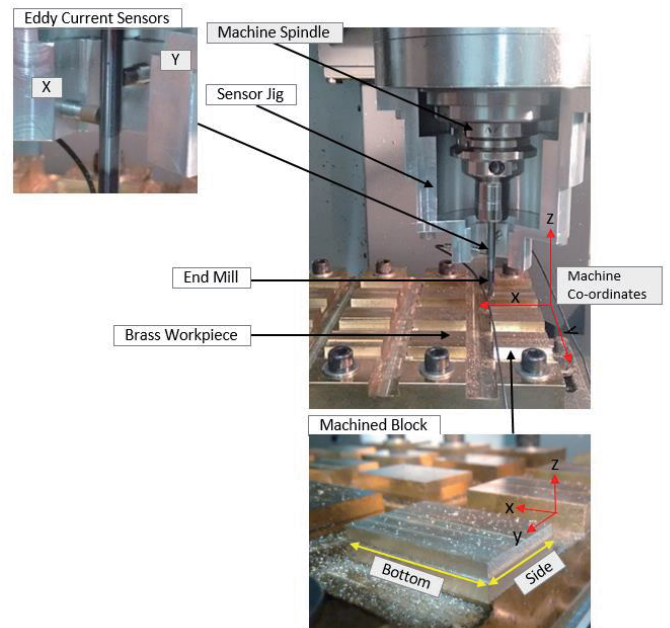


Fig. 6: Experiment Setup

The experiment uses a variable pitch end mill cutter to suppress the regenerative vibration and to concentrate our study on the mode-coupling chatter. The workpiece is milled with an immersion angle of 40deg. The experiment is performed at a spindle speed of 5600 rpm and at a constant feed rate of 342 m/min. Since the immersion angle is kept constant at 40°, the radial depth of cut

remains constant. The axial depth of cut is varied from 0 to 0.6 mm and the frequency response of the vibration is measured. The side, bottom and top surface of the blocks are machined to zero cut before beginning the actual experiment. A special jig is setup over the spindle to mount

the eddy current sensors to measure X and Y direction vibration as shown in the Fig. 7. To compare results, down milling is performed on both side and bottom. The digital oscilloscope is used to capture the response in time domain and are analysed in the frequency domain.

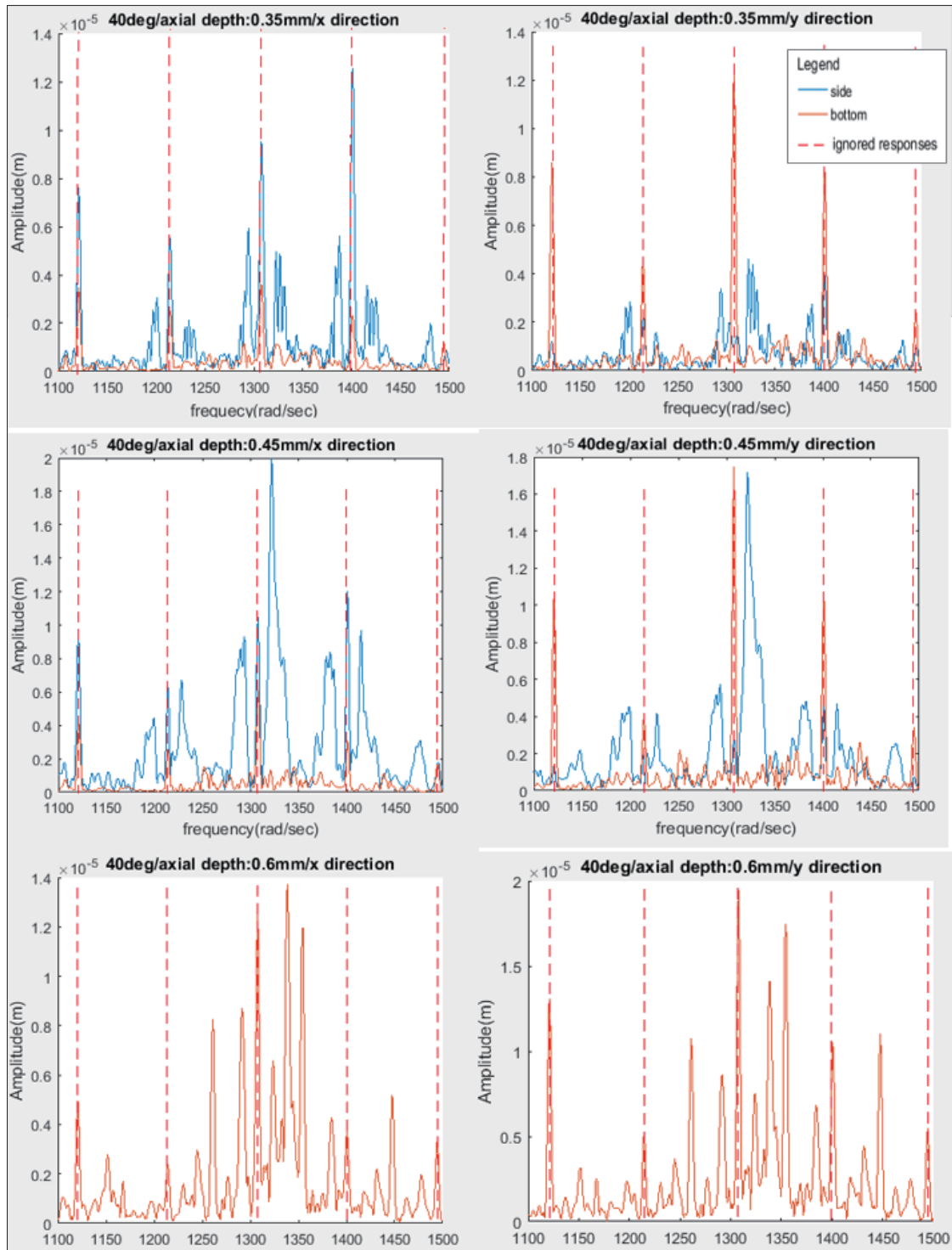


Fig. 7: Frequency response for axial depth of cut for 0.35mm, 0.45mm and 0.6 mm in X and Y direction

Results

The experimental result in Fig. 8 shows the chatter occurrence for different axial depth of cut and Fig. 7 shows the frequency response of the vibration. Our interest lies in analysing the chatter vibration; so the forced vibration responses are ignored in the study. In the Fig. 7, the high amplitude regions marked with dotted red lines are forced vibrations, which are experienced due to intermittent cutting and occur at regular frequency intervals. The response is recorded in the X and Y direction. Eliminating the forced vibration, we can observe that the chatter vibration of high amplitude at other frequencies are noticed in the side cut at 0.35 mm, 0.45mm and the bottom cut experiences the chatter only at 0.6mm axial depth of cut.

Conclusion

The experiment confirms the analytical results predicted, thereby confirming the proposed study. The direction of cutting has a significant effect on the stability and reducing the mode-coupling chatter. The asymmetric nature of the machine contributes to this effect. The results shown are for the given machine where greater stability is observed in the bottom cut. However, the effective direction of cutting varies based on the machine. Achieving more symmetricity in the machine would minimize this difference and provide a direction independent stability. However, due to technical constraints, the machines may not be designed to full symmetricity. The machining process can consider machining in the effective side at a faster material removal rate for more productivity. since only the transfer function matrix changes in our analytical model. The direction of cutting also carries an effect on regenerative chatter, but it is not considered in this paper.

References

[1] E. Budak, "An analytical design method for milling cutters with non-constant pitch to increase stability," 2003.

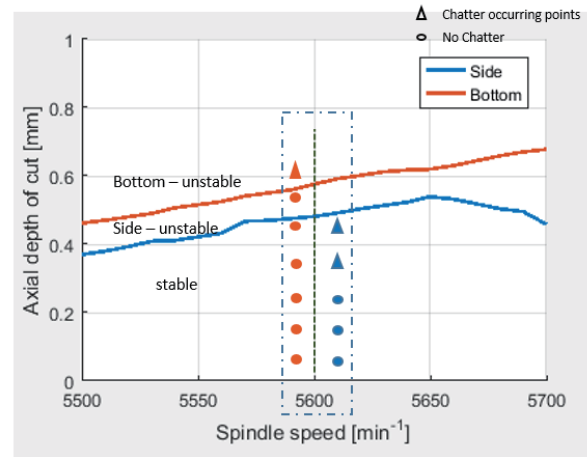


Fig. 8 Stability Graph with experimental points plotted

- [2] E. Shamoto, K. Kageyama and M. K, "Suppression of regenerative chatter vibration with irregular pitch end mill - construction of analytical mode and optimization of pitch angle," *Proceedings of JSME Kansai Branch Annual Meeting*, 2000.
- [3] E. Shamoto, T. Mori, B. Sencer, N. Suzuki and R. Hino, "Suppression of regenerative chatter vibration in multiple milling utilizing speed difference method - analysis of double side milling and its generalization to multiple milling operations," 2013.
- [4] S. Eiji and A. Saito, "A novel deep groove machining method utilizing variable-pitch end mill with feed-directional thin support," 2015.
- [5] Y. Altintas, *Manufacturing Automation*, Cambridge University Press, 2000.
- [6] Y. Altintas and E. Budak, "Analytical prediction of stability lobes in milling," *CIRP Annals*, 1995.
- [7] Y. Altintas, S. Engin and E. Budak, "Analytical Stability Prediction and Design of Variable Pitch Cutters," *Journal of Manufacturing Science and Engineering*, vol. 121, 1999.

EXPERIMENTAL AND COMPUTATIONAL ANALYSES FOR THE MOLTEN BOROSILICATE GLASS WITH/WITHOUT CRYSTALLINE MATERIALS

Xiaojin Shen

Department of Nuclear Engineering and Radiological Science, Graduate School of University of Michigan
xjserena@umich.edu

Supervisors: Prof. Y. Enokida, Prof. T. Sugiyama

(Affiliation) Graduate School of Engineering, Nagoya University
yenokida@nagoya-u.jp/t-sugiyama@nucl.nagoya-u.ac.jp

ABSTRACT

Vitrification is a widely used technology and has been applied for nuclear waste reprocessing for more than 40 years including high level nuclear waste (HLW) immobilisation. The vitrification process for the HLW with borosilicate glass-forming additives as the waste-glass frit will make the hazardous waste constituents be immobilised into the glass matrix. However, during vitrification the phase segregated ruthenium dioxide (RuO_2) and other metal element like platinum and tellurium alloy (Pd-Te) can largely effect on the viscosity of molten glass. This paper aims to study the physical phenomenon influenced by those segregated phases by the comparison between the experimental measurements of the viscosity of the molten glasses with and without those phases for actual simulating glass and the computational simulation by ANSYS/Fluent 16.2, expanding upon on the previous work at Nuclear Chemical lab of Nagoya University, which focused attention on the RuO_2 effect on the viscosity of molten borosilicate glass only.

1. INTRODUCTION AND BACKGROUND

In the previous work [1], it has been proved that the white beads, which is a raw material to form borosilicate glass, possess the property as Newtonian-fluid. After adding the spherical ruthenium dioxide into the glass matrix, the viscosity increased has been shown from the experimental measurement. In this paper, we focus our attention on the actual simulating glass prepared by CREIPI (Central Research Institute of Electric Power Industry) contained with needle-shaped ruthenium dioxide and other metals as Pd and Te. The two primary goals of my project are (1) to conduct the viscosity measurement of the molten glass for the actual simulating glass from CREIPI (2) to simulate the rheological phenomena for the molten glass with/without segregated phase by ANSYS/Fluent 16.2.

2. EXPERIMENTAL MEASUREMENT OF VISCOSITY OF MOLTEN GLASSES

2.1 EXPERIMENTAL SETTING

The viscosity calibration measurement was performed by Brookfield viscometer standard fluid-5000 to be performed before each measurement of a specified glass sample in our study to ensure accuracy. The accuracy of individual measurements was +/- 5% for $\log(\text{viscosity})$. We started to measure the viscosity for 200 g batches of white beads free of solid particles or crystalline materials in order to verify the measurement in the previous work [1]. A Pt-Rd spindle suspended from a Brookfield viscometer was immersed in the center of the melt in the electric furnace (Fig.1). Rate of shear for the measurement could be varied from 0.01 – 200 rpm, and temperatures ranged from 900 – 1200 °C.



Fig.1 The apparatus for viscosity measurement

The measurement of white beads was conducted under the temperature of 900, 1000, 1100 °C. Besides of white beads, there are other three specified glasses in our project; enriched bottom, purified top and mother glass of the simulated borosilicate glasses. Compositions for the white beads and the original simulated borosilicate glass from CREIPI are listed in Table 1 and Table 2.

The modified glass was obtained by thermal treatment to an original simulated borosilicate glass of 900g for 100 hours under the temperature of 1100 °C, over the continued heating time that all RuO₂ particles located initial randomly in the glass have fallen to the bottom, where it was called *enriched* glass, while the top part of the glass was called *purified* glass. Bottom and top parts of the thermally treated glass to segregate separating phases. Sedimentation behavior in the creeping flow of the glassy melt can be expressed by the Einstein Relation – Stoke’s law. For a spherical particle diffusing through a liquid with low Re, there are three main forces acting on it; drag force, buoyancy and the gravity. We assume that all solid particles have shared a spherical shape and they fall down to the bottom layer with the terminal velocity. This settling velocity is another assumption for our calculation, which means when the drag force and the buoyancy are identical with the gravity.

The drag force and the buoyancy are given by

$$F_{db} = 3\pi\mu rV + \frac{\pi}{6}r^3\rho_f g \quad (1)$$

The gravity is given by

$$F_g = \frac{\pi}{6}r^3\rho_s g \quad (2)$$

r is the radius of the spherical particle, ρ_f is the density of the fluid and ρ_s is the density of the solid particle. Therefore, the terminal velocity we used is given by,

$$3\pi\mu rV_t + \frac{\pi}{6}r^3\rho_f g = \frac{\pi}{6}r^3\rho_s g \quad (3)$$

The ratio between the density of glassy melt and the solid particle was assumed 0.35 and the diameter of the solid particle, 10µm. After computed the terminal velocity, we computed the falling time for the crucible height of 100 cm in our case. We consider that the maximum falling time is for the solid particles located at the top edge of the glassy melt with the constant velocity as the terminal velocity, which equals to 4 days. Hence we performed 100 hours heating treatment to set all solid particles, especially the ruthenium dioxide, down to the bottom layers of the modified glass.

The X-ray diffraction and the composition analyses for bottom and top portions of the modified glass are shown in the result section. Both of the enriched glass and the purified glass were conducted by x-ray diffraction method to determine the crystalline content of composition RuO₂ and the platinum element as the Pd-Te alloy. Since before the original simulated glass being modified it contained with 40.1 wt% of SiO₂, 12.9 wt% of Na₂O and 12.1 wt% of B₂O₃ (Table 2), so that we constructed a *mother glass* (Table 3) free of crystalline materials and solid particles with the same ratio of those three main components as a role of a comparison study. The composition of the mother glass is shown in Table 2. The objective for the measurement of viscosity of the specified glasses in our study is to compare the viscosity of the enriched and purified glasses and also to compare both the viscosity with the mother glass.

Table 1 - The compositions of white beads, 200g

Components	Fraction, wt %
SiO ₂	60
Na ₂ O	4
B ₂ O ₃	18.2
Al ₂ O ₃	6.4
ZnO	3.8
CaO	3.8
Li ₂ O	3.8
Total	100

Table 2 - The compositions of the original simulated borosilicate glass from CREIPI, 900g

Components	Fraction, wt %
SiO ₂	40.1
Na ₂ O	12.9
B ₂ O ₃	12.1
Al ₂ O ₃	4.65
Nd ₂ O ₃	2.95
CaO	2.92
Li ₂ O	2.56
ZnO	2.51
MoO3	2.39
Ce2O3	2.12
ZrO2	2.06
La2O3	1.58
Gd2O3	1.27
Fe2O3	1.18
Cr2O	1.12
Pr2O3	0.84
BaO	0.63
NiO	0.56
RuO2	0.53
Sm2O3	0.35
MnO2	0.34
PdO	0.32
Cr2O3	0.31
SrO	0.23
Y2O3	0.17
Rh2O3	0.13
TeO2	0.06
Total	96.9

Table 3 - The compositions of constructed mother glass, 120g

Components	Fraction, wt %
SiO ₂	40.1
Na ₂ O	12.9
B ₂ O ₃	12.1
Al ₂ O ₃	13.94
ZnO	6.97
CaO	10.45
Li ₂ O	3.53
Total	100

2.2 EXPERIMENTAL RESULTS AND DISCUSSION

The viscosity measurement for the white beads (Fig.2) was verified, by comparison with the experimental data in previous work [1].



Fig.2 The borosilicate glass formed by white beads

The viscosity measurement for the glassy melt of white beads has indicated the Newtonian fluid property; the viscosity is the only function of the heating temperature (Fig.3).

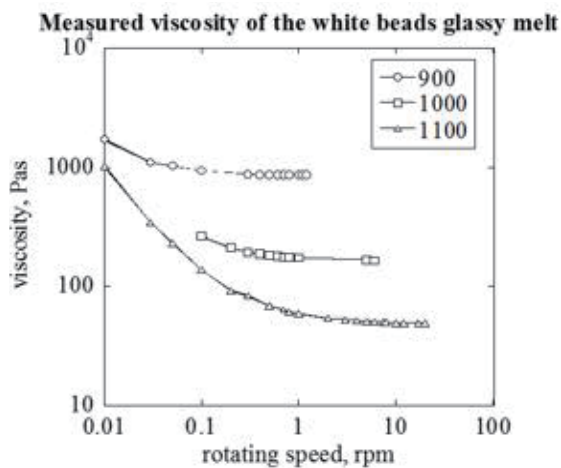


Fig.3 The viscosity measurement of the white beads under the temperature of 900, 1000, 1100°C

The viscosity measurement of the enriched bottom glass sample in 900, 950, 1000, 1100, 1200°C was shown in Fig.4.

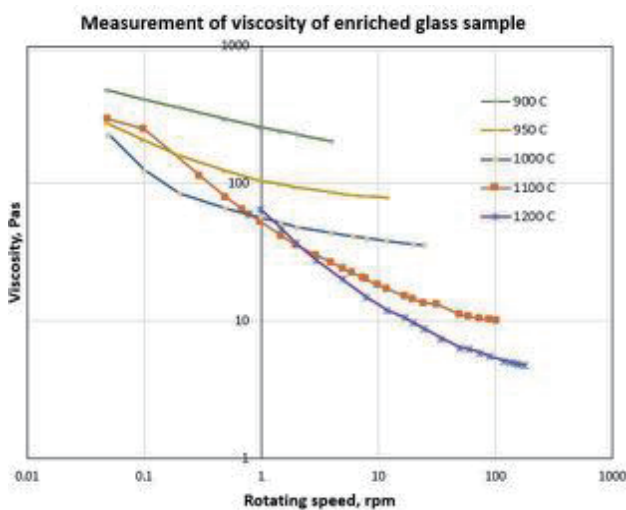


Fig.4 The viscosity measurement of the bottom glass

The viscosity in the enriched glass is a function of both temperature and the rate of shear which indicated that these melts were non-Newtonian; the rheological behavior was influenced by the wt% of crystalline content in the glassy melt. We can see there is an apparent viscosity decreased as the rate of shear increased for each operational temperature; the shear-thinning behavior was presented in the bottom glassy melt. For the non-Newtonian flow with different wt% crystalline content, it was estimated as the physical behavior of suspensions or as the pseudoplastic flow [2], distinct with the Newtonian fluid.

Similarly, the viscosity measurement for the purified top glass sample was shown in Fig.5.

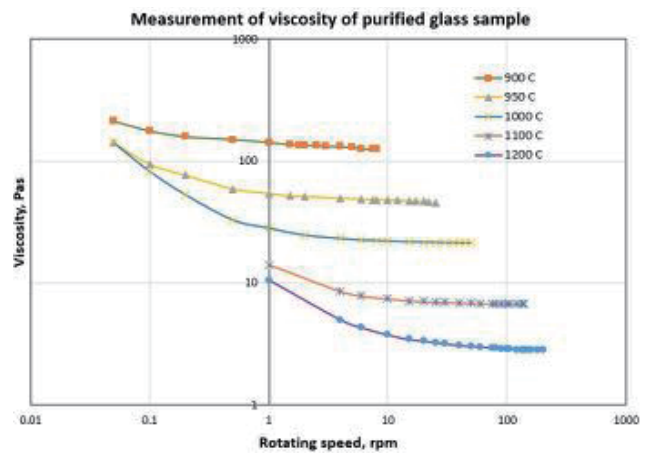


Fig.5 The viscosity measurement of the top glass

In order to prove our assumption that the top of the modified glass has been purified, we used the mother glass to compare with the measurement of viscosity. The measurement of viscosity for the mother glass was shown in Fig.6.

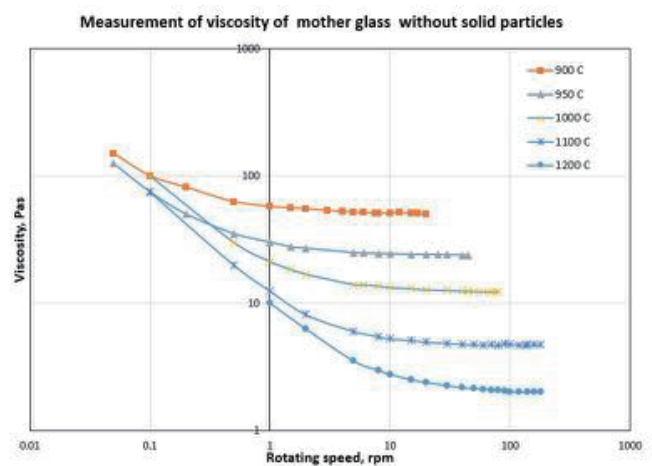


Fig.6 The viscosity measurement of the mother glass

The mother glass has shown as the Newtonian fluid in our study and the measured viscosity in each operational temperature is lower than the top glass, which indicates that even though the top glass has been purified by the thermal treatment it still remains low concentration of crystalline

materials, in which percentage the glassy melt property was protected as Newtonian fluid, to make the fluid more viscous than the mother glass.

The existence of the crystalline materials of ruthenium dioxide, Pd-Te (Fig.7) has been shown by X-ray diffraction (XRD) method for the enriched bottom portion glass compared with the original simulated borosilicate glass from CREIPI and purified top portion glass after the thermal treatment.

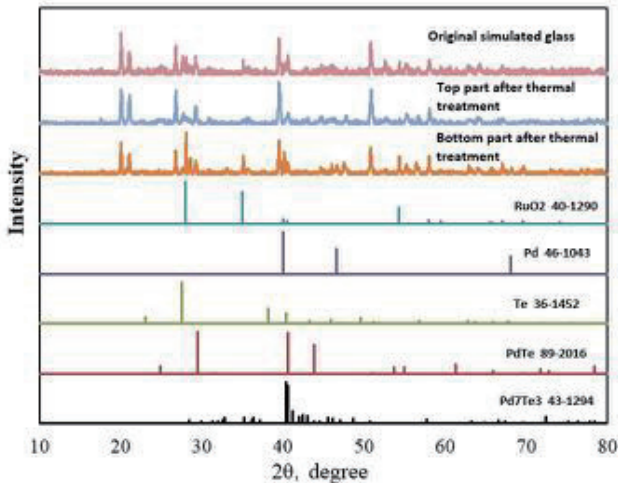


Fig.7 XRD data for the glass samples from original simulated glass, purified top glass and enriched bottom glass

The XRD data indicates that the concentration of RuO₂ in the bottom part is higher than the top part as there are three high peaks from ICDD matched with the curve from bottom glass rather than top portion. The Pd-Te alloy is also more enriched in the bottom portion.

The composition measurement has been conducted by the alkaline fusion (Table 4). We use the glass powder samples from those three specified glasses to conduct the measurement. The powder specimen of enriched bottom glass and purified top glass (Fig.8) were used as 0.05g be dissolved by the Na₂O₂ of 0.5g, later we diluted the glass powder by using 5.0% HCL solution.

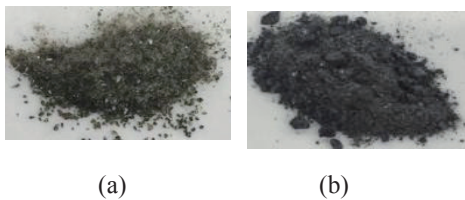


Fig.8 The glass powder specimen of the (a) top portion and (b) bottom portion

Table 4 -The concentration of RuO₂, Pd and Te in the specified glasses in wt%

Components	Original	Bottom	Top
RuO ₂	0.1800	1.1825	0.024
Pd	0.1821	0.7013	0.0153
Te	0.0387	0.0210	0.0245

After the thermal treatment, the sedimentation of RuO₂ was performed, as well as Pd. Te is almost in same concentration level between bottom and top portions, which indicates a possible reason for the viscosity measurement of top glass higher than the mother glass.

In this section, we proved that higher concentration of crystalline materials in the glassy melt would make the fluid more viscous and its fluid property may change to be non-Newtonian fluid.

3. NUMERICAL SIMULATION

3.1 NATURAL CONVECTION STUDY

In this section, we focus our attention on the natural convection of the molten glass with/without solid particles as the ruthenium dioxide in a 2D 1×1 m square domain with 100×100 of mesh size which is fine enough to get a mesh converged result (Fig.9).

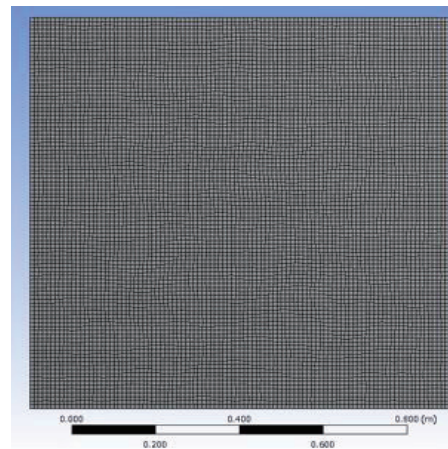


Fig.9 The enclosure geometry for the simulation of the natural convection for the glassy melt

The temperature for the top and bottom boundary are 900°C and 1200°C, and other boundaries set to no-slip. The glassy melt as the liquid phase is assumed as Newtonian fluid in this domain of interest. The rheological phenomenon of the natural convection of this laminar flow is driven by the temperature difference and the gravity. The Boussinesq model is used to restrain the density function of the flow. The viscosity of the glassy melt is imported from the experimental data of the viscosity measurement of white beads without/with 5.0 wt% RuO₂ [1] (Table 5). The relation between the viscosity and the temperature for the glassy melt as the Newtonian fluid can be expressed by the Vogel Fulcher Tammann law (VFT) theoretically.

VFT law is used mainly for glass. The equation is expressed as the following,

$$H(T) = 10^{-A + \frac{B}{T-C}} \quad (4)$$

Hence, the viscosity as the function of temperature is given by,

$$\log_{10} \eta = A + \frac{B}{T - T_0} \quad (5)$$

A, B and T_0 are three constants independent on temperature. From the viscosity measurement we can compute those three constants by three viscosity value in 900, 1000, 1100°C. In our simulation, the piecewise-linear model is applied to estimate the viscosity as the only function of temperature (Fig.10).

Table 5 - Viscosity data for the natural convection study

Temperature, K \ Viscosity, Pas	Without RuO ₂	With 5.0 wt% RuO ₂
1173	856.34	888.7
1273	173.69	179.27
1373	49.73	53.98
1473	19.3	21.5

The viscosity for each temperature is obtained by the simple average of the measured viscosity over the rotating speed range in which the viscosity varying by the shear stress can be considered to be steady.

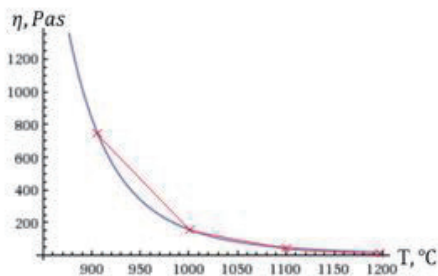


Fig.10 The viscosity estimation of the numerical simulation

In order to ensure the accuracy, it will need more measured viscosity data to import the simulation. In our study we imported only four points of the measured viscosity. A series of velocity fields for the glassy melt without/with RuO₂ in 20, 30, 50, 80 min has been shown in Fig.11.

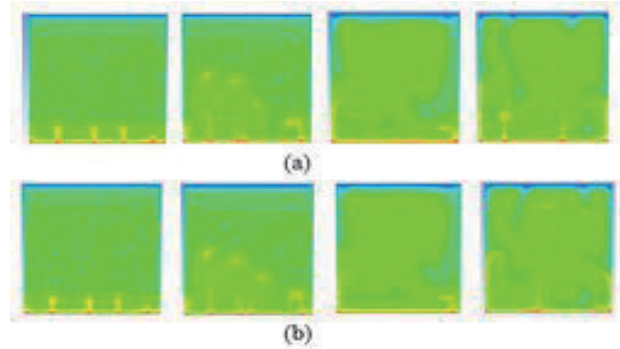


Fig.11 Velocity distribution for the glassy melt (a) without RuO₂ (b) with RuO₂

The natural convection in our case starts from 20 min, and over the time up to 100 min. The velocity magnitude of the domain shows that due to the viscosity increased of the glassy melt the velocity magnitude of the domain gets smaller than the glassy melt without RuO₂ and also the natural convection was more retarded (Fig.12).

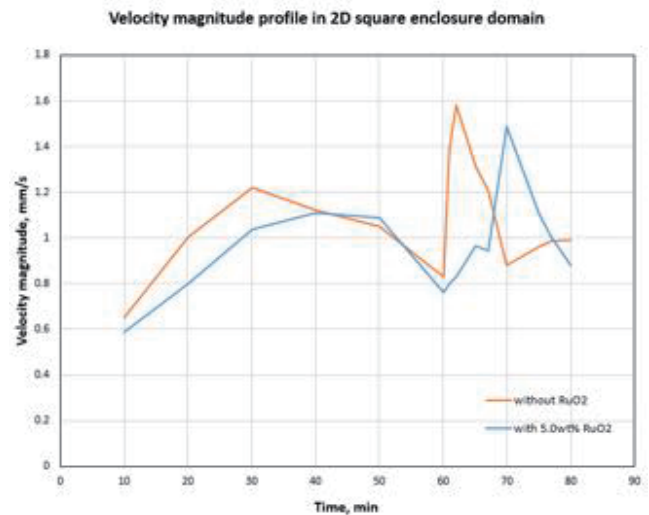


Fig.12 Velocity magnitude for the glassy melt (a) without RuO₂ (b) with 5.0 wt% RuO₂ in domain of square enclosure

In this simple case of study, we observed the natural convection phenomenon in the domain of interest and compared the velocity magnitude between the glassy melt with/without RuO₂.

3.2 THE SENSITIVITY STUDY FOR AN 2D INCLINED PLANE

We then try to bring to light on how the glassy melt flowing down along the plane. The glassy melt is flowing down with/without solid particles in a 2D inclined plane. The domain of interest with the boundary conditions of velocity inlet, pressure outlet, the free surface of the ambient top wall and the no-slip of the bottom wall. There are two types of laminar flow in our study, the single phase of glassy melt without solid particles (RuO₂) and the other is two-phase flow of the glassy melts with and without the solid particles. In the latter type, we apply the volume of fluid (VOF) model to

simulate for this multiphase flow on an inclined plane. Since in the VOF model we cannot track particles in the glassy melt, we have to assume the flow as an imaginary single-phase flow even though it contains solid particles and there is no interpenetration with another phase of flow without solid particles. The sensitivity study for those two types of flow is followed by changing the operational temperature to 1000, 1100 and 1200°C, we employ the viscosity data (Table.5) of the glassy melt as a constant fluid property respectively. The velocity distribution and the vector plot for the glassy melt without solid particles and the two-phase flow is shown in Fig. 13 and Fig.14 under the temperature of 1000°C.

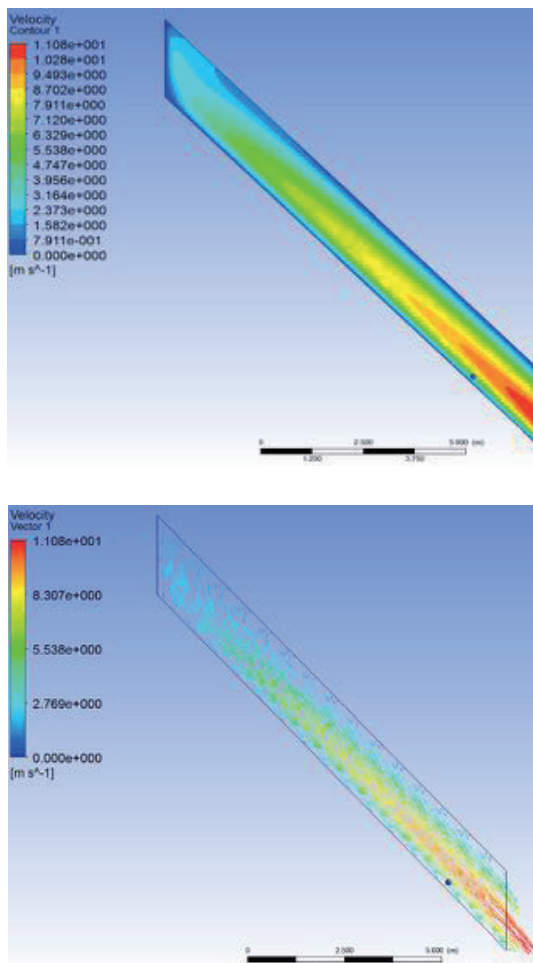


Fig.13 Velocity magnitude distribution and the vector plot for the glassy melt without solid particles

In the domain of interest, we create a derived point near the outlet above the bottom wall in order to monitor its velocity magnitude in the transient study.

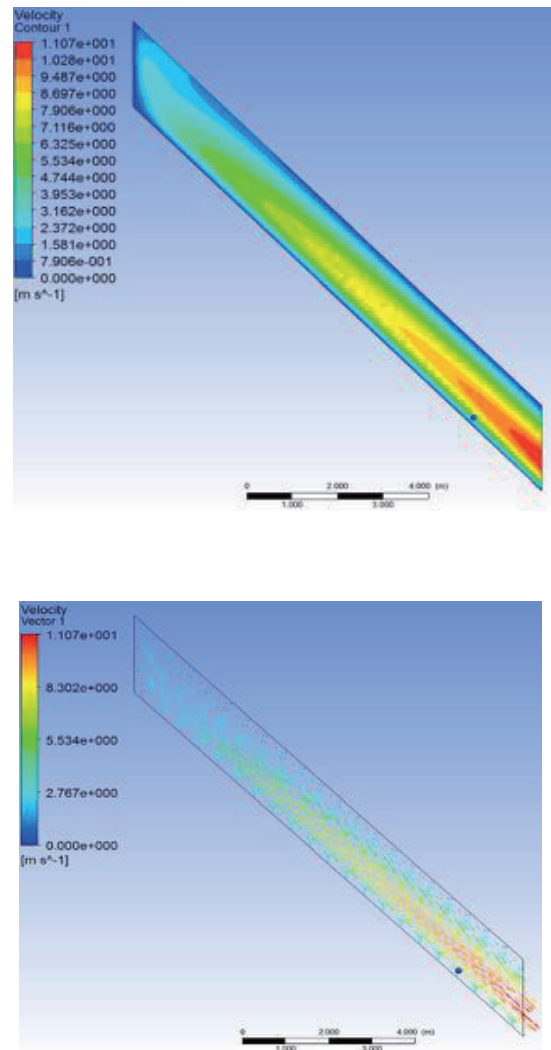


Fig.14 Velocity magnitude distribution and the vector plot for the glassy melt with solid particles

We manipulate the temperature to 1100°C and 1200°C to collect the monitored velocity magnitude of the derived point in those two types of flow. As we want to observe the varying of velocity magnitude of this point over the time, we enlarge the time step from 0.01 to 0.1 seconds to run the simulation and after the time up to 10 seconds, we can see that the result gets converged (Fig.15). To increase the temperature, it will greatly improve the fluidity of the glassy melt. From the monitored data, we can see that in the operational temperature of 1200°C, the converged velocity variance for the derived point in the melt without solid particles and in the two-phase melt is one order of magnitude smaller than in the temperature of 1000°C. (Table.6)

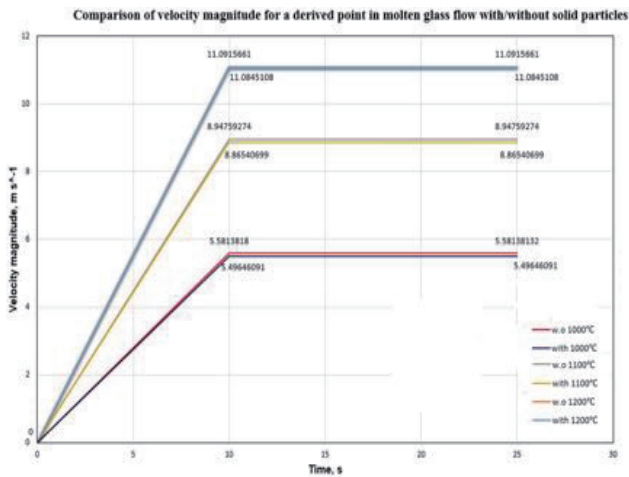


Fig.15 Velocity magnitude monitor of the derived point in different operational temperature in the glassy melt

Table 6 - The velocity differences for the two types of glassy flow in 1000, 1100, 1200°C

Temperature, °C	V _{single-phase} , m/s	V _{two-phase} , m/s	Δv, m/s
1000	5.582	5.496	0.086
1100	8.948	8.865	0.083
1200	11.092	11.085	0.007

3.3 RHEOLOGICAL BEHAVIOUR FOR THE MOLTEN GLASS IN THE MELTER

In the realistic geometry, the joule-heated glass melter feeds the resultant slurry combined with the liquid waste and glass ingredients (Fig. 16).

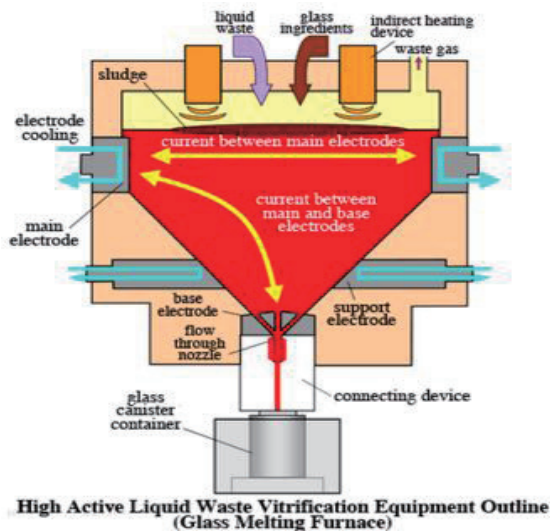


Fig.16 The glassy melter for the HLW vitrification

In order to immobilize nuclear waste in a durable glass, the glass composition we use must be a good solvent for important radioactive waste constituents. The error in feed preparation will mainly cause the formation of crystalline material in the glassy melt. We simplified the study that we

assumed Newtonian fluid property to simulate the glassy melt flow in the melter to observe the natural convection and the velocity distribution in the domain of interest. The viscosity data is imported from Table.7.

Table 7 - Viscosity data for the simulated scaling melter

Temperature, K \ Viscosity, Pas	Without solid particles	With solid particles
1173	856.34	1100
1273	173.69	198
1373	49.73	60
1473	19.3	24.8

The domain of interest for our study is scaled into a 2D melter form with the top and bottom thermal boundary condition of 1200°C and 1182°C and no-slip on the wall edges and a pressure outlet (Fig.17)

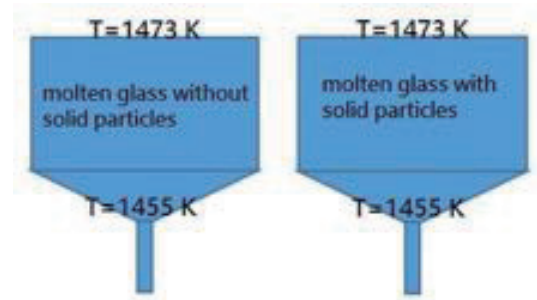


Fig.17 The simulation scaling melter

The natural convection of the glassy melt is driven by a small temperature difference on the boundaries in a transient study. We use the Boussinesq model to estimate the density of the flow and the y- direction of gravity to create the buoyancy.

There are two glassy flow in our study; single-phase flow of the glassy melt without solid particles and the imaginable single-phase flow with the viscosity contained solid particles. The simulation of those two types of flow run from 0 to 500 s with the time step of 0.05s. In the velocity magnitude distribution and the vector scheme, we can see the vortex direction in the melter and the temperature distribution stays homogeneous. The viscosity for the flow of imaginable single-phase glassy melt with the solid particles gets enlarged compared with the data in Table. 5, in this case we can predict how the viscosity enlarged can interfere the velocity magnitude of the domain, to note that the sedimentation or accumulation of those crystalline materials will be likely to occur in the local domain where has a lower velocity

magnitude. The velocity magnitude and the its vector scheme for those two types of flow are shown in Fig.18 and Fig.19.

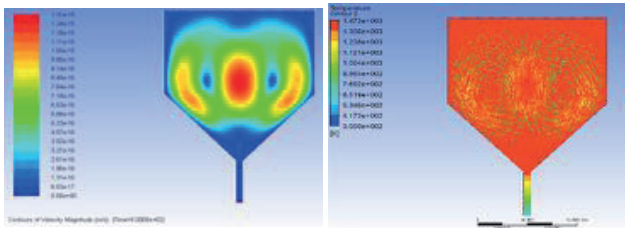


Fig.18 Velocity magnitude and temperature distributions for the single phase glassy melt without solid particles

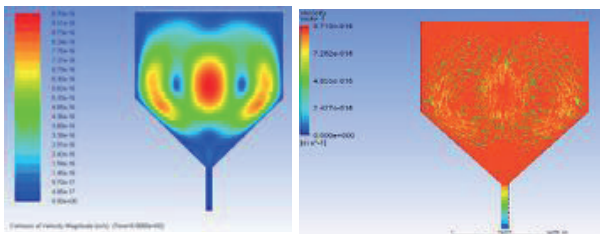


Fig.19 Velocity magnitude and temperature distributions for the imaginable single phase glassy melt with solid particles

4. CONCLUSIONS

In our study, we proved that the glassy melt of white beads has the rheological property as Newtonian fluid. We studied that by a high concentration of crystalline material, the fluid property would change as non-Newtonian fluid. Under the thermal treatment for actual simulated glass, the enriched bottom glass has more viscous fluid property than the purified top glass which causes by the high concentration of RuO₂ and Pd-Te alloy. In the numerical simulation, we simulated the case for the glassy melt flowing along the inclined plane, by the sensitivity study in different operational temperature, increasing the temperature will greatly improve the fluidity of the glassy melt. For the two-phase glassy melt we used the viscosity data by averaging all the rotating speed, these crystal-containing melts also become more fluid as the amount of shear they experience increases. Thus, mechanical agitation could mitigate the problem caused from crystalline materials. We simulated the natural convection phenomenon of the single-phase glassy melt without solid particles and imaginable single-phase glassy melt with solid particles, which predicts the natural convection vortex of the domain in the scaled melter, in realistic the glassy melt cannot be assumed as Newtonian fluid instead of non-Newtonian fluid to simulate the actual glass melter. The numerical simulation

in our study was validated by a Bingham fluid between two parallel plates against the analytical solution.

ACKNOWLEDGEMENTS

I have taken efforts in this project. However, it would not have been possible without the kind support and help of my supervisors and my teaching assistant and the study resources and hardware provided at Nagoya University and the JUACEP program. I would like to extend my sincere thanks to all of them. I am highly indebted to Professor Y.Enokida and Professor T.Sugiyama for their guidance and constant supervision as well as for providing necessary information regarding the project and also for their support in completing the project. I would like to express my special gratitude and thanks to my teaching assistant S.Uchimura for his patience and carefulness and the keen on the experimental measurements to contribute himself into the teamwork for this project.

REFERENCES

- [1] Yoshida, Master's thesis, (2015).
- [2] M. John Plodinec, IHEOLOGY OF GLASSES CONTAINING CRYSTALLINE MATERIAL, (1986).
- [3] NETL's non-Newtonian Multiphase Slurry Workshop Report, (2013).
- [4] Rokkasho Reprocessing Plant: Vitrification Problems Continue, CNIC.
- [5] Vinay Ramohalli Gopalaa, Jan-Aiso Lycklama à Nijeholta, Paul Bakkerb, Benno Haverkatea, Development and validation of a CFD model predicting the backfill process of a nuclear waste gallery, (2011).
- [6] Sandia National Laboratories, Multiscale Models of Nuclear Waste Reprocessing: From the Mesoscale to the Plant-Scale, (2012).
- [7] Y.Enokida, Kayo Sawada, Takahiro Shimada, and Daisuke Hirabayashi, Formation Mechanisms of the Needle-shaped Crystals of Ruthenium Dioxide during Vitrification of Nitric Acid Solution Containing Nitrosyl Ruthenium Nitrate, (2011).
- [8] Vinit Khandelwal, Amit Dhiman, Laszlo Baranyi, Laminar flow of non-Newtonian shear-thinning fluids in a T-channel, (2014).

TEMPERATURE DEPENDENT THERMAL-ELECTRICAL-STRUCTURAL FINITE ELEMENT ANALYSIS AROUND CRACK TIP UNDER HIGH CURRENT DENSITY ELECTROPULSING

Carlos Gámez

Mechanical and Aerospace Engineering, University of California Los Angeles
carlosgamez@ucla.edu

Supervisor: Prof. Yasuyuki Morita

Department of Mechanical Science and Engineering, Nagoya University
morita@mech.nagoya-u.ac.jp

ABSTRACT

Material fracture due to crack propagation is a common means in which a material will irreversibly fail. Electropulsing treatment is a practical method to stop crack propagation. In this paper an Al 6061-T6 with a single edge crack is modeled in Abaqus using temperature-dependent material properties. An initiation damage analysis was also developed to predict possible failures due to the electropulsing treatment. Samples were subjected to a current density of $3.2 \times 10^9 \text{ A/m}^2$ to measure the temperature and stress field around the crack tip. The experimental results show the melted region at the tip of the crack, the same area that is predicted with the Abaqus model. A Vickers hardness test was used to validate the temperature field obtained with the simulation.

1. INTRODUCTION

The aluminium alloy 6061-T6 is a precipitation hardened alloy with high content of magnesium and silicon that is extremely popular due to its toughness and workability. The mechanical properties that Al 6061-T6 has makes it one of the most common alloys used in a wide range of applications, including but not limited to: aircraft fittings, hydraulic pistons, appliance fittings, valve parts, and camera lens mounts [1]. Despite having excellent mechanical properties, this alloy may still fail under certain circumstances. Fatigue cracking is one of the failure modes that is frequently present in this alloy, therefore, various techniques have been developed to arrest the crack propagation or heal the crack [2].

Crack healing is recommended for practical applications [3] (particularly important in the aircraft industry) where a crack failure must be avoided. It has been proven that one method to arrest crack propagation is the use of thermal stresses [4]. However, this is just one of many methods, cold expansion [3, 4], laser welding [5, 6], artificial wedge infiltration [7, 8] and electropulsing treatment [9] have also been used to arrest cracks. Considering efficiency, the electropulsing treatment is one of the best methods, the

damage and deformation that it causes is almost negligible compared to the other methods [1].

Electropulsing treatment uses a high Electric Current Density (ECD) in a short period of time (around 1.5 ms) to create a desired thermal and mechanical response on a sample. For this reason, it is important to know the thermal and mechanical response of a crack tip under high ECD to understand how the treatment helps to arrest the crack. It is known that the alloy melts instantly forming a circular or elliptical hole at the crack tip. As well, the ejection of the melted metal is driven by an electromagnetic force and an inflation pressure [10]. In addition to this, due to the thermal compressive stress and the elimination of the stress concentration at the crack tip, the crack growth can be stopped [1].

To calculate the temperature field several thermal-electric numerical models have been developed, but they neglect the mechanical response (no stress field). Furthermore, the material properties used in previous numerical models are not dependent upon temperature. To fill the gap, in this study a Temperature Dependent Thermal-Electrical-Structural (TES) numeral solution was developed in Abaqus to obtain a more predictive temperature and pressure distribution around the track tip.

2. EXPERIMENTAL PROCEDURE

The Al 6061-T6 sample is 0.5mm thick with a cross-sectional area of $2.5 \times 10^{-6} \text{ m}^2$ in the middle of the sample. A single-edge crack of 0.140mm wide and 1mm long was cut by a wire cutter. Fig. 1 shows the dimensions of the sample.

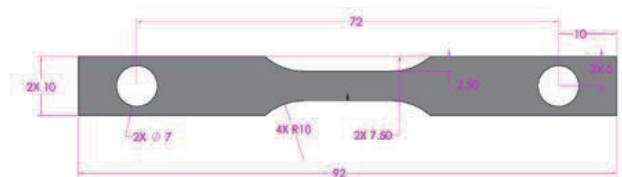


Fig. 1 Sample design. All the dimensions are in millimetres.

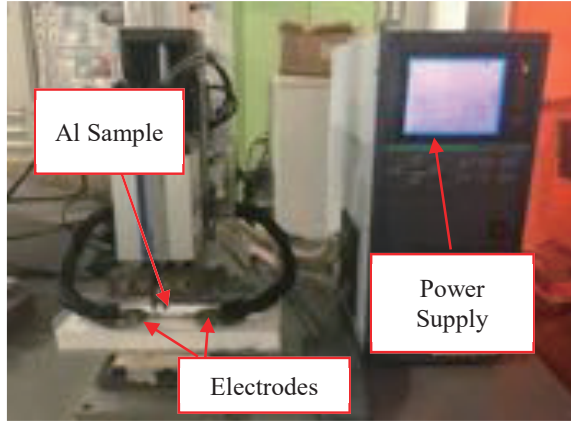


Fig. 2 Experimental Setup.

The electropulsing treatment experiment was performed under ambient conditions using a high-pulsed current discharge device. Fig. 2 provides the experimental setup.

The current delivered by the power supply is provided on the screen in the form of a graph and it is capable of reaching a maximum electrical current of 8kA in 1.5ms. The maximum ECD achieved with this setup is $3.2 \times 10^9 \text{ A/m}^2$.

2. NUMERICAL SOLUTION IN ABAQUS

Abaqus/Standard are modelling software that offer a fully coupled thermal-electric-structural analysis. The numerical simulation must solve for the displacement, temperature, and electrical potential simultaneously to obtain an accurate result [11]. The model consists a static step of a representative 3D part that depicts the Al 6061-T6 sample. The static step is 1.6 ms long with a 1.6×10^{-6} time step.

2.1 Governing Equations

To understand the response of the sample during the experiment it is necessary to identify the equations that are being solved by Abaqus. When an electrical current passes through a conductor, the conductor produces heat. This is known as Joule Heating and it can be represented by the following equation [12]

$$P = I^2 R \quad (1)$$

where P is the Joule heating power, I is the electric current and R is the resistance. The power is converted into heat and this heat is conducted through the sample.

The heat flow with a moving heat source in an elementary volume can be expressed as:

$$\rho C_p \dot{T} - \nabla \cdot (k \nabla T) = \dot{Q} \quad (2)$$

where $\rho = \rho(T)$ is density and $C_p = C_p(T)$ is the specific heat, $k = k(T)$ is thermal conductivity and \dot{Q} is the heat generation.

Thermal stress and strain are the result of an uneven temperature field and displacement constraints. The thermal stress can be expressed as

$$\sigma = E \alpha \Delta T \quad (3)$$

where σ is stress, $E = E(T)$ is the Young's modulus, α is the thermal expansion coefficient, and ΔT is the change in temperature. One last equation that must be satisfy is the equilibrium equations.

All the equations are coupled and nearly all of the variables depend on temperature, making a numerical solution with temperature dependent variables a more reliable numerical solution.

2.2 Material Properties

The material properties used in the Abaqus model are listed in Table 1 [13,14].

Table 1. Material properties of aluminum alloy 6061-T6.

Material	T(°C)	k (W·m ⁻¹ ·K ⁻¹)	C _p (J·kg ⁻¹ ·K ⁻¹)	ρ (kg·m ⁻³)	E (GPa)	α (×10 ⁻⁶ ·K ⁻¹)
Al Alloy 6061-T6	0	161	917	2703	69.7	22.4
	98	177	978	2685	66.2	24.61
	201	192	1028	2657	59.2	26.6
	316	207	1078	2630	47.78	27.6
	428	223	1133	2602	31.72	29.6
	571	253	1230	2574	0	34.2

The amount of data points is limited so in order to get a more accurate approximation of the values necessary for the simulations, a curve fitting analysis was done in Matlab. Figs. 3-6 show the curve fitting with its respective equation and

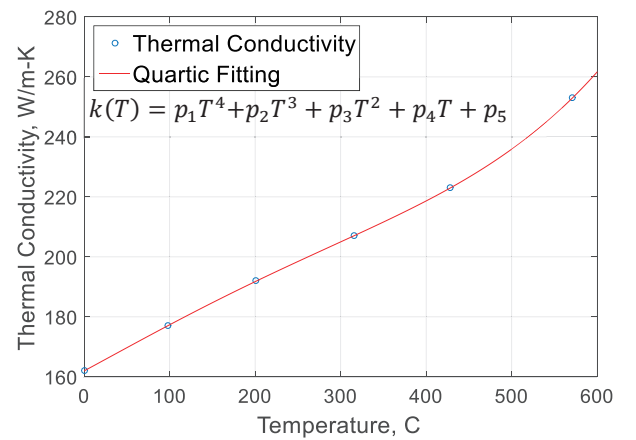


Fig. 3 Thermal conductivity polynomial curve fitting, where $p_1 = 6.9e^{-10}$, $p_2 = -4.4e^{-07}$, $p_3 = 3.35e^{-05}$, $p_4 = 0.154$, $p_5 = 162$.

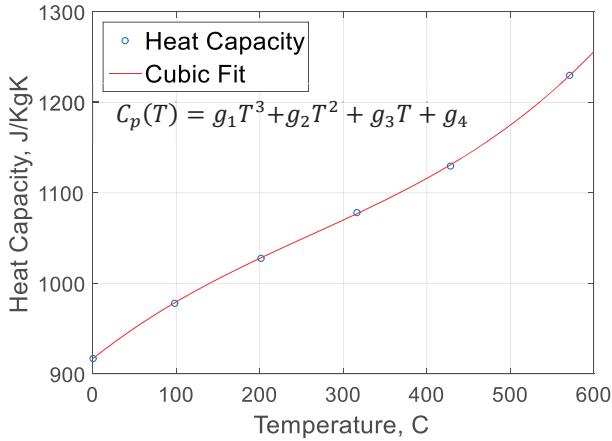


Fig. 4 Heat Capacity polynomial curve fitting, where $g_1=1.5e^{-6}$, $g_2=-0.001206$, $g_3=0.7339$, $g_4=916.7$.

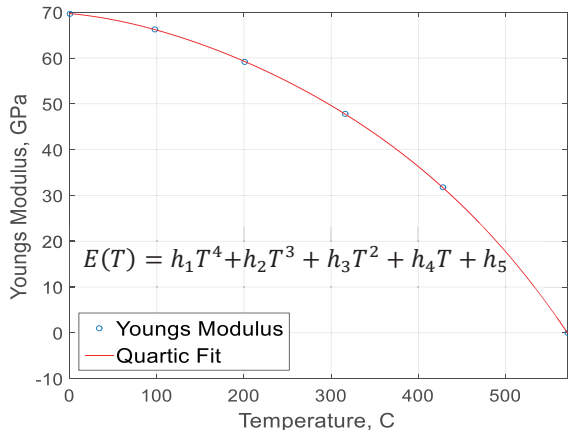


Fig. 5 Young's Modulus polynomial curve fitting, where $h_1=-3.9e^{-10}$, $h_2=2.73e^{-7}$, $h_3=-0.00021$, $h_4=-0.017$, $h_5=69.7$.

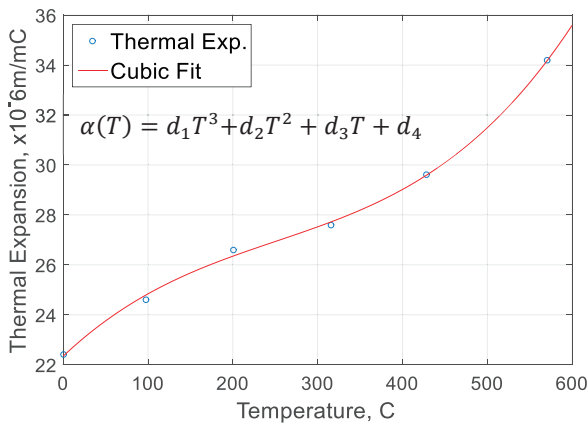


Fig. 6 Thermal Expansion coefficient polynomial curve fitting, where $d_1=1.1e^{-07}$, $d_2=-8.2e^{-05}$, $d_3=0.03206$, $d_4=22.35$.

coefficient values. It is noteworthy to mention that Abaqus does not update the density value during the analysis, so it was kept to the corresponding room temperature value.

Resistance values for conductors at any temperature other than the standard temperature (usually specified at 20 °C) can be determined through the formula [15]:

$$R(T) = R_{ref}[1 + \beta(T - T_{ref})] \quad (4)$$

where R is the electrical resistance, $R_{ref}=3.99 \times 10^{-8} \Omega$ is the reference electrical resistance, $T_{ref}=20^\circ\text{C}$ is the reference temperature and $\beta=0.004308$ is the temperature coefficient of resistance for the conductor material. The exact value for β was not found for 6061-T6 in literature, however since the majority of the alloy (> 97%) consists of Al, the β for Al was used instead.

The electrical resistivity is not a material property input in Abaqus, instead it has an electrical conductivity, γ , input. γ is the inverse of resistivity and is a function of temperature:

$$\gamma(T) = \frac{1}{R(T)} \quad (5)$$

To address the remaining material properties of Al 6061-T6 for the model, the Joule Heat fraction was set to 1 (all the power is going to be converted to heat), the latent heat was set to 380kJ/Kg, the solidus temperature to 600°C and the liquidus temperature to 642°C [19].

2.3 Interaction

The sample with a given surface area will interact with the air surrounding it. To calculate the heat loss of the system to its surroundings, two interactions were added to the model: convection and radiation.

The convection coefficient, $h_c=10 \text{ W}/(\text{m}^2\text{K})$, for low speed flow of air over a surface was selected to calculate the heat loss [16]. Heat loss due to radiation was expected to be small but it also was included in the model. The emissivity, ϵ , for an unpolished surface Al 6061-T6 is 0.4. The change in emissivity and the convection coefficient with respect to temperature was neglected as their temperature relationship was not found in literature. The absolute zero temperature and the Stefan-Boltzmann constant, σ_{SB} , were utilized in the model where absolute zero was set to -273.13°C and $\sigma_{SB}=5.67 \times 10^{-8} \text{ W}/(\text{m}^2\text{K}^4)$.

2.4 Geometry and Mesh

To avoid a long and heavy computational load on the simulation, a representative section of tested sample was modeled. A section of 10mm x 5mm is enough to get an accurate temperature and stress profile, because the edges are far away from the crack. For the mesh controls, a free tetrahedral was selected to minimize distorted elements without unnecessarily increasing the size of the problem. The overall element size is 0.0002m with a more refine element size in the crack region of $2 \times 10^{-5} \text{ m}$ to get a smooth temperature and stress field around the crack tip. Fig. 7 shows the Tet mesh.

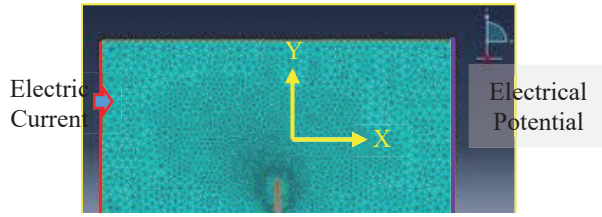


Fig. 7 Tet mesh. Electric current applied on the left hand side and a zero electrical potential on the right side.

2.5 Boundary Conditions and Loading

To replicate the exact conditions of the experiment, a zero stress and a room temperature were set as initial values. An electric current load was applied on the left side of the sample and a zero electrical potential on the right hand side. To avoid the movement of the sample during the simulation four displacement boundary conditions were set, one on each corner. The top left corner was fixed in all directions, the top right is free to move only in the X direction and the bottom corners can move in the XY plane only. Electric current profile was obtained from the screen of the power supply. It had to be approximated since the machine cannot be imported from the machine. Fig. 8 shows Electric current input into the model.

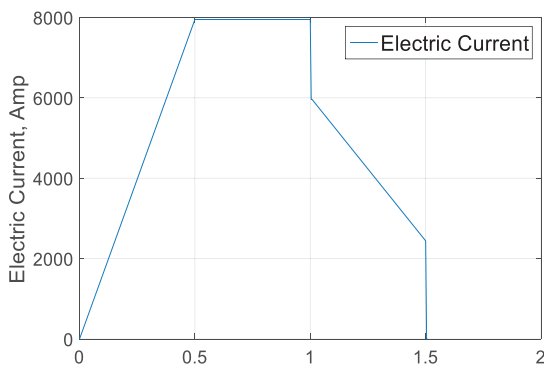


Fig. 8 Electric current profile obtained from the power supplied.

2.6 XFEM analysis

The Extended Finite Element Method (XFEM) capability of Abaqus was used to model any possible damage initiation that might appear as a result of the stress field. The XFEM requires additional enrichment of the material near the crack tip, where the failure is more likely to initiate [11]. The maximum principal stress criteria ('Maxps Damage' in Abaqus) was selected for the damage initiation criteria. In this case the Ultimate Strength was selected to be the limiting factor. Fig 9 shows how the Ultimate Tensile Strength (UTS) changes with temperature. The $UTS(T)$ equation is only valid for $200^{\circ}\text{C} < T < 371^{\circ}\text{C}$ [18]. For values between 371°C and the melting point the UTS values were set to vary approximately in a linear way from 24 MPa at 371°C to 0 MPa at melting point.

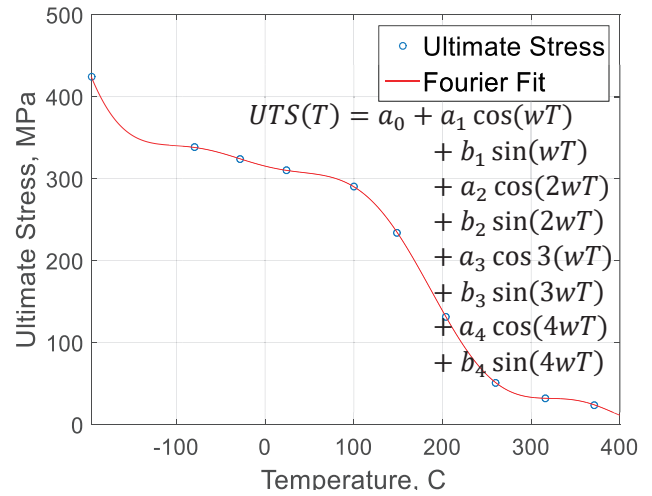


Fig. 9 Ultimate tensile stress Fourier Fit, where $a_0=354.9$, $a_1=-39.07$, $b_1=-337.9$, $a_2=-53.99$, $b_2=222.3$, $a_3=101.9$, $b_3=-32.45$, $a_4=-48.51$, $b_4=-13.3$, $w=0.006146$.

The fracture energy was used for the damage evolution criteria. Fracture energy was estimated using the relationship

$$G_{IC} = \frac{K_{IC}^2}{E} \quad (6)$$

where $G_{IC}=24.2$ kN/m is fracture energy, K_{IC} is fracture toughness, and E is Young's modulus [17].

The XFEM analysis is more complex than the TES analysis. A two-step analysis was used in this simulation instead of one (the TES analysis is just one step). In the first step, the same initial conditions were prescribed but in the second step the temperature field history was imported from the TES analysis. In this case the analysis was static in order to get the 3D stresses.

3. RESULTS AND VALIDATIONS

Fig.10 shows the electric current density vectors. Since the current cannot go through the crack, it detours around the crack tip, making the ECD almost 4 times greater than the 3.2 A/m², at the crack tip. Fig. 11 shows the temperature distribution at $t=1.0$ ms, where the maximum temperature is reached.

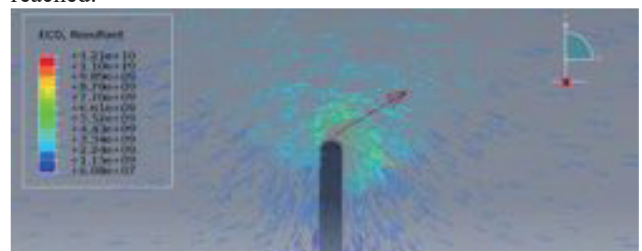


Fig. 10 Electrical Current Density Vectors at $t=1.0$ ms.

The temperature distribution in Fig. 11 shows how rapidly the temperature falls from the tip of the crack to the opposite side of the crack.

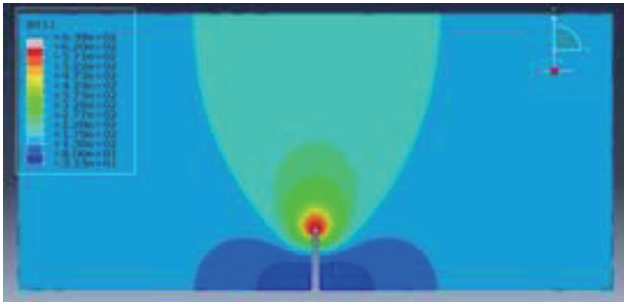


Fig. 11 Temperature field at $t=1.0\text{ms}$.

The corresponding Von Mises is shown in Fig. 12, and Fig. 13 shows the stresses along the X axis and it can be seen that the expansion of the sample is greater in the hotter zones, forcing the material to push outwards, therefore making the hotter regions a compressive one, while other regions are under a tension load. Since the heat distribution is dependent on time, the stress field is also dependent on time. At the beginning of the simulation the region that is closest to the crack tip is under compression. As we move upwards in the Y direction, the stress changes into a tensile region. As the sample continues to heat up, the compressive region expands and the tensile region move upwards.

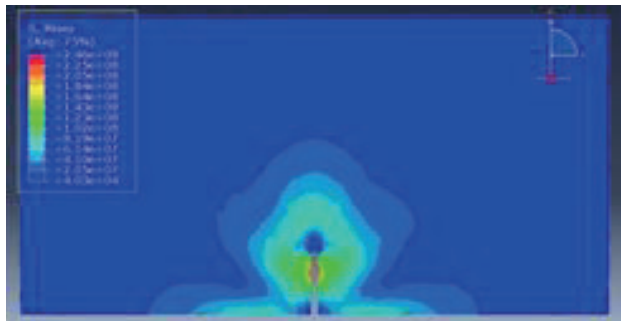


Fig. 12 Stress Field. Von Mises Temperature field at $t=1.0\text{ms}$.

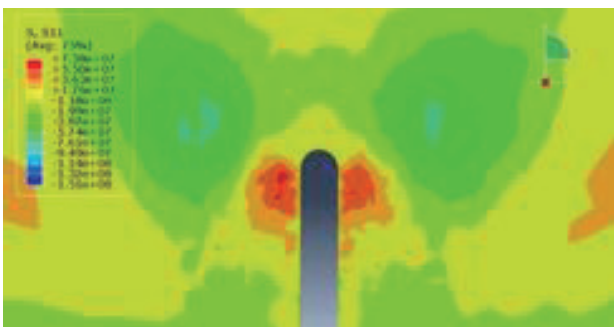


Fig. 13 Tensile Stress field (X direction) at $t=1.0\text{ms}$.

Fig.14 shows the experimental results. As we can see the melted area cannot be clearly observed in Fig. 14a. In order

to examine the melted area more clearly, the sample had to be polished until it had a mirror finish.

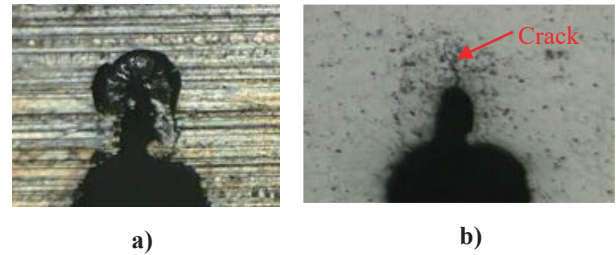


Fig. 14 Crack tip after electropulsing treatment. The melted area has an approximate diameter of 0.06mm .

The grey contour in Fig. 15 represents the melted area obtained from Abaqus. A more accurate simulation would be to delete the element that have failed, but element deletion is not possible without the implementation of subroutines that required additional software. We can compare the melted area in Fig. 15 to the melted area in Fig. 14 and see how the Abaqus can predict accurately the size of the melted area with approximately 0.01mm difference in diameter between the two.

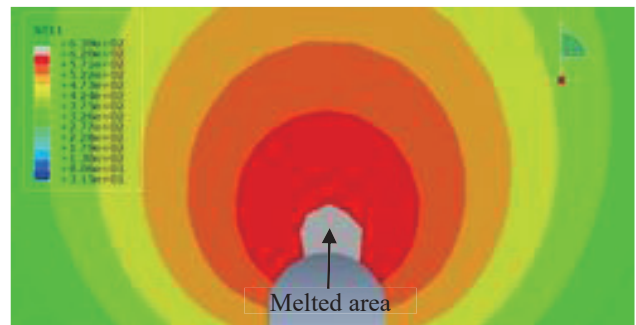


Fig. 15 Melted area in grey.

A micro vickers hardness test was performed near the crack tip to see if the temperature field has an effect on the hardness. The result of 120 Vickers test are shown in Fig. 17. The hardness varies in the same manner as the temperature field near the crack tip. Fig. 16 shows the area tested.

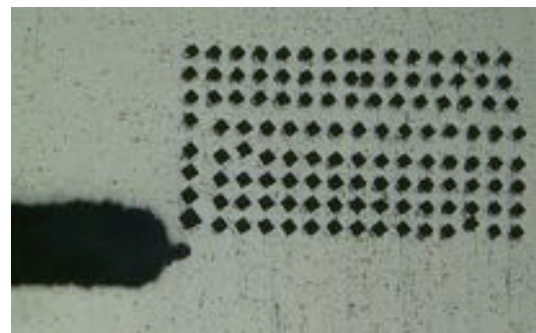


Fig. 16 120 Vickers test near the crack tip.

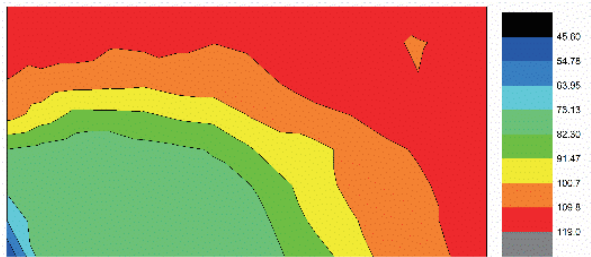


Fig. 17 Hardness profile. The units on the legend are HV.

The result of the XFEM model is shown in Fig 18. It can be seen that damage initiates near the tip of the crack. That is the region more likely to fail, and crack to propagate. In Fig. 14b, a crack appears at the tip of the melted area.

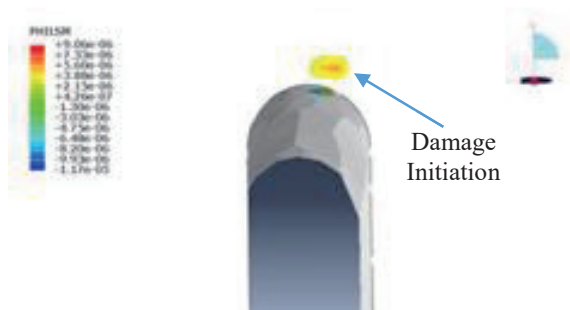


Fig. 18 Damage initiation.

4. CONCLUSIONS

Thermo-Electric-Structural and XFEM analyses were developed for an Al 6061-T6 sample, 0.5mm thick with a single-edge crack of 0.140mm wide and 1mm. The proposed FEM model considers the temperature-dependent material properties for Al 6061-T6. In addition, a damage initiation model was also completed.

The temperature gradient causes considerable internal stresses in the sample. However, the stress field can also be affected by the displacement boundary conditions. With the model the stress field can be obtained near the crack to perform further analysis where the stress state is necessary.

The melted area obtained from the simulation is nearly identical to the size of the melted area obtained in the experiment. The agreement of the temperature field obtained with the simulation can also be seen in the Vickers hardness test as both share the same profile.

The damage initiation model needs to be more precise, it predicts damage approximately in the same location where the crack is present after the electropulsing treatment but it fails to propagate the crack in the right direction. It was observed that that crack does not appear in all of the tested samples. It could appear because the loading conditions vary enough from experiment to experiment (mounting conditions of the sample, pre-existing stresses when it mounted in the testing setup, possible damage with it being polished), so these changes have to be included in the model as well.

This report provided a comprehensive FEM model for electropulsing treatment for crack arresting and it can be used as a foundation for further studies of other materials and/or different configurations.

ACKNOWLEDGEMENTS

This work was supported by all the people involved in the JUACEP program. The author is grateful to the Ju Lab and Lin Yang for her contributions to this work.

REFERENCES

- [1] Lu, S. K., Yi, X. H., Yu, L., Jiang, Y. L., Wei, W. R., 2011 SREE Conference on Engineering Modelling and Simulation, of the simulation and experimental fatigue crack behaviors in the aluminum alloy HS6061-T6, Procedia Engineering, Volume 12, Pages 242-247, ISSN 1877-7058 (2011).
- [2] Wei, S., Wang, G., Deng, D. et al. Appl. Phys. A 121: 69. doi:10.1007/s00339-015-9383-x (2015).
- [3] Golovin, Y. I., Finkel, V. M., Sletkov, A. A., Strength Mater. 9, 204 (1977).
- [4] Chakherlou, T. N., Shakouri, M., Aghdam, A. B., Akbari, A., Mater. Des. 33, 185 (2012).
- [5] Yamashita, Y., Kawano, T., Mann, K., J. Nucl. Sci. Technol. 38, 891 (2001).
- [6] Pinkerton, A. J., Wang, W., Li, L., J. Eng. Manuf. 222, 827 (2008).
- [7] Yanyan, W., Mingxu, Z., Daqing, F., Fatigue Fract. Eng. Mater. Struct. 16, 363 (1993).
- [8] Shin, C. S., Cai, C. Q., Int. J. Fatigue 30, 560 (2008).
- [9] Yu, J., Zhang, H., Deng, D., Liu, Q., Hao, S., Int. J. Adv. Manuf. Tech. 1 (2014).
- [10] Gallo, F., Satapathy, S., Ravi-Chandar, K., Electromagn. Launch Tech. 573 (2008).
- [11] ABAQUS 'ABAQUS/CAE 6.11 User's Manual'. Online Documentation Help: Dassault Systèmes (2011).
- [12] Wang, B., Hilali, S. Y., Electro-Thermal Modeling Using Abaqus, Abaqus Users' Conference (1995).
- [13] Seli, H., Awang, M., Ismail, A. I., Rachman, E., Ahmad, Z. A., Evaluation of properties and FEM Model of the Friction welded mild Steel-Al6061-Alumina. Mat. Res., São Carlos, v. 16, n. 2, p. 453-467 (2013).
- [14] Mills, K. C., Recommended Values of Thermophysical Properties for Selected Commercial Alloy, Woodhead Publishing Limited (2002).
- [15] Kuphaldt, T. R., Temperature Coefficient of Resistance (2016).
- [16] Lienhard IV, J. H., Lienhard V, J. H., A Heat Transfer Textbook, Phlogiston Press (2016).
- [17] Weaver, C. M., Rigg, P. A., Cordes, J. A., Hayes, A., XFEM Analyses of Critical Cracks in a Pressure Tap for a 40mm Gun Breech, SIMULIA Customer Conference (2011).
- [18] Holt, J. M., Structural Alloys Handbook, 1996 edition, Technical Ed; C. Y. Ho, Ed., CINDAS/Purdue University, West Lafayette, IN (1996).
- [19] Valencia, J. J., Quested, P. N., Thermophysical Properties, ASM Handbook, Vol 14, p 468-481 (2008).

MECHANICAL PROPERTIES OF LIPID VESICLE STUDIED BY MOLECULAR DYNAMICS SIMULATIONS

Chen-Hsi Huang

Department of Materials Science and Engineering, Graduate School of Engineering, University of California, Los Angeles
skyhuang@ucla.edu

Wataru Shinoda

Department of Applied Chemistry, Graduate School of Engineering, Nagoya University
w.shinoda@apchem.nagoya-u.ac.jp

ABSTRACT

Lipid vesicles are studied using Molecular dynamics (MD) simulations. Two sizes of vesicles are investigated: 1512- and 5000-lipid vesicles. Three properties including vesicle radius, number of inner water particles, and water density are calculated to probe whether the vesicles are in equilibration. The results show that 1512-lipid vesicles are close to equilibrium, while the 5000-lipid vesicle may need more time to get equilibrium. I then investigate the elastic response of vesicles by adding or removing water from inside. The results show the tension on vesicles is dependent on number of inner water. Lastly, I perform spherical harmonics analysis of the vesicles to obtain bending stiffness. The results show that the bending stiffness increases with increasing the vesicle size.

Undisclosed

Investigation of Time-Dependent Hemodynamics in Stented and Unstented Aneurysms

Ray Roman

Department of Mechanical Engineering, University of California, Los Angeles

rroman681@ucla.edu

Supervisor: Yasumasa Ito

Graduate School of Engineering, Nagoya University

yito@nagoya-u.jp

Abstract

While several studies have been performed to determine the effect of stenting on the hemodynamic flow within cerebral aneurysms, there is a paucity of research dedicated to the time-dependent hemodynamics located within the aneurysm itself. Furthermore, the peculiar behavior of stented flow versus unstented flow in aneurysms has been observed, but few phenomenological explanations have been offered. Computational fluid dynamics (CFD) was performed on stented and unstented aneurysm models of two sizes so that the flow behavior can be examined in detail. The results of the CFD simulations have shown that pressure plays a big role in characterizing the flow, especially in the case of stented aneurysms. On the other hand, it has been shown that the fluctuation of flow properties over time within the aneurysm itself does not lend itself clearly to any sort of phenomenological explanation behind aneurysm rupture.

Introduction

Flow diverter stents are a favorable option for treating intracranial aneurysms, and their success is attributed to its low invasiveness compared to conventional, albeit riskier and more invasive, treatment options such as endovascular coiling (11, 17). In particular, these devices seek to alter

the hemodynamic conditions to promote thrombosis (13). They also boast modest success in mitigating the risk of aneurysm rupture when treating large (10 mm to 25 mm in diameter) or giant (≥ 25 mm in diameter) aneurysms (14). Not to be ignored, however, are some potential complications as a result of using flow diverter stents including the risk of stent creeping or delayed aneurysm rupture (3, 4). Furthermore, holistic clinical results from using flow diverter stents appears tepid at best (1, 14).

A natural starting point for understanding the limitations of flow diverter stents would be to investigate the behavior of blood as it flows through and near a stent. Some studies (e.g., Jing et al. (4), Wu et al. (16)) examine the flow characteristics through the neck of a stented aneurysm. An alternative perspective is to focus not on the neck, but on the body and dome of the aneurysm, as aneurysm rupture may tend to originate from those places (9, 10). Identifying areas of large fluctuations in the mechanical properties is important in finding the most important areas to examine from a time-series perspective.

Various hemodynamic parameters are defined to better characterize the pathology of aneurysm formation and even the potential of aneurysm rupture. Two important parameters in this experiment are the wall shear stress, wss, and the aneurysm formation index, AFI. The wss describes the frictional effect that blood flow imparts on vessel walls,

TABLE 1: Flow characteristics.

Characteristic	Condition
viscosity	$3.17\text{E-}3$ Pa s
density	1050 kg m ⁻³
flow	pulsatile
model	rigid
inlet pressure	no gradient
outlet pressure	0 Pa
Δt	0.01 s

owing to both the viscosity of blood and velocity gradient:

$$WSS = \mu \frac{d\mathbf{u}}{dr}. \quad (1)$$

Surprisingly, it is hard to ascertain the “golden” value for wss that curbs aneurysm development: As summarized in (7), both low and high values of wss correlate to aneurysm formation and rupture, where high wss may exacerbate weak vessel walls, while low wss may trigger a chronic inflammatory response, leading to an atherosclerotic response and eventual aneurysm formation (5, 8).

The AFI describes the flow based on the observation that aneurysm formation may be correlated to the directional fluctuation of the wall shear stress over time (6). It is computed as follows:

$$AFI = \frac{WSS_i \cdot \overline{WSS}}{|WSS_i| * |\overline{WSS}|}, \quad (2)$$

where WSS_i denotes the wall shear stress at time i , and \overline{WSS} denotes the time-averaged wall shear stress. Though these properties are important in a static context, a careful examination of their variation over time could clue into important physiological consequences.

Methods

Methodology background

Four different models were tested with numerical simulations. Each model exhibited the same horseshoe-shaped configuration with the aneurysm located at the apex (henceforth referred to as an “outside” configuration). The cases

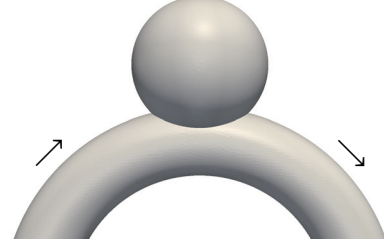


FIGURE 1: Sample model. Arrows indicate the direction of flow.

included an 8 mm diameter aneurysm with and without a stent, and a 12 mm diameter aneurysm with and without a stent. A prototypical model is shown in Figure 1. Following a similar measurement notation to the one in Seshadhri et al. (13), the specific dimensions of the aneurysm model were as follows: The parent vessel diameter was $d = 4$ mm and a maximum neck width was $N = 5.66$ mm. The aneurysm diameter was either $D = 8$ mm or $D = 12$ mm, and the neck-to-dome length was either $H = 6.82$ mm or $H = 11.48$ mm. Particular to the “outside” configuration, the inlet and outlet branch lengths were 150 mm, and the branch radius was 9.55 mm. The stent that was chosen for these simulations was the pipeline embolization device (PED), a particular type of flow diverter stent that has shown promising results in a clinical context (1, 12). Additionally, in the context of the experiment, the pipeline stent is preferred over other flow diverter stents (for example, Silk), because the former is a preferred option for treating large aneurysms (11). By modifying the dimensions of the rhombus-shaped pores in the PED, a porosity of 31.1 % was obtained (15).

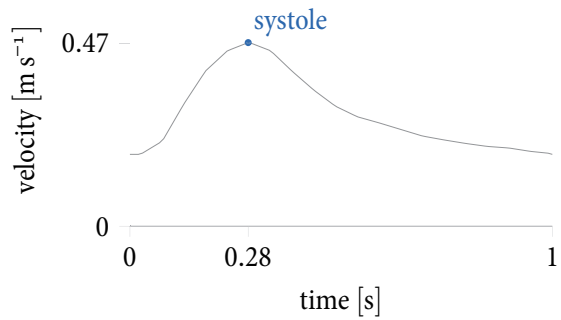


FIGURE 2: Pulse waveform, averaged from actual clinical data over one second.

To reduce the computational cost of performing simulations on an extremely fine mesh, the large eddy simulation (LES) model was used, while the wall-adapting local eddy-viscosity (WALE) model was used on the subgrid scale (with the model parameter $C_w = 0.544$). For the simulations, blood is assumed to be a Newtonian fluid. The flow conditions as well as the fluid properties are described in Table 1. As the flow was modeled to be pulsatile, the flow rate pattern was obtained by averaging real-life clinical data, the result of which is shown in Figure 2. Note that the waveform was averaged in order to last the duration of one second.

Numerical simulations

The computational meshes were finalized using SolidWorks, and using the methodologies described earlier, the simulations were performed using the computational fluid dynamics software OpenFOAM. Each model was then examined using the visualization software ParaView.

Holistic examination of each model consisted of taking images of various parameters at $t = 0.2 \text{ s}, 0.28 \text{ s}, 0.4 \text{ s}, 0.5 \text{ s}$. The full-body aneurysm was visualized for the AFI and wss. Additionally, slices were taken at the midplane (normal parallel to the z -direction) to visualize the blood velocity and blood pressure contours, and slices at the neck were required to visualize the flow rates entering and leaving the aneurysm.

Visualizing the time-dependent hemodynamics required the sampling of a few points located on the aneurysm wall as well as within the body. The center plane of the aneurysm was sliced (normal in the y -direction), and seven points were deliberately selected to examine their time-dependent behavior. Three sets of pairs of points (one on the surface and one close to the surface point chosen) were chosen as well as the center point. Of these points, two pairs were selected at or near the distal wall (coinciding where the AFI is shown to fluctuate rapidly in the stentless case), and one pair was selected at the proximal wall. Using the data visualization program ParaView, the AFI, wss, velocity \mathbf{u} , and pressure p were recorded over all time steps for each point.

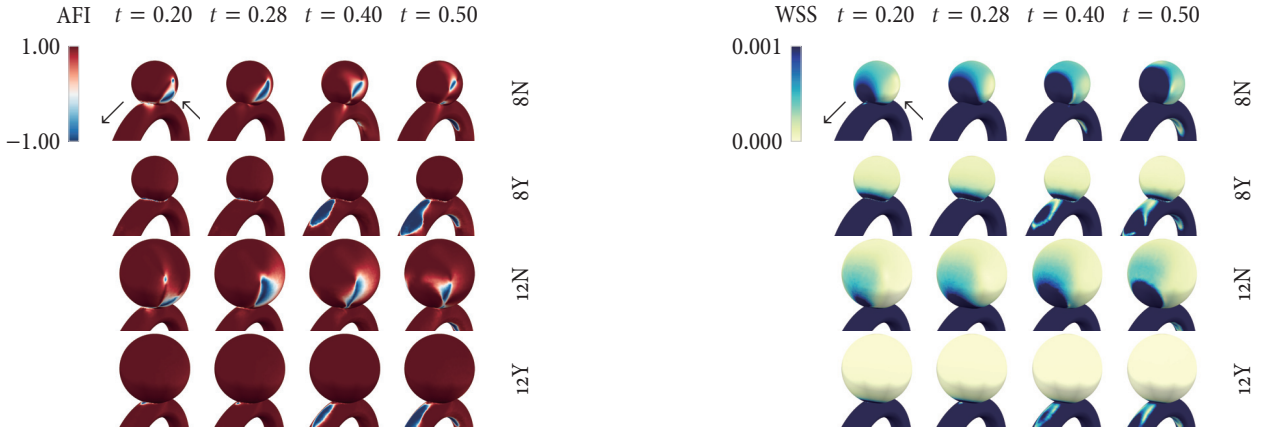
Results

Several sets of images were obtained. Figure 3 show the AFI and the wss for the selected time steps. The AFI for all cases range from $-1 \leq AFI \leq 1$. The wss for all cases fall in the range $0 \text{ kPa} \leq WSS \leq 0.001 \text{ kPa}$. For all cases, the heatmaps for the magnitude of the velocity vector (Figure 4b) were aptly represented in the range $0 \text{ m s}^{-1} \leq \|\mathbf{u}\| \leq 0.7 \text{ m s}^{-1}$. In examining the u_y component in the neck plane, the 8 mm illustrative range was found to be between -0.1 m s^{-1} to 0.1 m s^{-1} , and for 12 mm -0.15 m s^{-1} to 0.15 m s^{-1} . The heatmaps for pressure have a case-dependent representative domain; the ranges are illustrated in Figure 4a. As shown in the bottommost plot of Figure 4a, all four models exhibit higher pressures before and at peak systole than after.

With respect to the center plane images, the unstented models' flow patterns shows a counterclockwise flow into the aneurysm, entering near the distal wall, following the curvature of the aneurysm dome, and then exiting at the proximal wall. This is in stark contrast to the flow patterns exhibited by stented models. In both stented models, the flow follows a clockwise pattern, the fluid entering near the proximal wall, following the curvature of the aneurysm, and then exiting at the distal wall.

In Figure 5, the flow rates and the y -component of neck velocity are shown. With regards to the flow rate (Figure 5a) right before the peak, the regions of high velocity are centered in the middle of the neck, but across the transition into late diastole, the region of high velocity moves closer to the distal wall. For the models with the PED, the regions of high velocity are located close to both walls rather in the center, and this pattern remains relatively unchanged from early systole to late diastole. Overall, the stented cases appear relatively lighter than the unstented cases, though this pattern seem much more unchanging over the course of one pulse.

Looking specifically at the y -directional variation on the neck (Figure 5b), the pattern is more detailed. For the unstented cases, the region of high velocity in the center (colored red, at $t = 0.2 \text{ s}$) is shown to be one of positive y -velocity, namely fluid is entering the aneurysm primarily in the center. On the other hand, fluid exits the aneurysm in a halo-like shape around this region (as coded in blue).



(A) Aneurysm formation index for each time step.

(B) Wall shear stress for each time step.

FIGURE 3: Selected hemodynamic properties. Note that for both sets of images, the distal wall is facing front.

The stented cases, on the other hand, are fixed in terms of fluid entrance and exit. Fluid enters at the proximal wall and exits at the distal wall, though the intensity of fluid entry or exit appears to decrease over time.

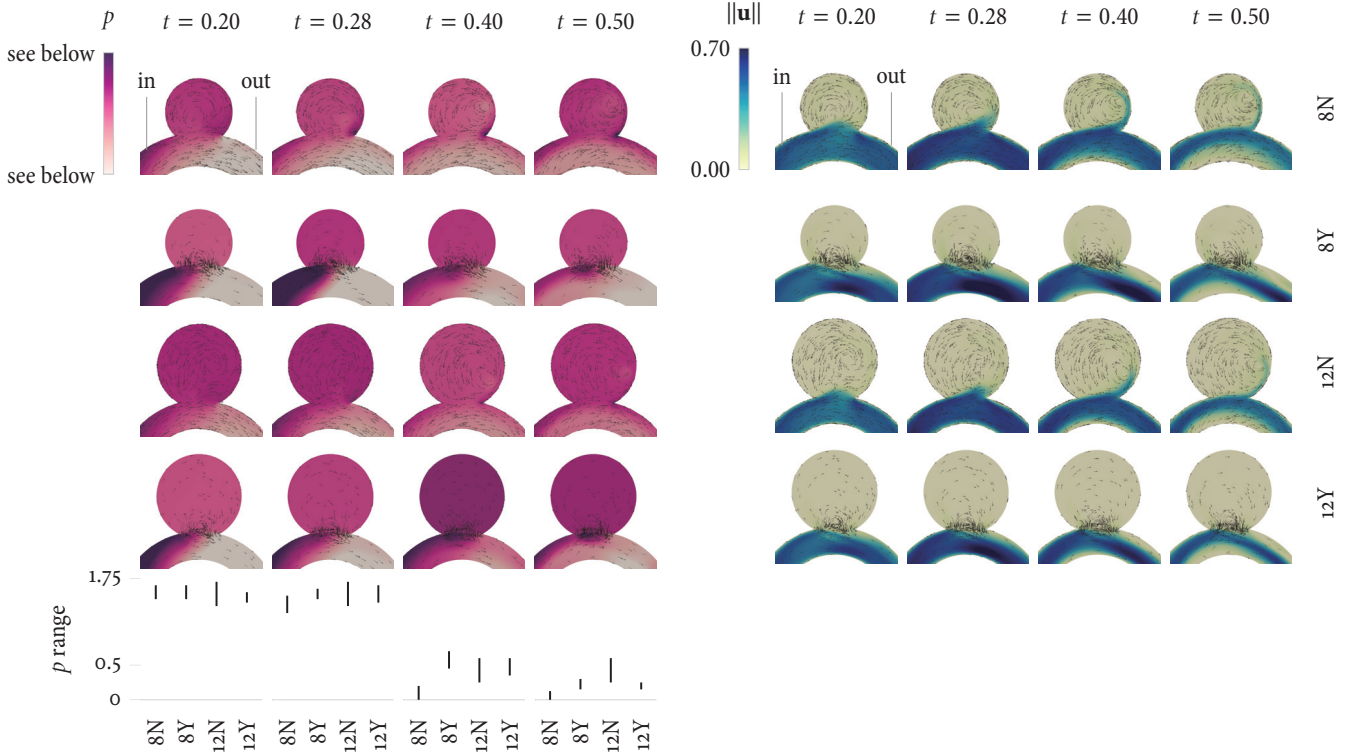
The time-dependent patterns, as shown in Figure 7, show much similarity. The inner points exhibit little to moderate variation over one second. The range for the velocity components for all cases is shown to be $-0.04 \text{ m s}^{-1} \leq u_i \leq 0.02 \text{ m s}^{-1}$. The magnitude of velocity is shown to fall between $0 \text{ m s}^{-1} \leq \|\mathbf{u}\| \leq 0.07 \text{ m s}^{-1}$. The center point, colored gray in Figure 7 shows a high degree of fluctuation in the no stent cases for both 8 mm (in $u_x, u_y, \|\mathbf{u}\|$) and 12 mm (in $u_y, \|\mathbf{u}\|$).

The points on the wall were recorded for their wss and AFI values as well as pressure. In the unstented cases, the AFI fluctuates from $AFI = 1$ before the systole, to $AFI = -1$ at peak systole, then up again for the rest of the pulse. Much less dramatic than the no stent cases, the models fitted with the PED stay at $AFI = 1$ up through halfway the entire pulse, only to taper near the one second mark. On the opposite end of the aneurysm, the proximal point paints a different picture. Showing little variation, the proximal point that was selected stays at $AFI = 1$ for roughly the entire time step for all cases. These same observations are present in the actual snapshots of the model, as discussed previously.

Discussion

It is clearly seen in Figure 3 that the AFI for both unstented cases exhibit a more dynamic variation, whereas both stented cases appear to have $AFI = 1$ on the entire body. Interestingly, the descending parent vessel appears to be more dynamic in the AFI values for the aneurysms fitted with a PED. A similar observation is made for the wall shear stress. The distal wall experiences high wss for the unstented cases (as can be confirmed by the plots as well); for the stented cases, there is almost no notable change in wss except on the parent vessel.

In viewing Figure 4, the heatmaps tell an interesting story. The velocity maps in Figure 4b show a region of high velocity jetting into the aneurysm body and striking the distal wall in the stented cases; for the unstented cases, however, the magnitude of velocity appears uniform in the entirety of the aneurysm body. The pressure maps in Figure 4a are more noteworthy. Over the course of one cycle, the pressure ranges that were required to achieve brightness constancy in the midplane images drops dramatically from $p \sim 1.6 \text{ Pa}$ to $p \sim 0.25 \text{ Pa}$. This variation may be explained by decreasing inflow velocity over the course of the pulse. While there may be a more rigorous explanation as to the difference in stentless–stented and 8 mm–12 mm dichotomies, too few time steps were sampled to make any significant hypothesis.



(A) Shading represents the pressure.

(B) Shading represents the magnitude of the velocity.

FIGURE 4: Center plane visuals. Note for the bottom figure, the plot represents the pressure range.

Looking more closely at the neck in Figure 6, the pressure may play a significant role in the hemodynamic pattern. As shown, there is a negative pressure gradient surrounding the pores of the aneurysm; the encroaching flow enters the aneurysm at the nearest availability (closest to the proximal wall), thus beginning the flow pattern that is observed overall in the stented cases. Thus it may be said that the idiosyncratic flow into the aneurysm for the stented cases is driven primarily by pressure. This observation confirms the pressure-driven model as described in Bouillot et al. (2), but in this experiment the model has been confirmed for aneurysms of normal and large size as well as in an outside configuration. The pressure-driven model may also explain why the magnitude of fluid inflow to and outflow from the aneurysm in the stented case is relatively lower than in the stentless cases. The observations found in Figure 5 also support the pressure-driven model, as there is a noticeable difference in how the fluid behaves in the

stented cases versus the unstented cases: In the unstented cases, there is a prominent region of fluid entry, which shuttles closer to the distal wall over one cycle; the stented cases are much more constant, with a counterclockwise motion as described previously.

As components of the velocity vector were sampled, there was no unexpected pattern, save for the out-of-plane behavior of the fluid. The magnitude of the velocity shows more variation at the center than at the points closer to the edges, which may be attributed to the erratic flow in the u_x and u_y directions, as the flow tends to move in a counterclockwise manner. Additionally, since the center point is the farthest point in the midplane from all the walls, there is less shear stress-induced attenuation of the velocity components. As the flow continues in the positive x -direction, the values for u_z appear to vary primarily based on the location of the point that was chosen rather than the fact that a stent is or is not present. In particular, the

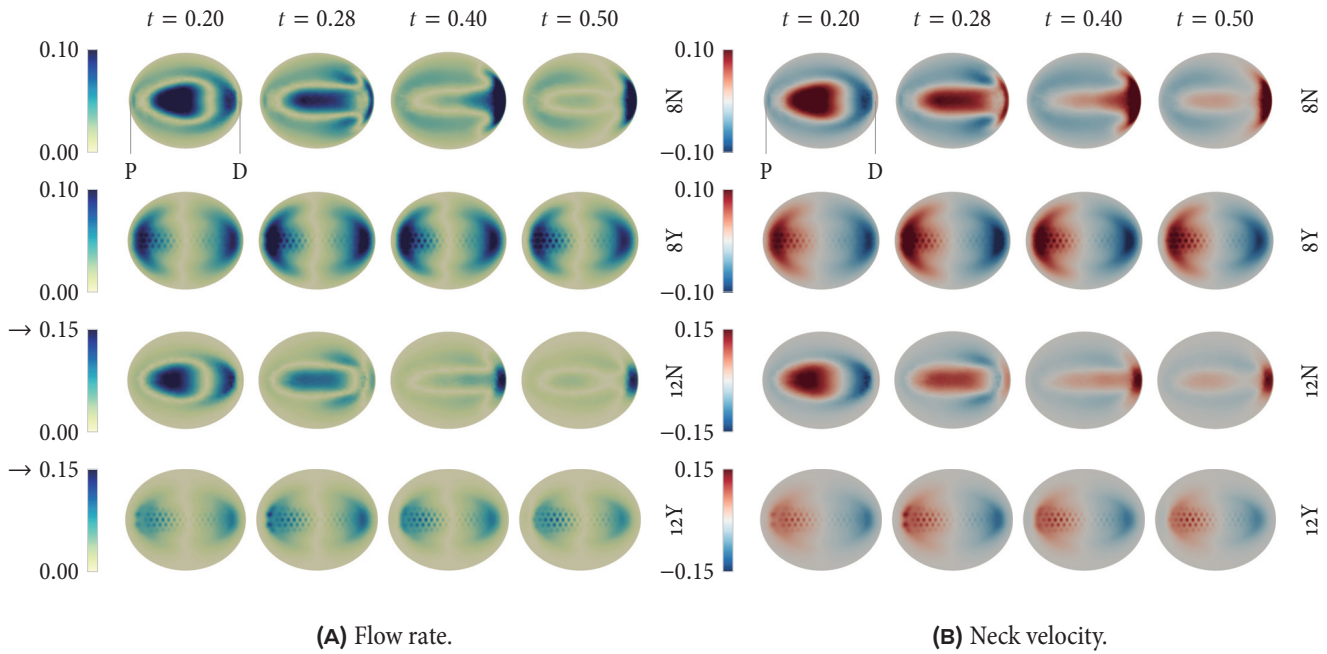


FIGURE 5: Neck slices featuring flow rate and neck velocity. “P” stands for proximal, “D” for distal.

u_z plot for the 12 mm no stent model shows a symmetry about the x -axis for both distal points that were selected.



FIGURE 6: Neck detail of pressure contour in 8 mm stented case at $t = 0.28$ s.

Also noteworthy, the stented cases for both sizes have much more reduced velocities than the no stent analog. Again, this may be related to the pressure-driven model, as the flow throughout the aneurysm in the stented cases is much more constant than in the no stent cases; however, this pattern may be reflective of the specific points chosen as opposed to some hard and fast rule. And as stated earlier, the pressure is virtually the same for all cases for all points.

The points on the surface of the aneurysm also tell an interesting story. Overall, both the aneurysm formation index and the wall shear stress show great variation (though more so for the unstented case with respect to the wall shear stress). In the unstented cases, the wall shear stress, for all components and the magnitude, have large variations after the systole. The values for each point for WSS_x show little deviation from each other, whereas there is a stark difference present between the proximal points and the distal points for the WSS_y and WSS_z components. The time variation of AFI values for the unstented cases are much more dramatic than for the stented cases, though only for distal points. This is also reflected in the visual time series of the AFI on the aneurysm body, as the stented cases have very little change in AFI on the body itself.

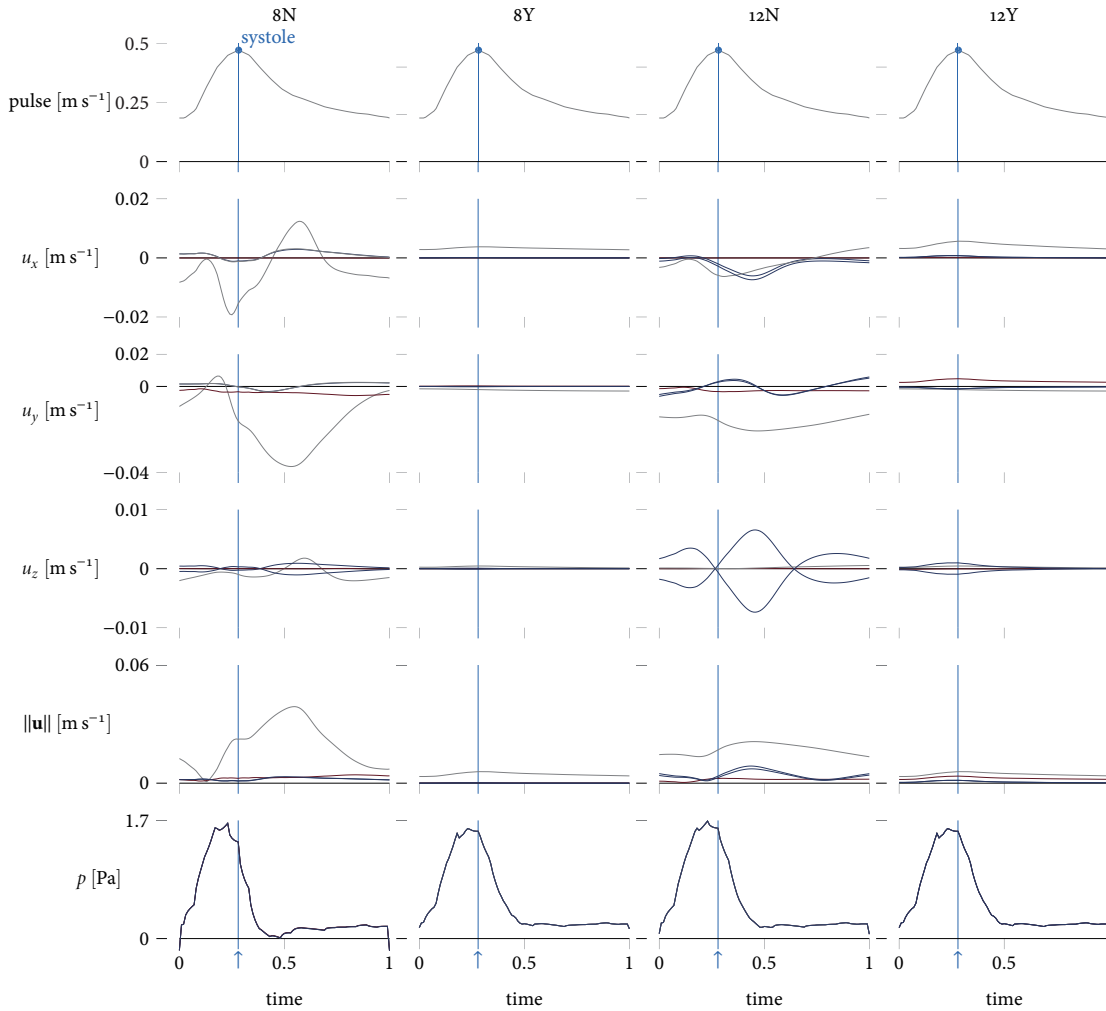


FIGURE 7: Time-dependent flow characteristics of inner points. Red denotes the curve at the proximal points, and blue at distal points. Gray is at the center. All lines coincide in the pressure plot.

Two conclusions can be drawn from the data overall. First, pressure plays a considerable role in driving blood flow, and the pressure patterns unique to PED-treated aneurysms is a suitable explanation for the quirky behavior that was observed. Second, the flow patterns within the aneurysm itself do not appear to show any hint towards rupture-related pathology. Any sort of large, notable fluctuations in the flow pattern could hint at an underlying mechanism related to aneurysm rupture; however, none were observed.

Conclusion

To summarize, pipeline embolization devices may be an attractive option for the treatment of aneurysms of normal and large sizes as they reduce the blood inflow rate as well as homogenize the flow over one pulse. A pressure-driven model may explain the unique flow pattern observed in aneurysms treated with stents. Additionally, the fluid appears to behave less erratically in those cases as well, which may be one factor in generating thrombogenic conditions as a result of treatment. Though some variation in flow was exhibited, there does not appear to be any time-dependent

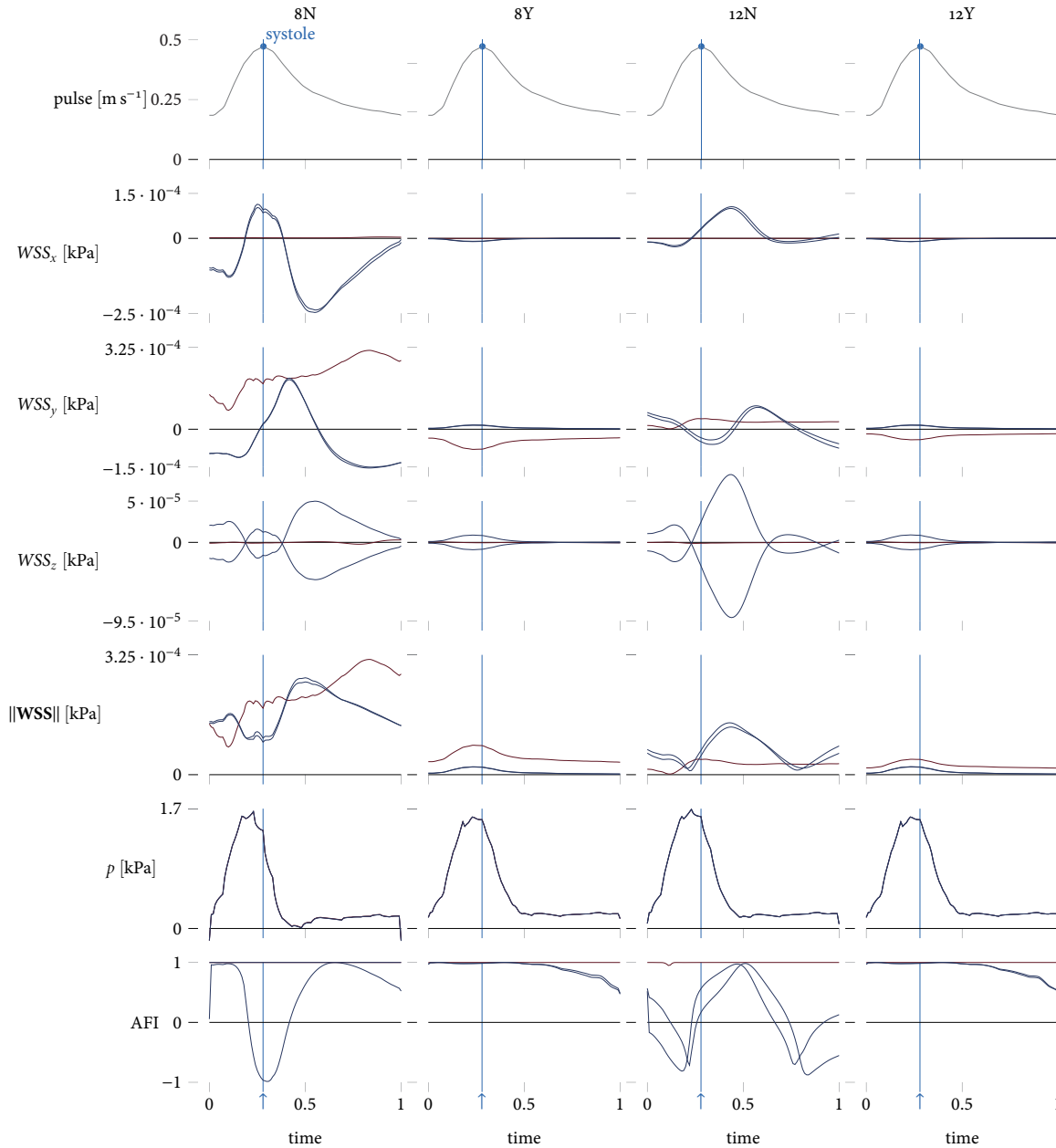


FIGURE 8: Time-dependent flow characteristics of outer points. Red denotes the curve at the proximal points, and blue at distal points. Gray is at the center. All lines coincide in the pressure plot.

phenomenological explanation as to aneurysm rupture.

References

- [1] Armoiry, X., Paysant, M., Hartmann, D., Aulagner, G., and Turjman, F. (2012). Interest of flow diversion pro-
- theses in the management of unruptured intracranial aneurysms. *International Journal of Vascular Medicine*, 2012:1–5.
- [2] Bouillot, P., Brina, O., Ouared, R., Lovblad, K.-O., Farhat, M., and Pereira, V. M. (2015). Hemody-

- dynamic transition driven by stent porosity in sidewall aneurysms. *Journal of Biomechanics*, 48(7):1300–1309.
- [3] Cohen, J. E., Gomori, J. M., Moscovici, S., Leker, R. R., and Itshayek, E. (2014). Delayed complications after flow-diverter stenting: Reactive in-stent stenosis and creeping stents. *Journal of Clinical Neuroscience*, 21(7):1116–1122.
- [4] Jing, L., Zhong, J., Liu, J., Yang, X., Paliwal, N., Meng, H., Wang, S., and Zhang, Y. (2016). Hemodynamic effect of flow diverter and coils in treatment of large and giant intracranial aneurysms. *World Neurosurgery*, 89:199–207.
- [5] Kim, M., Taulbee, B. D., Tremmel, M., and Meng, H. (2008). Comparison of two stents in modifying cerebral aneurysm hemodynamics. *Annals of Biomedical Engineering*, 36(5):726–741.
- [6] Mantha, A., Karmonik, C., Benndorf, G., Strother, C., and Metcalfe, R. (2006). Hemodynamics in a cerebral artery before and after the formation of an aneurysm. *American Journal of Neuroradiology*, 27(5):1113–1118.
- [7] Meng, H., Tutino, V., Xiang, J., and Siddiqui, A. (2014). High wss or low wss? Complex interactions of hemodynamics with intracranial aneurysm initiation, growth, and rupture: Toward a unifying hypothesis. *American Journal of Neuroradiology*, 35(7):1254–1262.
- [8] Meng, H., Wang, Z., Hoi, Y., Gao, L., Metaxa, E., Swartz, D. D., and Kolega, J. (2007). Complex hemodynamics at the apex of an arterial bifurcation induces vascular remodeling resembling cerebral aneurysm initiation. *Stroke*, 38(6):1924–1931.
- [9] Mohiaddin, R. H. (2010). Assessment of the biophysical mechanical properties of the arterial wall. In *Cardiovascular Magnetic Resonance*, pages 362–377. Elsevier BV.
- [10] Omodaka, S., ichirou Sugiyama, S., Inoue, T., Funamoto, K., Fujimura, M., Shimizu, H., Hayase, T., Takahashi, A., and Tominaga, T. (2012). Local hemodynamics at the rupture point of cerebral aneurysms determined by computational fluid dynamics analysis. *Cerebrovasc Dis*, 34(2):121–129.
- [11] Pierot, L. and Wakhloo, A. K. (2013). Endovascular treatment of intracranial aneurysms: Current status. *Stroke*, 44(7):2046–2054.
- [12] Saatci, I., Yavuz, K., Ozer, C., Geyik, S., and Cekirge, H. S. (2012). Treatment of intracranial aneurysms using the pipeline flow-diverter embolization device: A single-center experience with long-term follow-up results. *American Journal of Neuroradiology*, 33(8):1436–1446.
- [13] Seshadhri, S., Janiga, G., Beuing, O., Skalej, M., and Thévenin, D. (2011). Impact of stents and flow diverters on hemodynamics in idealized aneurysm models. *Journal of Biomechanical Engineering*, 133(7):071005.
- [14] Szikora, I., Berentei, Z., Kulcsar, Z., Marosfoi, M., Vajda, Z., Lee, W., Berez, A., and Nelson, P. (2010). Treatment of intracranial aneurysms by functional reconstruction of the parent artery: The budapest experience with the pipeline embolization device. *American Journal of Neuroradiology*, 31(6):1139–1147.
- [15] Tang, A. Y.-S., Chan, H.-N., Tsang, A. C.-O., Leung, G. K.-K., Leung, K.-M., Yu, A. C.-H., and Chow, K.-W. (2013). The effects of stent porosity on the endovascular treatment of intracranial aneurysms located near a bifurcation. *Journal of Biomedical Science and Engineering*, 06(08):812–822.
- [16] Wu, Y.-F., Yang, P.-F., Shen, J., Huang, Q.-H., Zhang, X., Qian, Y., and Liu, J.-M. (2012). A comparison of the hemodynamic effects of flow diverters on wide-necked and narrow-necked cerebral aneurysms. *Journal of Clinical Neuroscience*, 19(11):1520–1524.
- [17] Zhang, Y., Chong, W., and Qian, Y. (2013). Investigation of intracranial aneurysm hemodynamics following flow diverter stent treatment. *Medical Engineering & Physics*, 35(5):608 – 615.

PATH TRACKING USING LIDAR LOCALIZATION AND MAPPING

Itsui Yamayoshi

Department of Mechanical and Aerospace Engineering, Graduate School of UCLA
itsuiyamayoshi@ucla.edu

Supervisor: Tatsuya Suzuki

Graduate School of Engineering, Nagoya University
t_suzuki@nuem.nagoya-u.ac.jp

ABSTRACT

This report details the development and the results of a path tracking algorithm implemented on an electric vehicle utilizing a Velodyne LiDAR for sensing. The focus for the report is to understand the effectiveness of LiDAR to accomplish path tracking. LiDAR has an opportunity to provide an essential function for future autonomous vehicles: sensing of the immediate surroundings and environment through SLAM (Simultaneous Localization and Mapping). Thus, it is fundamental to examine its usage in a real environment. To this effect, a LiDAR utilized path tracking is executed on a test course and the resulting data is analysed to see how well the path is followed. Slight tuning of the path tracking algorithm is done to minimize the deviation from the path at higher speeds. The results are then evaluated to see the effectiveness of both the LiDAR localization process and the path tracking algorithm.

INTRODUCTION

Autonomous driving has become one of the big objectives for the 21st century as both the industries and the academia pursue to make it a reality. Path tracking is one of the fundamental functions that an autonomous vehicle would have to be able to accomplish and it has been researched extensively [1], [2], [3], [4]. Many of the research has detailed the benefits of different algorithms and has also shown the effectiveness of trajectory tracking in real life. However, many of these path tracking has been accomplished using information from sensors like: odometer, IMU, or GPS. While these sensors are sufficient to accomplish path tracking in controlled environments, for true autonomous driving, consideration has to be put for ever changing environments. To this effect, the LiDAR is indispensable. In tunnels and cities, the GPS signals can be obstructed and in bad weather conditions, the odometry data can be unreliable. During these kind of unfavourable conditions, there will be times where the vehicle will have to rely on another sensor, such as the LiDAR, to provide accurate information about its current state.



Fig. 1. Toyota's super-compact electric vehicle, COMS. The vehicle is mounted with the VLP-16 LiDAR on top, above the driver's seat. Two computers are also employed at the trunk, one for processing LiDAR data and another for using the generated information to provide control command to steer the car.

In this report, we address this specific problem by testing out LiDAR as the only sensor used to obtain localization information. This information will then be utilized in the path tracking algorithm. We have already seen the use of LiDAR in combination with other sensors in different researches and at the DAPRA Urban Challenge 2005 [5]. More recently, a localization technique using monocular cameras and LiDAR maps has been proposed [6]. These prior examination has shown the ability of LiDAR, in combination with other sensors and by itself, to be able to produce highly accurate localization information. Here, we retrace some basic functions using the LiDAR to build the groundwork for future use in the lab.

This report will begin by discussing the process of LiDAR localization and mapping. Then, a brief overview of path tracking is given. Afterwards, the experimental details and results are provided. Finally, an analysis and concluding remarks are given

LIDAR LOCALIZATION AND MAPPING

For this report, a Velodyne VLP-16 LiDAR was used on top of Toyota's super-compact electric vehicle, COMS. The accuracy on the LiDAR was +/- 3 cm with a range of 100 m and a vertical field of view of 30 degrees. The refresh rate used for the LiDAR was 10 Hz. All data from the LiDAR is initially processed by Autoware, an open source ROS program.

Due to the limitation of computational power, real time SLAM is not accomplished using the LiDAR. Instead, the environment is mapped beforehand and the localization data is obtained within an *a priori* known map. To accomplish this, the LiDAR first scans the environment and records the incoming data. Afterwards, the map is constructed through an iterative process in which a *Normal Distribution Transform* is completed. The basic premise of this process can be found in [7] for 2D cases. In short, a normal distribution is assigned to a cell, a subdivision of the scan area, representing the probability of measuring a point. Using this information, another scan data can be matched through the usage of Newton's algorithm. An extension of this technique for 3D cases is achieved through the Autoware program.

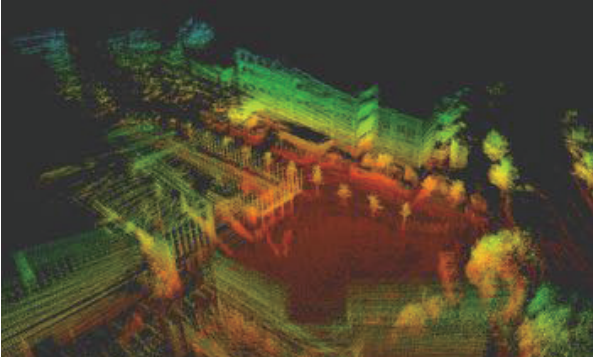


Fig. 2. A map generated from the LiDAR outside of the National Innovation Complex at Nagoya University.

From here, using the map generated after the initial LiDAR scan of the environment, NDT scan matching is used to infer the localization information and the state of the vehicle. This process has been used to successfully obtain localization data at places including: the university campus, inside a confined room, and a test course with few notable landmarks. Preliminary testing within a confined room has shown that the localization data can be trusted to an accuracy of 10 cm. Furthermore, the variety of environments that we have been able to perform accurate localization on has shown the effectiveness of the technique. Especially in the test course with few notable landmarks, the NDT matching method showed promise in being accurate and reliable enough to use on the path tracking algorithm.

PATH TRACKING ALGORITHM

For the purpose of this research, we used a path tracking algorithm similar to the *Pure Pursuit* method outlined in [8]. The algorithm does not take into account the dynamics of the vehicle and simply uses a kinematic vehicle model to determine the look-ahead point and eventually the goal point, a point in the predetermined path. The steering command is then determined so that it will take the current state of the vehicle towards that goal point. The basic idea behind determining the look-ahead point, the goal point, and the steering angle is discussed below.

To determine the look-ahead point, we first determine the current turn radius of the car, r . Since the COMS vehicle is a front-wheel drive car, it is easy to calculate the turn radius from the wheelbase w and the front wheel's angle α . The turn radius is then given by:

$$r = \frac{w}{\tan(\alpha)} \quad (1)$$

Using this information along with the change in heading of the vehicle ϕ , determined using the look-ahead distance, we can obtain the local position of the look-ahead x_L and y_L . In our case, the x-axis is towards the front of the car and y-axis is perpendicular to the up direction and the x-axis.

$$x_L = r \sin(\phi) \quad (2)$$

$$y_L = r (\cos(\phi) - 1) \quad (3)$$

After calculating the look-ahead position, we can then search through our path to find the path point closest to our look-ahead position. Using the local coordinate of the found goal point x_g and y_g , we can solve for the desired steer angle θ . To do this, we first obtain the curvature of the turn γ .

$$\gamma = \frac{1}{r_{desired}} = \frac{2}{x_g^2 + y_g^2} * y_g \quad (4)$$

$$\theta = \text{atan}(w\gamma) \quad (5)$$

With this, we can send a steer command to the vehicle. According to [8], as we make the distance of the look-ahead to be longer, we should see a smoother control at the expense of worse tracking accuracy. And, as we make the look-ahead distance shorter, we can expect better tracking accuracy with worse stability. Thus, the look-ahead distance and the gain for the steer command will be the main control parameters for our experiment.

RESULTS

Experiment on the path tracking was conducted on a private test course. The environment was filled with paved road amongst a surroundings of low laying grass. A hill enclosed the track on one side while a small river enclosed it from the other side. Unlike the Nagoya University campus, the amount of notable landmark was considerably less. The COMS vehicle was driven through the course initially to have the LiDAR prepare the map. Afterwards, a relatively simple circular path was generated by recording the points that the vehicle drove through. The path that we used was made so that each points were separated by approximately 0.5 meters.

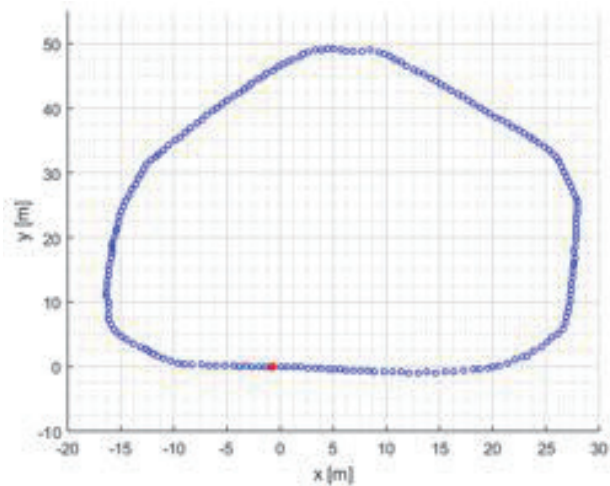


Fig. 3. The path to follow. Red point shows the starting point.

A total of 6 runs were recorded during our experiment. Each run followed the same path, but with some variation in the speed of the vehicle or the control parameters: the look-ahead distance and the proportional gain for the steering. Using the localization data obtained from the LiDAR, we evaluated how accurately the path was tracked. This was done by calculating the distance of the vehicle at each localization from the line created between 2 closest points in the path.

Table 1 Parameter Values and Maximum Error of Each Trial

Trial #	Speed (km/h)	Gain	Look-Ahead (m)	Maximum Error (m)
1	8	0.5	2	2.38
2	12	0.2	3	1.48
3	12	0.2	3	0.94
4	8	0.2	3	0.73
5	12	0.1	3	1.95
6	12	0.1	5	0.82

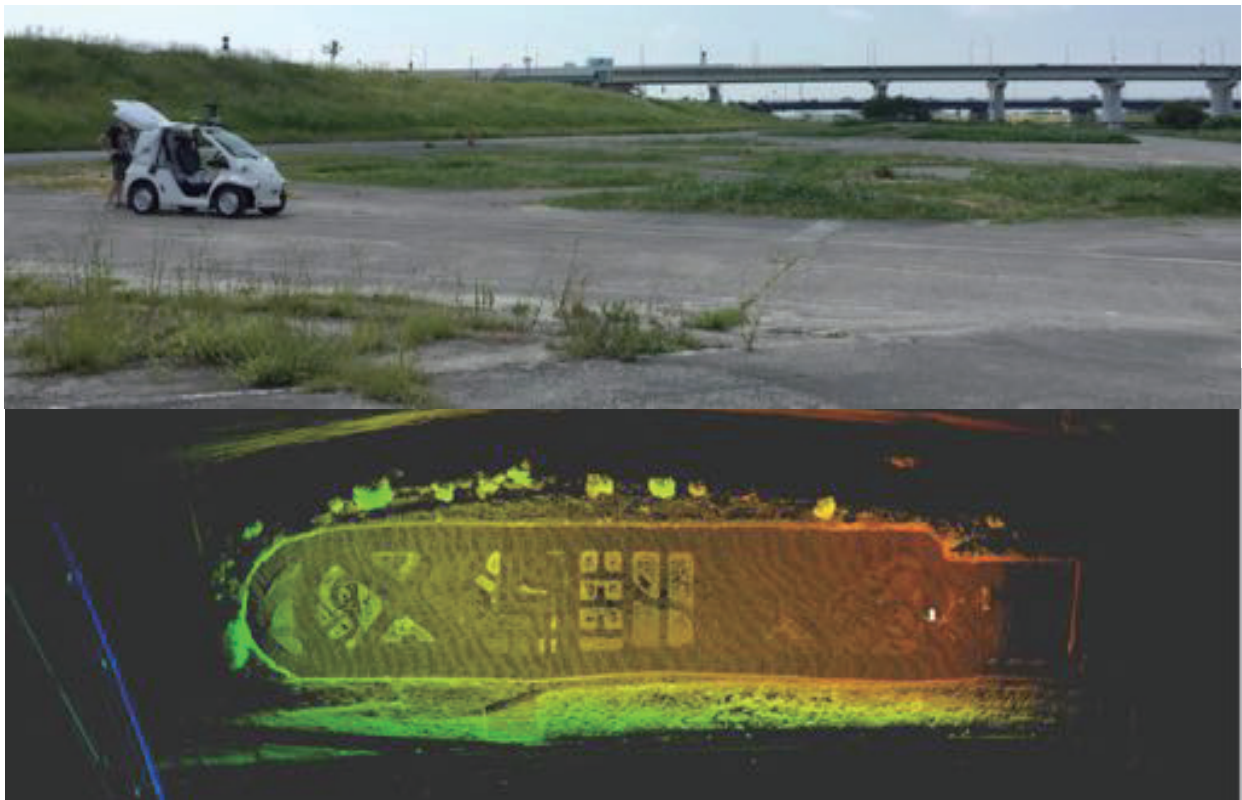
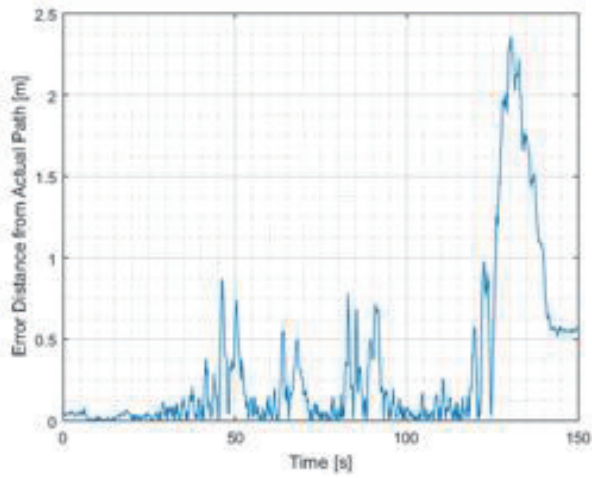
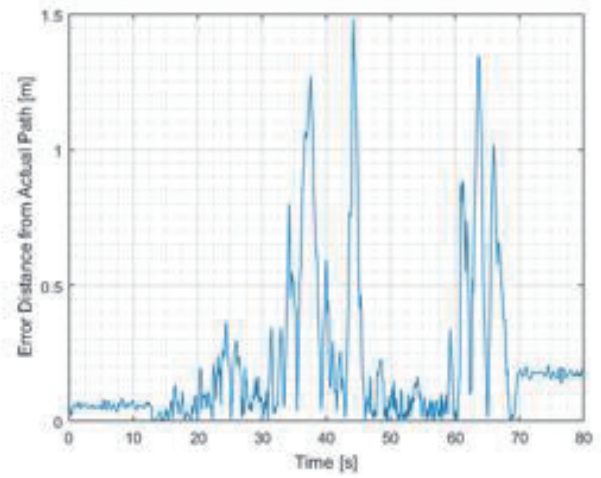


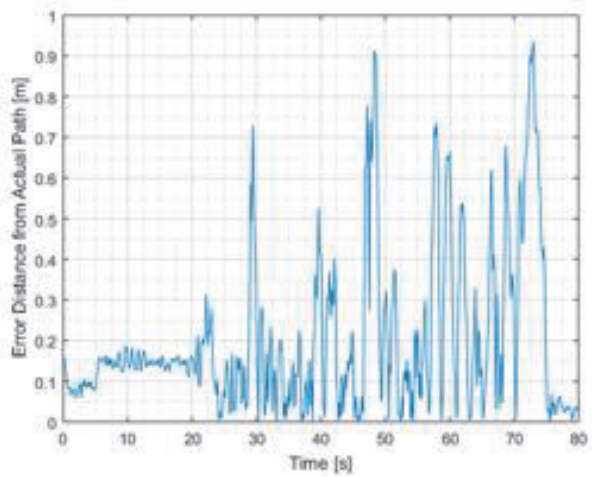
Fig. 4. The picture of test course is shown above and a top-down view of the LiDAR generated map is shown below.



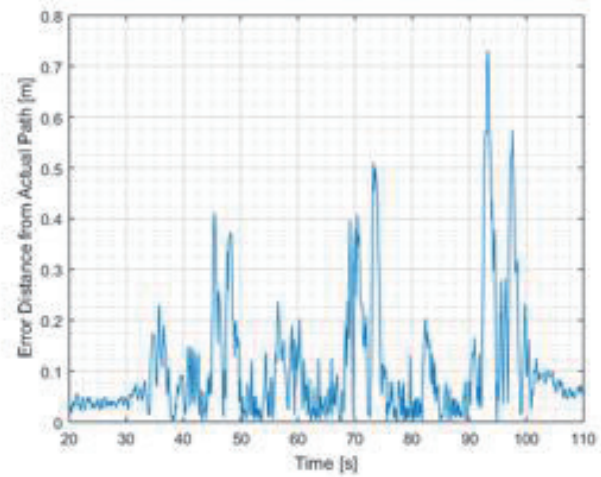
a) Speed = 8 km/h, Gain = 0.5, Look-Ahead = 2 m



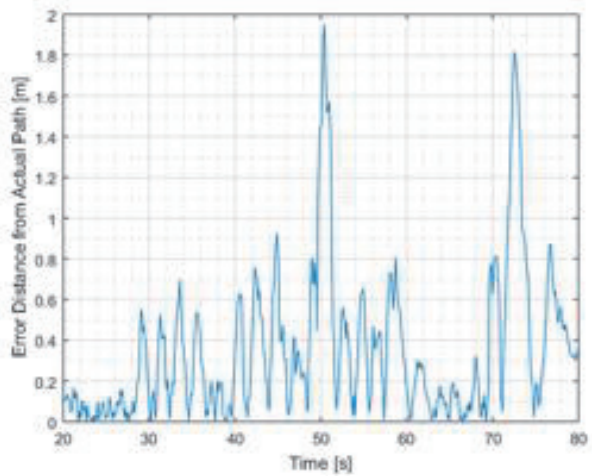
b) Speed = 12 km/h, Gain = 0.2, Look-Ahead = 3 m



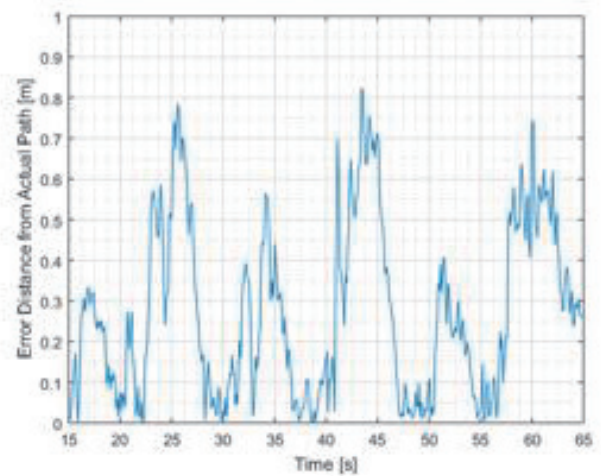
c) Speed = 12 km/h, Gain = 0.2, Look-Ahead = 3 m



d) Speed = 8 km/h, Gain = 0.2, Look-Ahead = 3 m



e) Speed = 12 km/h, Gain = 0.1, Look-Ahead = 3 m



f) Speed = 12 km/h, Gain = 0.1, Look-Ahead = 5 m

Fig. 5. The tracking error and the parameter values during each trial are shown above.

Looking at the results, we see that, in general, higher speed equates to higher values of tracking error for the system. This is probably the most notable pattern across all trials. If we increase the look-ahead distance we see a smoother ride, most visibly on the 6th trial. Decreasing the gain, in general, doesn't show a clear trend. This is most likely due to the fact that while the decrease in gain will reduce overshoot of the system, it results in a slower response. Hence, there is a competition depending on the speed of the vehicle and whether the path requires a significant change in orientation or not. In the worst case, trial 1 shows that overshoot can cause the vehicle to veer off the path towards the end, resulting in a constant nontrivial error. In the best case scenario, at high speed, trial 6 shows good response throughout the course. The lowest value of the maximum error is shown for trial number 4, when the speed is low, at 8 km/h. Taking in account of all 6 trials, it can be claimed that the gain and look-ahead distance should be made into a variable that changes depending on the speed. Since, we only used proportional gain for this experiment and speed was set to the desired value by a human driver, there is some inconsistency in our trials, as can be observed through trial number 3 and trial number 4.

CONCLUSION

This report detailed the usage of LiDAR as the sole sensor for the application of path tracking. We were able to see that, with good enough control parameters, it is possible to have a tracking error of less than 1 meter throughout a simple circular course. However, increase in speed can significantly affect the response of the vehicle.

LiDAR has shown itself to be serviceable for following a path accurately if the parameters of the control algorithm is adjusted correctly. The current approach, using an *a priori* constructed map to obtain localization data, shows promise for future use in more complicated paths and environment. But, towards even higher speeds than 12 km/h, it will be desirable to have a LiDAR with a higher refresh rate than 10 Hz so the controller can make faster adjustments.

For future work, more path tracking data should be accrued with the LiDAR. Moreover, a dynamic simulation of the path tracking algorithm should be obtained to better understand the effects of the PID gains. Combining both of these data, a complete PID control and a variable look-ahead distance should be developed so that the path tracking will be optimized for low tracking error, low overshoot, and high response time. Since this experiment only used a simple circular path with high radius of curvature, the path tracking algorithm should be tested to see how it responds to sudden changes in the path. Then, the usage of LiDAR for path tracking can be compared with the usage of other sensors doing similar types of path tracking.

REFERENCES

- [1] Coulter, R.C., Implementation of the Pure Pursuit Tracking Algorithm, report within CMU-RI-TR-92-01 (1992).
- [2] Snider, J.M., Autonomous Steering Methods for Autonomous Path Tracking, report within CMU-RI-TR-09-08 (2009).
- [3] Lundgren, M., Path Tracking of Miniature Robot, Master's Thesis, Dept. of Computer Science, Umea University (2009).
- [4] Giesbrecht, J., Mackay, D., Collier, J., Verret, S., Path Tracking for Unmanned Ground Vehicle Navigation, Defense Research and Development Canada (2005).
- [5] Hoffman, G.M., Tomlin, C.J., Montemerlo, M., Thrun, S., Autonomous Automobile Trajectory Tracking for Off-Road Driving: Controller Design, Experimental Validation and Racing, Proc. 26th Amer. Control Conf., pp. 2296-2301 (2007).
- [6] Wolcott, R.W., Eustice, R.M., Visual Localization within LIDAR Maps for Automated Urban Driving, Intelligent Robots and Systems (IROS 2014), 2014 IEEE/RSJ International Conference on, pp. 176-183 (2014).
- [7] Biber, P., The Normal Distributions Transform: A New Approach to Laser Scan Matching, *IEEE/RSJ International Conference on*, 2003, pp. 2743-2748 vol.3 (2003).
- [8] Morales, J., Martinez, J.L., Martinez, M.A., Mandow, A., Pure-Pursuit Reactive Path Tracking for Nonholonomic Mobile Robots with a 2D Laser Scanner, *EURASIP Journal on Advances in Signal Processing*, Volume 10 (2008).

CARBON NANOTUBE THIN FILM TRANSISTORS ON FLEXIBLE PLASTIC FILMS

Matthew Yee

Department of Materials Science and Engineering, Graduate School of UCLA
mayee@ucla.edu

Supervisor: Prof. Yutaka Ohno

Graduate School of Engineering, Nagoya University
yohno@nuee.nagoya-u.ac.jp

ABSTRACT

Carbon nanotube thin film transistors (CNT-TFTs) exhibit p-type behaviour under atmospheric conditions. These electrical characteristics can be controlled by chemical doping of the nanotubes. N-type and p-type doping of CNT-TFTs on PEN substrates have been demonstrated using PEI and F₄-TCNQ respectively. F₄-TCNQ doped devices were passivated with CP 1010 and display stable p-type characteristics with low hysteresis. PEI doped devices exhibit n-type behaviour with large hysteresis.

1. INTRODUCTION

Recently, there has been an increasing interest in flexible electronic devices and screens. Thin Film Transistors (TFTs) are a key component in LCDs but are currently based on amorphous or polysilicon substrates which offer only limited flexibility. It is desirable for such devices to be fabricated on plastic substrates, allowing for additional flexibility. Carbon nanotube (CNT)-TFTs on plastic substrates have previously been demonstrated using networks of randomly oriented CNTs and are promising for flexible devices.¹

CNTs are an extremely attractive material for TFTs due to their high carrier mobility, mechanical flexibility, and compatibility with solution based processing.² Both n-type and p-type devices are necessary for many integrated circuit technologies, including CMOS. The electrical properties of these devices for any application must be precisely controlled for consistent and high performance operation. This can be done by selecting contact materials with varying work functions³ or by doping the CNTs.³ In this project, CNT-TFTs were fabricated and doped using Tetrafluoro-tetracyanoquinodimethane (F₄-TCNQ) as a p-type dopant and Polyethylenimine (PEI) as an n-type dopant. F₄-TCNQ and PEI are commonly used as dopants for polymers^{4,5}, and have also previously been used for CNT doping.^{6,7}

Surface passivation of devices is also extremely important to preserve the electrical characteristics of devices when they are exposed to the ambient environment. As

fabricated CNT-TFTs exposed to the ambient atmosphere possess unipolar p-type characteristics. Furthermore, CNT-TFTs exposed to atmospheric levels of O₂ and H₂O exhibit current collapse and large hysteresis.⁶ However, annealing the devices will remove any adsorbed atmospheric gases, reducing hysteresis and current collapse as well as change the electrical characteristics to ambipolar.⁸

N-type devices on PEN substrates using a filter based transfer technique with low hysteresis and controlled electrical properties have previously been achieved by this group through PEI doping and an Al₂O₃ passivation layer. In this project, similar experiments were carried out to examine F₄-TCNQ as a p-type dopant to obtain p-type devices with low hysteresis as well as controllable electrical characteristics. CP1010 was also investigated as a possible passivating layer

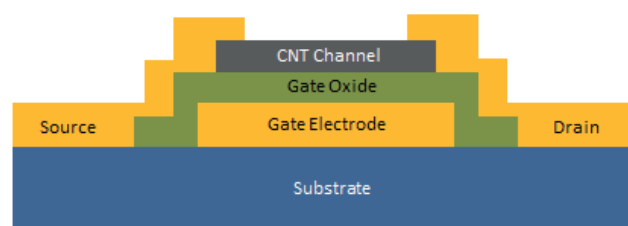


Figure 1. Schematic of cross section of bottom-gate CNT-TFT.

2. EXPERIMENTAL

Bottom-gate CNT-TFTs were fabricated with the device structure as shown in Figure 1 with a channel length of 100 μm . Devices were fabricated on polyethylene naphthalate (PEN) substrates prepared by sonication in acetone for 5 minutes, washing with IPA, and annealing at 200 $^{\circ}\text{C}$ for 2 hours and 30 minutes. All features were defined using standard contact photolithography and lift-off techniques. The source, drain, and gate electrodes were deposited (Ti/Au 10/100 nm) using electron-beam evaporation. A 40 nm Al₂O₃ gate oxide was deposited using atomic layer deposition

(ALD) at 145 °C. The gate electrode was deposited first, followed by the deposition of the gate oxide, CNT network transfer, and source and drain deposition.

CNTs with an average diameter of 1.3 nm and an average length of 0.1 μm were suspended in a 1% Sodium Cholate, 0.3% Sodium Dodecyl Sulfate aqueous solution and dispersed by sonication and subsequently vacuum filtered using Millipore membrane filters. Remaining surfactants were washed away using 100 mL of H_2O at 45 °C. Substrates were functionalized by Oxygen plasma ashing at 100 W, 180 sccm for 3 minutes and (3-Aminopropyl)triethoxysilane (APTES) vapor by evaporating 2 μL of 1 wt% APTES at 120 °C and exposing for 2 hours in a sealed environment.

CNT transfer was performed by wetting the filter with Butanol and contacting the filter to the substrate. The filter was dissolved using Acetone and Remover(1165). Each device was electrically isolated using Oxygen plasma ashing at 200 W, 180 sccm for 3 minutes.

Tetrafluoro-tetracyanoquinodimethane ($\text{F}_4\text{-TCNQ}$) dissolved in Toluene with concentrations of 0.001, 0.01, and 0.1 mM. Polyethylenimine (PEI) was dissolved in solutions of Methanol with concentrations of 0.5 wt% and 0.005 wt% were spincoated on devices at 3000 rpm for 50 s. $\text{F}_4\text{-TCNQ}$ doped samples were passivated with 40 nm Al_2O_3 , CP 1010, and CP 1010 followed by followed by 40 nm Al_2O_3 . Substrates were prebaked at 130 °C for 10 minutes before doping and the dopant solvent was evaporated by baking at 60 °C for 5 minutes. CP 1010 was cured by baking at 150 °C for 2 minutes and exposing to UV for 30 seconds.

3. RESULTS AND DISCUSSION

3.1 Undoped Devices

Devices were examined using SEM, but the CNTs were unable to be resolved. However, a successful transfer was confirmed by the electrical characteristics of the devices

Figure 2a) shows the $I_d\text{-}V_{gs}$ at $V_{ds} = 500$ mV of undoped devices exposed to air. P-type characteristics are exhibited which is consistent with literature results⁸ as well as previous experimentation. Additionally, there is a hysteresis of about 1 V present in these devices as would be expected due to the presence of oxygen and water. However, these devices differ from previous experiments slightly in their on-off ratios. Previous experiments produced devices with on-off ratios of $10^4\text{-}10^5$, compared to these devices which had on-off ratios of $\sim 10^3$.

3.2 $\text{F}_4\text{-TCNQ}$ Doping

The electrical characteristics after passivation by Al_2O_3 for devices doped with 0.001, 0.01, 0.1 mM $\text{F}_4\text{-TCNQ}$ as well as an undoped sample for reference are shown in Figure 2b). However, all devices showed ambipolar conduction regardless of doping concentration instead of strong p-type conduction as would be expected from p-type doped

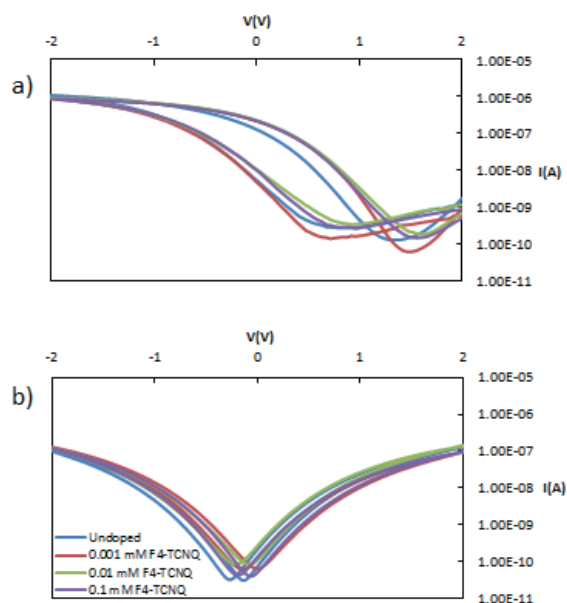


Figure 2. $I_d\text{-}V_{gs}$ characteristics at $V_{ds} = 500$ mV for a) undoped devices, b) $\text{F}_4\text{-TCNQ}$ doped devices passivated with 40 nm Al_2O_3 using ALD

devices. $\text{F}_4\text{-TCNQ}$ has been reported to be volatile and possesses a high vapor pressure which can lead to evaporation during vacuum processes.⁹ It is likely that the $\text{F}_4\text{-TCNQ}$ was evaporated along with the adsorbed atmospheric gases during ALD before the surface could be fully passivated due to the elevated temperature (145 °C) and vacuum environment.

CP1010 was used as an intermediate layer between the dopants and the Al_2O_3 to prevent the $\text{F}_4\text{-TCNQ}$ from evaporating before the surface was fully passivated. The doping effect of $\text{F}_4\text{-TCNQ}$ before the depositions of CP1010 and ALD was verified as shown in Figure 3a) using 0.1 mM $\text{F}_4\text{-TCNQ}$. The electrical characteristics of the doped devices displayed increased p-type conduction compared to non-doped samples as shown in Figure 3a). Both the on and off currents of these devices were increased. However, when subjected to ALD, the characteristics of the devices became ambipolar, similar to Figure 2b), indicating that the $\text{F}_4\text{-TCNQ}$ was still able to evaporate even with the CP1010 layer. Devices spincoated with CP1010 without Al_2O_3 had on and off currents with values similar to those of the pre-doped state as shown in Figure 3b). This is likely due to the dopants being mixed into the polymer during spincoating, decreasing the amount of dopants adsorbed on to the CNTs. Devices doped by $\text{F}_4\text{-TCNQ}$ and passivated with CP1010 have hysteresis of ~ 0.5 V compared to non-passivated devices which have a hysteresis of ~ 1 V. Additionally, devices passivated with CP 1010 maintained stable electrical characteristics for 5 days.

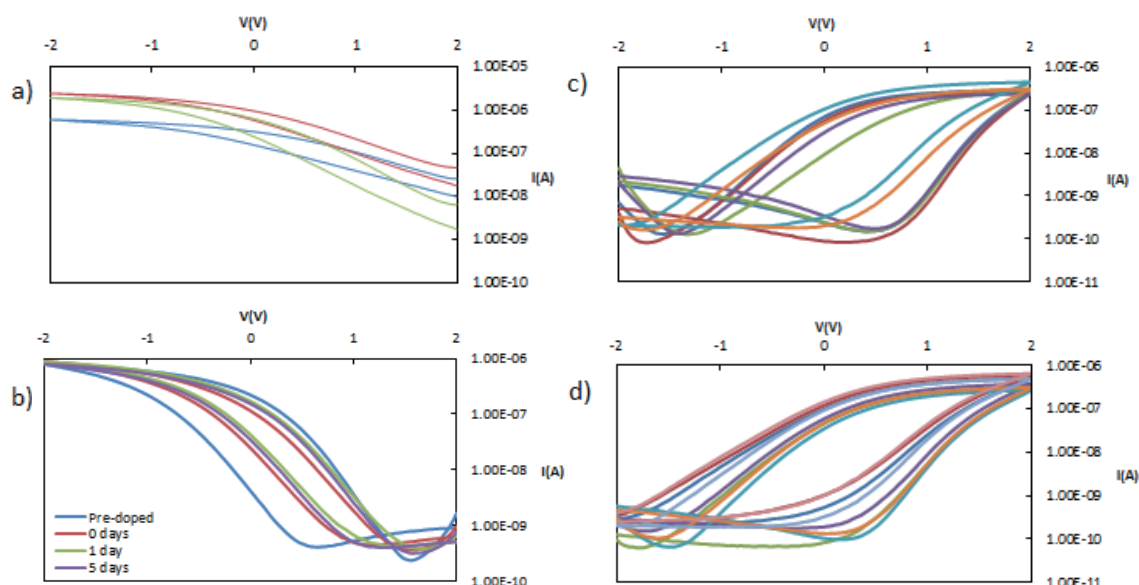


Figure 3. I_d - V_{gs} characteristics at $V_{ds} = 500$ mV for a) devices doped with 0.1 mM F_4 -TCNQ without passivation, b) devices doped with 0.1 mM F_4 -TCNQ and passivated with CP1010 0, 1, and 5 days after doping, c) 0.5 wt% PEI doped devices and CP 1010 passivated, and d) 0.5 wt% PEI doped devices and CP 1010 passivated after annealing for 1 hr at 145 °C in vacuum.

3.3 PEI Doping

Devices were doped with PEI 0.5 wt% PEI solutions and spin coated with CP1010 to determine if the same method could be used to create passivated n-type devices with low hysteresis without the use of ALD. However, using the same spincoating parameters (3000 rpm for 50 s) produced non-uniform layers as shown in Figure 4. The electrical characteristics are displayed in Figure 3c) and although the PEI doped devices displayed n-type behavior, they also possessed a hysteresis of ~ 2 V. It is unclear what the cause of these non-uniformities is as well as the increase in hysteresis. It is possible that the Methanol only partially evaporated and disrupted the CP 1010, or it could also be due to an interaction between the PEI and CP 1010.

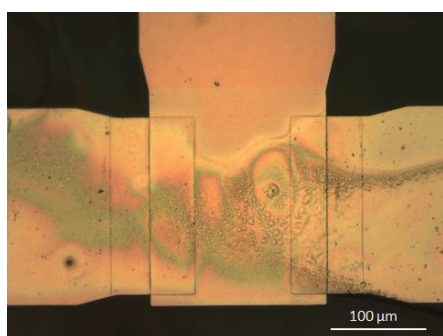


Figure 4. Optical microscope image of 0.5 wt% PEI doped devices with CP 1010.

Devices doped with 0.5 wt% PEI with CP 1010 spincoated were annealed at 145 °C in vacuum to evaporate any adsorbed atmospheric gases through the CP 1010. The devices not annealed in vacuum showed slight p-type characteristics at negative gate voltages which were reduced

after annealing in vacuum as shown in Figure 3d). However, the hysteresis is still present, indicating that the hysteresis is due to an interaction with the CP 1010.

4. CONCLUSIONS

In summary, bottom gate CNT-TFTs have been doped with F_4 -TCNQ and PEI. F_4 -TCNQ was found to evaporate when subjected to ALD. Passivation of devices using CP 1010 was investigated and produced devices with hysteresis of ~ 5 V air stability of at least 5 days. PEI doped devices passivated with CP 1010 exhibited non-uniform layers with large hysteresis of ~ 2 V. Further research is necessary to determine the stability of CP1010 passivated devices over long periods of time. Additionally, applications such as CMOS will require optimization of F_4 -TCNQ dopant concentrations as well as find methods that are compatible for fabrication of both n-type and p-type devices. Possible avenues of research may include utilizing less volatile p-type dopants that are compatible with ALD or finding an alternative polymer that would allow passivation of both PEI and F_4 -TCNQ doped devices.

ACKNOWLEDGEMENTS

Thank you to Benny Tan for his guidance and help throughout this project.

REFERENCES

- [1] Sun, D., Timmermans, M., Tian, Y., Nasibulin, A., Kauppinen, E., Kishimoto, S., Mizutani, T., Ohno, Y., Flexible high-performance carbon nanotube integrated circuits, *Nat. Nanotechnol.*, 6, pp. 156–161 (2011)

- [2] Wang, C.; Zhang, J.; Ryu, K.; Badmaev, A.; De Arco, L. G.; Zhou, C. Wafer-Scale Fabrication of Separated Carbon Nanotube Thin-Film Transistors for Display Applications. *Nano Lett.*, 9, pp. 4285–4291 (2009)
- [3] Alam, K., Lake, R., Role of Doping in Carbon Nanotube Transistors With Source/Drain Underlaps. *IEEE Trans. Nanotechnol.*, vol. 6, no. 6, pp. 652–658 (2007)
- [4] Guillain, F., Endres, J., Bourgeois, L., Kahn, A., Vignau, L., Wantz, G., Solution-Processed p-Dopant as Interlayer in Polymer Solar Cells. *ACS Appl. Mater. Interfaces*, 8, pp. 9262–9267 (2016)
- [5] Sun, B., Hong W., Thibau, E., Aziz, H., Lu, Z., Li, Y., Polyethylenimine (PEI) As an Effective Dopant To Conveniently Convert Ambipolar and p-Type Polymers into Unipolar n-Type Polymers, *ACS Appl. Mater. Interfaces*, 7(33) pp. 18662-18671 (2015)
- [6] Noshu, Y., Ohno, Y., Kishimoto, S., Mizutani, T., The effects of chemical doping with F₄TCNQ in carbon nanotube field-effect transistors studied by the transmission-line-model technique, *Nanotechnology*, **18** 415202 (2007)
- [7] Yasunishi, T., Kishimoto, S., Ohno, Y., Effect of ambient air on n-type carbon nanotube thin-film transistors chemically doped with poly(ethylene imine) *Jpn. J. Apply. Phys.* Vol 53, No. 5S1, (2014)
- [8] Martel, R., Derycke, V., Lavoie, C., Appenzeller, J., Chan, K., Tersoff, J., Avouris, P., Ambipolar Electrical Transport in Semiconducting Single-Wall Carbon Nanotubes, *Phys. Rev. Lett.*, Vol 87, No. 25 (2001)
- [9] Mi, B., Gao, Z., Cheah, K., Chen, C., Organic light-emitting diodes using 3,6-difluoro-2,5,7,7,8,8-hexafluoroquinodimethane as p-type dopant, *Appl. Phys. Lett.* **94**, 073507 (2009)

ESTIMATION OF THE REGION OF ATTRACTION FOR OPTIMIZATION OF DESIGN PARAMETERS IN NONLINEAR CONTROL SYSTEMS

Bonan Zhou

Department of Mechanical and Aerospace Engineering, Graduate School of UCLA
bonanzhou@ucla.edu

Supervisor: Dr. Susumu Hara

Graduate School of Engineering, Nagoya University
haras@nuae.nagoya-u.ac.jp

1. ABSTRACT

A novel method for efficiently determining optimal control design parameters was developed for the 6-link inverted pendulum. This method can be extended to general nonlinear dynamic systems. This method combines a genetic algorithm (GA) with a Monte Carlo Bisection Search (MCBS) to select an optimal combination of parameters with respect to enlarging the Region of Attraction (ROA) of a nonlinear system stabilized by a Linear Quadratic Gaussian (LQG) controller. Furthermore, substituting the Monte Carlo optimization of the ROA with a linear matrix inequality (LMI) method based around minimizing the peak response of the system yielded similar results. Thus, it may be possible to realize an even faster yet accurate version of this algorithm by substituting direct estimation of the ROA with an LMI approach.

2. LANGUAGE AND UNITS

2.1 ALGORITHM TERMS AND VARIABLES

GA: Genetic algorithm

MCBS: Monte Carlo Bisection Search

ROA: Region of Attraction

R : Radius of ROA

M : Number of stability tests in MCBS

H : Number of bisection iterations in MCBS

N : Population size in GA

L : Number of generations in GA

2.2 DYNAMIC SYSTEM PARAMETERS

r_i : length of i-th link [m]

m_i : mass of i-th link [kg]

ρ : density of each link [g/cm^3]

μ_i : friction in i-th joint [Nms]

- τ_i : torque in i-th joint [Nm]
 t_i : distance to tip of i-th link [m]
 p_i : distance to center of mass of i-th link [m]
 v_i : velocity of center of mass in i-th joint [m/s]
 q_i : angle of i-th joint from local vertical [rad]
 ω_i : angular velocity of i-th joint [rad/s]
 J_i : inertial moment of i-th link [$kg\ m^2$]
 T : kinetic energy of system [$kg\ m^2/s^2$]
 U : potential energy of system [$kg\ m^2/s^2$]
 L : Lagrangian of system [$kg\ m^2/s^2$]

2.3 STATE-SPACE VARIABLES AND MATRICES

LQG: Linear Quadratic Gaussian

LMI: Linear Matrix Inequality

x : state vector

u : scalar input

$f(x)$: nonlinear function of state vector

$g(u)$: nonlinear function of input

A : linearized dynamic matrix

B : linearized input matrix

C : measurement matrix

K : controller gain

3.1 OPTIMIZATION ALGORITHMS

The main optimization problem we considered for the 6-link inverted pendulum is this:

$\max R$

w.r.t. $r_0 \dots r_5$

Where R is the radius of the largest hyper-sphere contained in the ROA and centered on the origin, and $r_0 \dots r_5$ are the link lengths of the each link of the pendulum. There is considerable research on direct calculation or estimation of the ROA based on sum-of-squares methods or rational Lyapunov functions [1],[2],[3]. However elegant, these methods are known to be very conservative. This research attempts to reduce this conservativeness by directly optimizing the ROA with respect to system design parameters using simple probabilistic approximation schemes.

Our optimization procedure can be pictured in two layers. First, there is the lowest layer optimization problem of evaluating an individual cost function for a given set of design variables. One must estimate the size of the ROA with the largest hyper-sphere (sphere henceforth) that can fit inside the *a priori* unknown ROA (which is arbitrary, but usually some oblong shape). Estimating this “largest interior sphere” is thus an optimization problem that must be solved many times for a particular combination of system design parameters (such as link lengths in an inverted pendulum). Second, there is the optimization problem of evaluating an ensemble of these cost functions for the space of design parameters that one seeks to optimize over. Monte Carlo Bisection Search (MCBS) was used for the former. A genetic algorithm (GA) was used for the latter.

Additionally, a much faster LMI method based on minimizing the peak response was tested instead of the MCBS approach. While the LMI method does not directly deal with the ROA, it resulted in optimal design parameters that were extremely similar to the MCBS method, indicating that it may be a valuable design metric in lieu of ROA estimation when approaching nonlinear control systems.

For a comparison of the run-times of these algorithms, see Table 1. For a comparison of the optimal link lengths yielded by these algorithms see Table 6. For a plot of the cost functions and link lengths of these algorithms see Tables 3A, 3B, and 3C.

3.1.1 MONTE CARLO BISECTION SEARCH (MCBS)

The ROA is the set of initial conditions (positions and velocities) for which the closed-loop nonlinear system will be stable. Naturally, the ROA lies in a $2N$ dimensional space where N is the number of degrees of freedom of the system, and as usual, stability is defined as all states of the system (positions and velocities) decaying to zero, the origin of this space. Thus, for the simulations that will be discussed in this paper, the ROA can be pictured as a $2N$ dimensional unknown subspace around the origin. One is generally interested in enlarging this subspace. However, from a design perspective, simply making it larger without regard to its shape is not necessarily good. For instance, an extremely elliptical ROA would not yield a control system with desirable performance characteristics as it would imply that while very specific configurations of position and velocity would be stable, nearby configurations that happen to be outside of the ellipse would be unstable. Therefore, from a design perspective one is interested in enlarging the approximately spherical region of the ROA in $2N$ dimensions.

Thus, the problem of estimating the ROA becomes one of placing the largest sphere possible inside of the true ROA. It is of course fine if the ROA does in fact have “lobes,” or additional stable regions extraneous to the spherical part. But, the main interest is in finding design parameters (link lengths in this research) for which the quasi-spherical region around the origin is largest.

This is a non-trivial problem, however, because the ROA is not *a priori* known; each point in the ROA represents an initial condition for which a stability test of the nonlinear system must be performed. For a nonlinear system, this test cannot be done without actually simulating the system through numerical integration. As doing this is extremely time consuming, it becomes critical to test the fewest number of points in the ROA possible to determine the largest interior sphere.

A combination of bisection search and Monte Carlo methods were used to perform this test efficiently. This Monte Carlo Bisection Search (MCBS) begins by choosing a large sphere that will generally be much larger than the ROA. This is the “ceiling” that one tries to systematically lower to locate the radius of the largest interior sphere. One randomly picks a point on this ceiling and tests the stability of the closed-loop nonlinear system for that initial condition. As this ceiling will almost always be too large, the chances are high that one selects an unstable initial condition. If not, one randomly picks another point on the sphere until an unstable initial condition is found or some user-defined maximum number of points is reached. How one precisely picks this maximum is somewhat arbitrary, but it dictates the confidence level one has in the final answer (see Section 3.2.3 for details).

Once a single unstable point has been found, one can safely reject the candidate sphere as being the largest interior sphere because, by definition, that sphere's surface (and all the points it encloses) should be composed entirely of stable initial conditions (as this is the definition of being part of the ROA). When a candidate sphere is rejected, the next candidate proposed is a sphere with half the radius of the previous candidate. Then, one repeats the process of randomly selecting initial conditions. If the candidate is again rejected, the next candidate's radius is halved. However, if a suitable number of initial conditions tested are all stable, it is known to a certain confidence level that the sphere most likely lies within the ROA (see 3.2.3 for details). At this point, one has obtained a stable interior sphere, but it is not known if this is the *largest* interior sphere. Hence, the next candidate will be a sphere whose radius is halfway between the previous candidate which is known to be safe, and the candidate before that which is known to be unsafe. This is no different from bisection search.

This MCBS technique can quickly determine the largest interior sphere of the ROA. The MCBS is summarized below:

1. For iteration i , randomly test points on the surface of candidate sphere of radius $r[i]$ until an unstable one is found.
2. If an unstable point is found, define a new candidate sphere of radius is $r[i]/2$.
3. If no unstable point is found after M tests, define a new candidate sphere whose radius is $\frac{1}{2}(r[i] + r[i-1])$.
4. Go to 1 until this loop has run H times.

Here M and H will affect the confidence level and precision in the final answer, respectively. In the abstract, it is desirable to make M and H as large as possible. But as the runtime of the algorithm is of order $M \cdot H$, there is a trade-off between these two considerations. Nevertheless, it is important to note that the run-time does not directly depend on the dimension of the search space, and only on the tuning parameters M and H (see Table 2 for details).

3.1.2 GENETIC ALGORITHM (GA)

The previously discussed MCBS algorithm is used to estimate the ROA for a particular set of design parameters - for instance, some combination of link lengths in the 6-link inverted pendulum.

However, there is the second problem of then how to efficiently optimize the link lengths with respect to the MCBS measure, subject to length constraints (minimum and maximum link lengths as well as a total length constraint for the entire mechanism). This optimization was done using a genetic algorithm.

A random population of mechanisms was generated by drawing link lengths from a uniform distribution subject to the constraint that the total length not exceed 1.5 meters and that each link be greater than .1 meter and less than 1 meter. Then, each member of this population was evaluated according to MCBS. The members with the largest ROA estimates were then “bred” pairwise by rank, wherein the top two members were bred, then the next two, and so forth. Breeding consisted of randomly selecting a link from one of the parents to be passed on the child.

At this point, the children are merely a direct hybrid of their parents so mutation was introduced to ensure better exploration of the search space. The mutation was generated as a normally distributed random variable, with zero mean. The variance controls the magnitude of the mutation, and is a tuning parameter in this algorithm. Furthermore, these mutations again must accord with the total and individual link length constraints. Thus, once the mutations were generated in the algorithm, they were adjusted so that no individual link would mutate above or below the minimum and maximum link lengths and also that the total mechanism length would not exceed the maximum (see Table 3 for details).

Finally, as half the population is culled, and each pair of survivors has four children, the population is always constant. The next generation then begins, where the children are again tested, culled, and bred.

The GA is summarized below:

1. Test entire population of N members according to MCBS (or LMI, see 3.1.3).
2. Sort population by fitness and kill bottom half.
3. Survivors breed pairwise, and pass on traits to children randomly with mutation.
4. Children become new population. Go to 1 until this loop has run L times.

Here N and L affect the accuracy of the final answer, but it is difficult to estimate the actual accuracy. This is why GA is considered a heuristic approach. Like MCBS, the runtime does not depend on the dimension of the search space and scales as N*L (see Table 3 for details).

3.1.3 PEAK RESPONSE USING LMI

Though MCBS is much faster than a deterministic bisection search (which would require many grid points in a high dimensional space), an even faster approach is to substitute direct enlargement of the spherical portion of the ROA with an LMI peak response minimization (Table 1). In other words, instead of directly maximizing R , one minimizes the peak deviation of the system from equilibrium, as it is known that the underlying linearization needed to design the controller becomes a poor approximation as the system disequilibrates. This is discussed in greater detail in Section 3.2.5.

The purpose of this proxy method is that if a problem can be phrased as an LMI then it can be readily solved by efficient algorithms on a computer. Thus, by replacing the MCBS evaluation of the ROA with a the LMI, the genetic algorithm was able to find the optimal link lengths in a matter of minutes. In testing, it was shown that using this LMI as the cost function (over which the GA optimized), yielded similar link lengths to the MCBS cost function with a much quicker run-time. See Fig. 3A and 3C for the optimal link lengths and Table 1 for a comparison of the run-times.

3.2 EQUATIONS

3.2.1 LINEARIZED DYNAMICS

The 6-link inverted pendulum is 6 consecutive revolute joints connected by rigid links with a revolute actuator at the base and encoders in each of the 6 joints to measure the joint angles. The positions of the midpoints, p_i , of each link can be expressed with the following equations:

$$t_0 = [r_0 \cos q_0, r_0 \sin q_0]^T$$

$$p_i = t_{i-1} + .5t_i$$

$$t_{i+1} = t_i + [r_i \sin q_i, r_i \cos q_i]^T$$

Where $0 \leq i \leq 5$ and enumerates each link, link 0 representing the base with the actuator t_i representing the distance to the tip of the mechanism and p_i locates the midpoint of each link. Note that $t_i = 0$ for $i < 0$. Then, the kinetic and potential energy of the system, K and U ,

can be expressed in terms of the velocity, angular velocity, inertial moments of each link, v_i, ω_i, J_i :

$$v_i = dp_i / dt$$

$$\omega_i = dq_i / dt$$

$$J_i = 1/12 m_i r_i^2$$

$$T = \sum 1/2 m_i v_i^2 + 1/2 J_i \omega_i^2$$

$$U = \sum m_i g p_i e_2$$

Where the mass was given by $m_i = 2\pi l \rho$ and ρ is the density of aluminum 2.7 g/cm^3 .

Then, by defining an energy quantity known as the Lagrangian, L , the equations of motion can be determined from taking derivatives of L with respect to the degrees of freedom of the system, q_i , and the time derivatives of those degrees of freedom, ω_i :

$$L = T - U$$

$$d/dt \partial L / \partial \omega_i - \partial L / \partial q_i = F_i$$

Where the input torque on joint 0 is:

$$\tau_0 = u - \mu_0 \omega_0$$

And the torque on joints $1 \leq i \leq 5$ are:

$$\tau_i = -\mu_i \omega_i$$

For values of the link density, friction, and other dynamic system parameters see Table 5.

Solving for the Lagrangian equations of motion would be too tedious to do by hand, so they were done via a symbolic solver (MuPad). The resulting dynamic equations are profoundly nonlinear, too lengthy to reproduce here, and too impenetrable to be understood analytically.

Thus, let us simply represent the resulting Lagrangian equations of motion in terms of f and g which are arbitrary nonlinear function of the state vector, x :

$$dx/dt = f(x) + g(u)$$

Where the states in x are the joint angles and angular velocities:

$$x = [q_0 \dots q_5, \omega_0 \dots \omega_5]^T$$

These equations are then linearized to yield the traditional linear system state space:

$$dx/dt = Ax + Bu$$

With measurement:

$$y = Cx$$

Where $A = \partial f / \partial x$ is evaluated around equilibrium $x = 0$ and $B = g(0)$. This equation represents the approximate first order dynamics when the 6-link inverted pendulum is in or near a completely vertical “headstand.” From these assumptions, the LQG controller and filter was implemented resulting in the standard Kalman filter and familiar linear feedback law:

$$u = K x_e$$

Where x_e is the state estimate from the Kalman filter. Note that it is assumed that the angle of each joint is measured independently by encoder, and that these encoders have unity gain.

3.2.3 MCBS ACCURACY

As mentioned, the accuracy of the MCBS algorithm is dictated by M , the number of stability tests one makes before deciding an interior sphere lies inside the true ROA, and K , the number of bisection search iterations, which affects the precision with which one knows the largest interior sphere.

Let us characterize the fraction of the area on the candidate sphere that lies in the ROA as α . Again, as the ROA is not *a priori* known, the exact value of α is unknown. However, by definition it satisfies $0 < \alpha < 1$. This is important because if one randomly selects points from the surface of the candidate sphere, the chance of randomly selecting a point that also lies in the true ROA is exactly equal to α . This of course implies that the probability, P , of randomly selecting M points that happen to lie in the ROA is $P = \alpha^M$.

Consequently, at the last iteration of the algorithm, one can be sure that the probability of a “false negative” or that the candidate sphere does in fact lie outside of the ROA is equal to α^M . As M , the number of point selections was chosen to be 50 in this research, for reasonable values of α (for example, .95), there is only about an 8% chance that all of the initial condition points randomly selected would lie in the true ROA. Indeed, this would lead to incorrectly accepting that candidate sphere as the largest interior sphere; however, by construction this sphere would have .95 of its surface area inside of the true ROA. As this method is just an approximation scheme, we consider this error to be acceptable.

Moreover, the precision of the MCBS algorithm is dictated by the iteration number, K because each bisection cuts the search space by half. Thus, the ultimate precision, D is given by $D = 2^{-K}$.

Importantly, this methods scales extremely well with the dimension of the phase space (see Table 1 for run-times for 2-link vs. 6-link mechanism). Additionally, the early iterations of the bisection search will reject the candidate sphere very quickly, as when the sphere is large, the number of stability tests one needs to perform is small; indeed most of the initial conditions that lie on the surface of a large candidate sphere will be outside the true ROA. Note that the MCBS algorithm was parallelized for a quad-core processor.

3.2.4 GA ACCURACY

Genetic algorithms are merely heuristic so it is difficult to make statements about their accuracy. Nevertheless, in our tests, the agreement between the genetic algorithm and more exhaustive methods such as the built-in nonlinear optimizers in MATLAB (tested on a random ensemble of initial conditions) was extremely close. The results combination of the GA with the MCBS cost function are in Table 3A. As the cost function to the GA in this approach is the radius of the ROA, that increases with each iteration as the algorithm seeks to “evolve” the fittest mechanism according to MCBS.

Furthermore, agreement with grid search methods on a lower dimensional test system was also good. Specifically, the genetic algorithm approach was checked against a grid search of the optimal link lengths in the Acrobot mechanism. This could be done in a reasonable amount of time because the search space is only two-dimensional (each length axis was partitioned into 20 points, yielding a total of 400 grid points). Based off this agreement, the GA was used to optimize over the 6-dimensional space of the 6-link inverted pendulum (see Fig. 2A and 2B).

3.2.5 PEAK RESPONSE AND LMI EQUATIONS

Minimizing the peak response of the system can be related to the minimization of the condition number of a Lyapunov inequality. This in turn can be expressed as an LMI minimization problem which can be solved very quickly. Using the fact that the system uses a linear feedback law $u = Kx$, the closed-loop dynamics are given by:

$$dx/dt = (A + BK)x$$

Here we have ignored the fact that the controller does not actually have full-state feedback, but instead the state estimate x_e from some state observer. Normally, this is fine because a linear system obeys the separation principle, which dictates that the controller and filter can be designed separately, where the controller has access to the full-state. As this system is nonlinear, that is no longer true.

However, as we are not relinearizing the dynamics anyway (as doing so at each time step would be too time consuming), we are essentially forced to assume that the system will usually operate close to its equilibrium point (the point about which A and B were generated) no matter what. Under these assumptions, the system is close to linear, so we will treat the feedback as full-state for the purpose of the LMI analysis.

Then, defining the closed-loop dynamics as $A_{cl} = A + BK$, one can minimize the peak response of the system, which is tantamount to minimizing the condition number of the corresponding Lyapunov solution of the stable closed-loop system [4], [5]:

$$\min \kappa(P)$$

Where $\kappa(P) = \lambda_{\max}(P) / \lambda_{\min}(P)$, while simultaneously enforcing the following Lyapunov inequality on P :

$$P A_{cl} + A_{cl}^T P + 2\beta P < 0$$

This can then be converted into an LMI problem:

$$\min \gamma$$

Subject to:

$$\begin{aligned} A_{cl} Y + Y A_{cl}^T - B Z - Z^T B^T &< 0 \\ I &< P' < \gamma I \end{aligned}$$

Where:

$$\begin{aligned} Z &= K P^{-1} \\ Y &= P'^{-1} \\ P &= \beta P' \end{aligned}$$

This LMI cost function yielded optimal link lengths extremely close to that of the MCBS cost function, which was much more exhaustive and time-consuming (see Table 1 for run-times and Table 6 for optimal link lengths). This indicates that replacing the MCBS evaluation of the ROA with the LMI peak minimization does not yield a significantly different answer. The combination of GA with the LMI cost function seeks to minimize the peak response; this can be seen from Fig. 3B, where the cost decreases after each generation. The final optimal link lengths can be seen in Fig. 3C (compare with Fig. 3A).

The fact that this LMI cost is so similar to the MCBS cost (despite being much more *ad hoc*) agrees with our intuition that the stability properties of a nonlinear system with a linear controller should be better when the system operates very near its linearization point - in this case equilibrium. Thus, peak minimization may be a good proxy for directly calculation of the ROA when searching for optimal design parameters.

3.2.6 LQG CONTROLLER AND DISTURBANCES

Using the optimal link lengths given by the GA and MCBS cost function (see Fig. 3A) the LQG command from MATLAB was used to design the controller for the 6-link inverted pendulum. The LQG framework accounts for both process noise and measurement noise. In this 6-link inverted pendulum problem, the actuator in joint 0 had process noise, w , and all 6 encoders had measurement noise, v . The corresponding state-space dynamics of this noise corrupted system is:

$$dx/dt = Ax + B(u + w)$$

With measurement:

$$y = Cx + v$$

However, this model is still highly idealized and ignores several practical limitations, such as the resolution of the encoders used to actually measure the joint angles, and the deadband as a result of mechanical backlash in the motor. These effects were added in Simulink (see Fig. 1 for block diagram and Table 5 for numerical values) but were not modelled in the LQG or LMI designs.

Nevertheless, the LQG controller with the optimal link lengths was able to stabilize the inverted pendulum for certain values of backlash and deadband (as much as .025 degrees, .055 degrees). In simulation (performed in Simulink) it was found that while the LQG controller was robust against noise, as this is inherently part of the LQG framework, the backlash and deadband had a significant effect on the robustness of the controller (see Fig. 4B).

Indeed, to stabilize the system, the process noise covariance W and the measurement noise covariance V had to be artificially widened. It is common practice to “lie” to the filter/controller to account for unmodeled disturbances by artificially widening the anticipated power on these noise signals (see Table 4B).

In Fig. 4A, the backlash was reduced to .0025 and .0055 degrees and the system performance is visibly significantly improved, in terms of steady state and peak response. For this LQG controller the true values of the noise power were used (see Table 4A).

Finally, it must be noted that the purpose of the simulation was simply to verify that the link lengths generated by the GA and MCBS/LMI algorithms would indeed yield a working controller and filter. Consequently, not much attention was paid to tuning the LQG controller and filter (for instance by adjusting the weighting matrices Q and R), which is common in real world design problems (see Table 4A and 4B for the actual values). Hence, Fig. 4A and 4B should not be taken as conclusive statements on the performance of an actual 6-link inverted pendulum, but merely demonstrations of the feasibility of the algorithms discussed here.

3.3 FIGURES AND TABLES

3.3.1 Figures

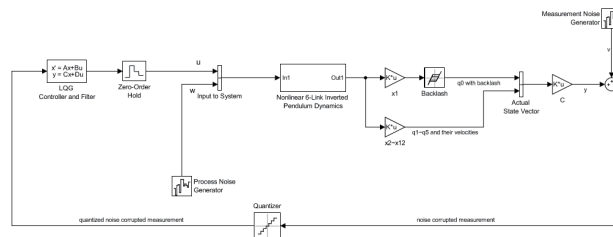


Fig. 1: Closed-loop diagram with modeling of actuator backlash and encoder quantization. Plant includes full nonlinear dynamics. Controller is designed by LQG command in MATLAB using linearized state-space matrices.

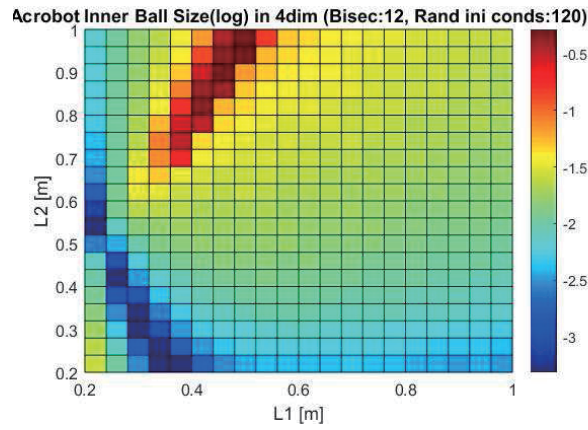


Fig. 2A: Grid search for optimal link lengths L1 and L2 in Acrobot (2-link inverted pendulum). Red indicates greater radius of ROA.

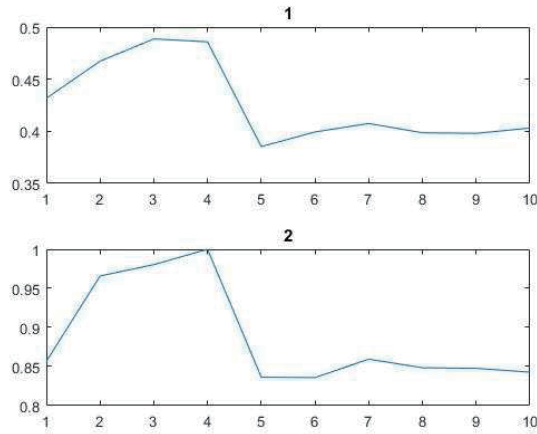


Fig. 2B: Genetic algorithm optimal link lengths for Acrobot (2-link inverted pendulum). Best individual (L1 top, L2 bottom) in given population plotted as a function of generation.

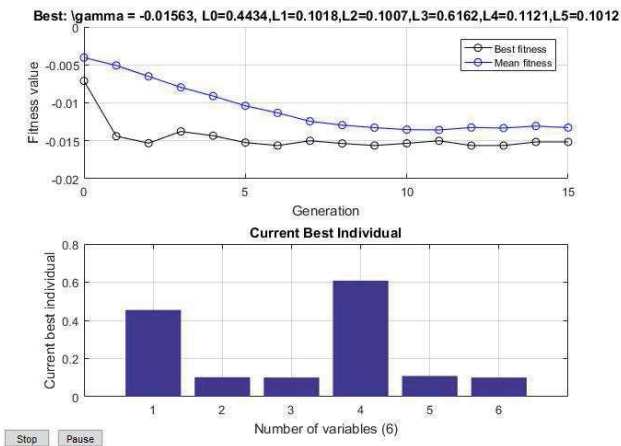


Fig. 3A: Genetic algorithm optimal link lengths for 6-link inverted pendulum with MCBS cost function. Best individual's fitness value, i.e. radius of ROA in given population plotted as a function of generation (top). Bar graph of genetic algorithm optimal link lengths after 15 generations with MCBS cost function (bottom).

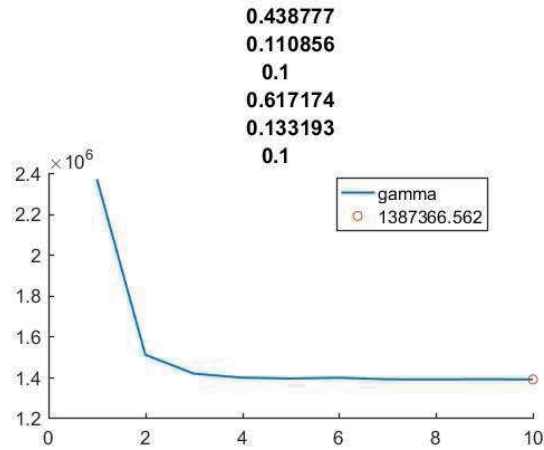


Fig. 3B: Genetic algorithm optimal link lengths for 6-link inverted pendulum with LMI peak response cost function. Best individual's fitness value, i.e. radius of ROA as determined by MCBS (graph) in given population plotted as a function of generation. Final optimal link lengths from link 0 to link 5 after 10 generations (title).

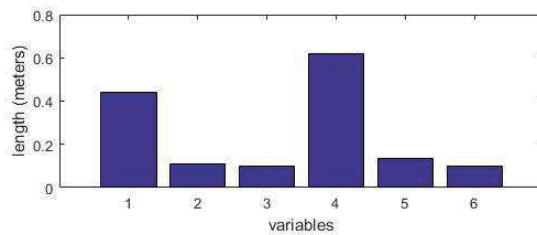


Fig. 3C: Bar graph of genetic algorithm optimal link lengths after 10 generations with LMI peak response cost function.

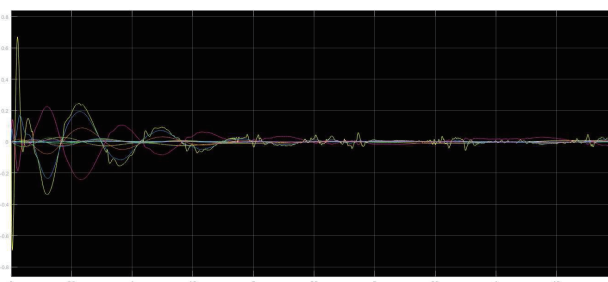


Fig. 4A: Nonlinear states (joint angles and angular velocities) over 2-second simulation with motor backlash and quantization (.0025 degrees, .0055 degrees). Link lengths from GA with MCBS cost. Controller and filter from LQG.

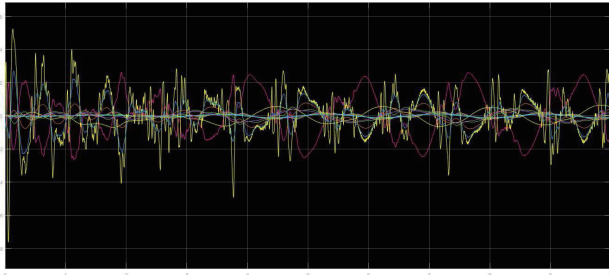


Fig 4B: Nonlinear states (joint angles and angular velocities) over 2-second simulation with motor backlash and quantization (.025 degrees, .055 degrees). Link lengths from GA with MCBS cost. Controller and filter from LQG.

3.3.2 Tables

Table 1: Approximate runtime of each algorithm used to design optimal link lengths.

	GA + LMI	GA + MCBS	Grid Search
2-links (acrobot)	2 min.	2 hrs.	1 day.
6- links	3 min.	20 hrs.	27 years (projected)

Table 2: MCBS Tuning Parameters

M (stability tests)	50
H (bisection iterations)	10

Table 3: GA Tuning Parameters

N (population size)	40
L (number of generations)	[10,15]
Mutation variance	0.01
Minimum link length	0.1
Maximum link length	1
Total link length	1.5

Table 4A: LQG Tuning Parameters in Fig. 4A

Q	I
R	1
W	10^{-10}
V	10^{-20}

Table 4B: LQG Tuning Parameters in Fig. 4B

Q	I
---	-----

R	1
W	10^{-3}
V	1

Table 5: Simulation (Simulink) Parameters

dt (time step)	.001 s
Deadband (Fig. 4A)	.0025 deg.
Deadband (Fig. 4B)	.025 deg.
Encoder resolution (Fig. 4A)	.0055 deg.
Encoder resolution (Fig. 4B)	.055 deg.
ρ (density of links)	2.7 g/cm^3
μ_0 (friction of actuated base joint)	1 N m s
μ_i for $1 \leq i \leq 5$	0.01 N m s

Table 6: Optimal link lengths

Cost Function	r_0	r_1	r_2	r_3	r_4	r_5
MCBS	0.44	0.1	0.1	0.62	0.11	0.1
LMI	0.44	0.11	0.1	0.62	0.13	0.1

4. CONCLUSIONS

The genetic algorithm (GA) combined with the Monte Carlo Bisection Search (MCBS) was successfully able to determine the optimal design parameters based off of estimating and enlarging the region of attraction for the 6-link inverted pendulum. The resulting mechanism and LQG controller was successfully stabilized in simulation in the presence of noise, motor backlash, and limited encoder resolution. The motor deadband and encoder resolution, however, were small compared to most commercially available and inexpensive mechanisms. This highlights the sensitivity of this approach to these “quantization” effects which are not adequately modelled by the LQG framework.

Additionally, when using the GA to determine optimal design parameters, it was shown that minimization of peak response based on linear matrix inequality (LMI) methods was a possible alternative to MCBS based on generating extremely similar link lengths to that of the MCBS method. It is, however, much faster than the MCBS approach, taking only a few minutes to run, whereas MCBS takes a few hours. Another possible advantage of this method is that it simultaneously generates the optimal gain as well. Future work is needed to clarify the direct mathematical relation between the two.

ACKNOWLEDGEMENTS

Thank you to Dr. Susumu Hara, Dr. Daisuke Tsubakino, and Mr. Takamasa Horibe for their wisdom, support, and patience during my stay at Nagoya University and CSEL. This research was made possible by MATLAB, Simulink, and MuPad.

REFERENCES

- [1] Packard, A., Tpcu, U. Seiler, P., Balas, G., Help on SOS, IEEE Control Systems Magazine, 1066-033X, pp. 18-22, (2010).
- [2] Hachicho, O., A Novel LMI-based optimization algorithm for the guaranteed estimation of the domain of attraction using rational Lyapunov functions, Journal of the Franklin Institute, 344, pp. 535-552, (2007).
- [3] Chesi, G., Rational Lyapunov functions for estimating and controlling the robust domain of attraction, Automatica, 49, pp. 1051-1057, (2013).
- [4] Marsden, J. E., Mathematical Systems Theory I Modelling, State Space Analysis, Stability and Robustness, Springer, pp. 675-680 (2005).
- [5] Boyd, S., Ghaoui, L., Feron, E., Balakrishnan, V., Linear Matrix Inequalities in System and Control Theory, SIAM, pp. 37-38 (1994).

(g) The 17th JUACEP Workshop
for the summer research course students from
University of Michigan and UCLA



Date: Friday, August 26, 2016

Venue: NIC 310 Conference Room (3rd floor, NIC)

[Timetable]

- 14:30 - 14:35 Opening address
Prof. Tomohide Niimi, Dean of Graduate School of Engineering
- 14:35 - 14:50 **(1) Chen-Hsi HUANG**, *Okazaki Lab, Applied Chemistry*
“Free energy analysis of biomolecular self-assembly” (Undisclosed)
- 14:50 - 15:05 **(2) Matthew YEE**, *Ohno Lab, Electrical Engineering*
“Carbon nanotube thin film transistors on flexible plastic films” (P.72)
- 15:05 - 15:20 **(3) Itsui YAMAYOSHI**, *Suzuki Lab, Mechanical Science and Engineering*
“Path tracking utilizing LIDAR localization and mapping” (P.75)
- 15:20 - 15:35 **(4) Chih-Kang CHANG**, *Hasegawa Lab, Micro-Nano Systems Engineering*
“Intuitive user interface for surgical tool operation” (P.79)
- 15:35 - 15:50 **(5) Carlos GAMEZ**, *Ju Lab, Mechanical Science and Engineering*
“Temperature dependent thermal-electrical-structural finite element analysis
around crack tip under high current density electropulsing” (P.82)
- 15:50 - 16:00 Break
- 16:00 - 16:15 **(6) Sandeep INGERSAL**, *Shamoto Lab, Mechanical Science and Engineering*
“Study and control of chatter vibrations in milling operation” (P.85)
- 16:15 - 16:30 **(7) Raymond ROMAN**, *Sakai Lab, Mechanical Science and Engineering*
“Time-dependent hemodynamics in stented aneurysms” (P.87)
- 16:30 - 16:45 **(8) Xiaojin SHEN**, *Enokida Lab, Quantum Science and Energy Engineering*
“Experimental measurement and numerical analyses for the molten borosilicate
glass with/without solid particles” (P.91)
- 16:45 - 17:00 **(9) Bonan ZHOU**, *Hara Lab, Aerospace Engineering*
“Estimation in the design of nonlinear control systems” (P.94)
- 17:00 - 17:15 Completion Ceremony
- 17:30 - Farewell Banquet at NIC Hall

*10 minutes presentation + 4 minutes Q&A each

Carbon Nanotube Thin Film Transistors on Flexible Plastic Films

Matthew Yee
8/26/2016
Ohno Research Group

Outline

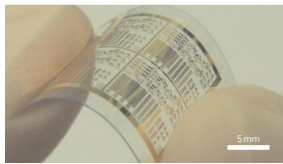
- Background
- Fabrication Process
- Results
- Conclusion

2

Motivations

Flexible Devices

- Plastic substrates
 - Low temperature processing
 - Controlled electrical characteristics



Flexible high-performance carbon nanotube integrated circuits

<http://androidcommunity.com/kyocera-proteus-is-another-flexible-smartphone-20141103/>

3

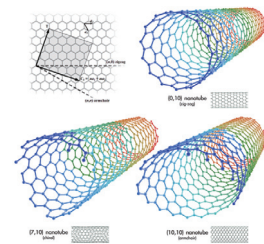
Carbon Nanotubes

CNT Thin Films

- High mobility
- Flexible
- Transparent
- Low temperature processing
- Low cost

CNTs for Transistors

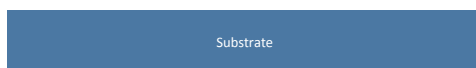
- Single wall
- Semiconducting



<http://www.thenanoage.com/carbon-nanotubes.htm>

4

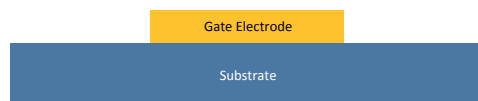
Fabrication



Bottom-gate carbon nanotube thin-film transistor
Substrate – Polyethylene naphthalate (PEN)

5

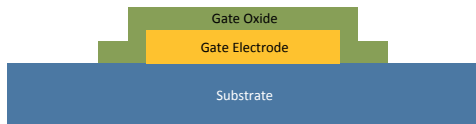
Fabrication



Bottom-gate carbon nanotube thin-film transistor
Gate Electrode – Ti/Au 10/100 nm (Electron Beam Evaporation)

6

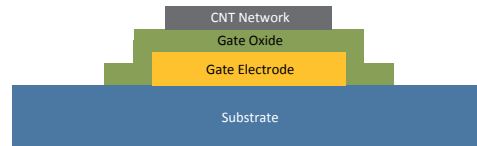
Fabrication



Bottom-gate carbon nanotube thin-film transistor
 Gate Oxide – 40 nm Al_2O_3 (Atomic Layer Deposition)
 TMA and H_2O precursors
 362 cycles at 145 °C

7

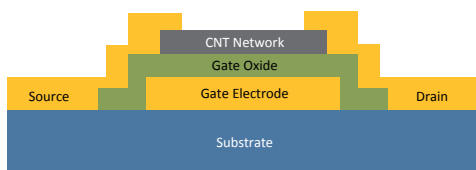
Fabrication



Bottom-gate carbon nanotube thin-film transistor
 CNT Transfer

8

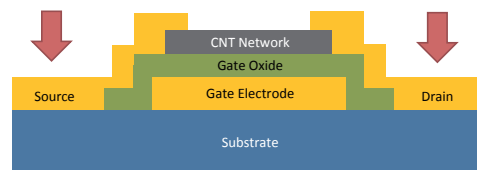
Fabrication



Bottom-gate carbon nanotube thin-film transistor
 Source/Drain Electrode – Ti/Au 10/100 nm (Electron Beam Evaporation)

9

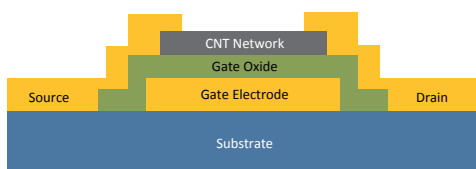
Fabrication



Bottom-gate carbon nanotube thin-film transistor
 Oxygen plasma removes CNTs outside of channel to electrically isolate devices

10

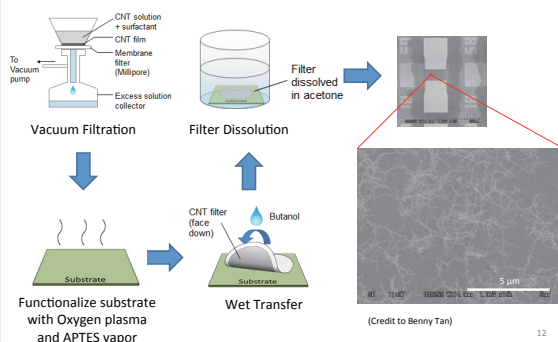
Final Device Structure



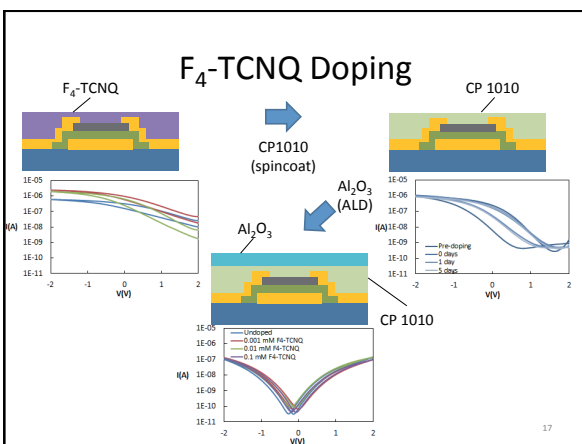
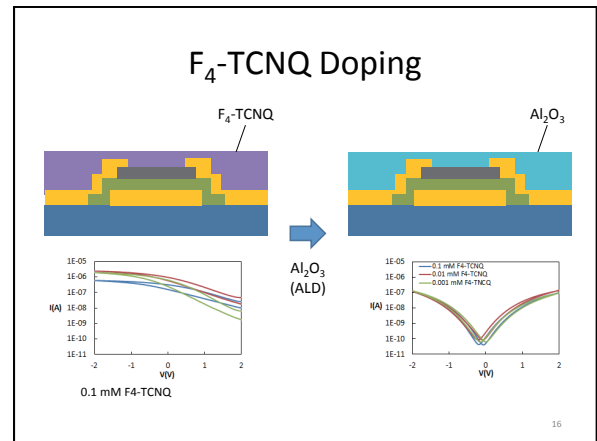
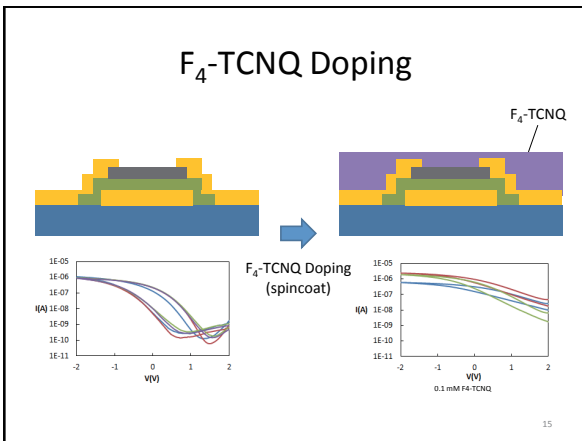
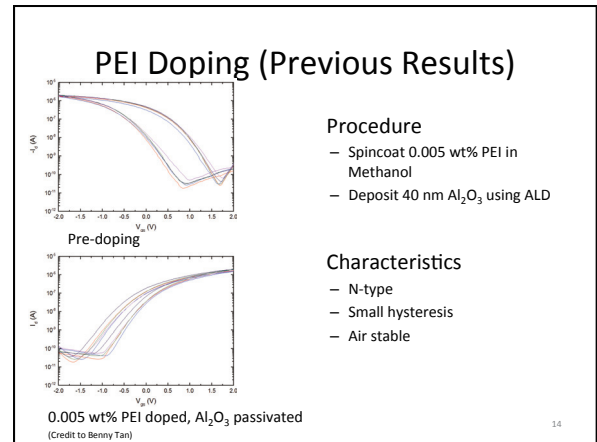
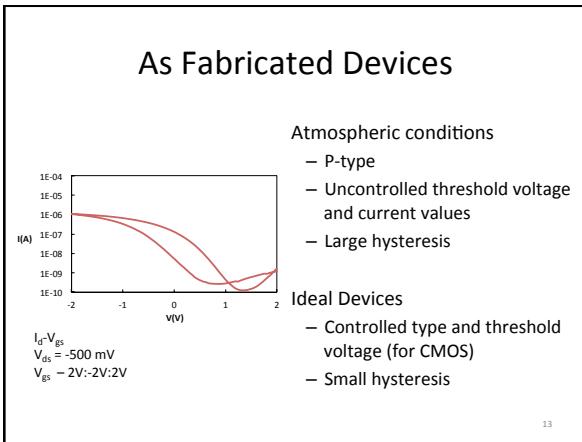
Bottom-gate carbon nanotube thin-film transistor
 Current flows between the source to drain which can be controlled by applying a gate voltage

11

CNT Transfer



12



Conclusion

- F₄-TCNQ evaporates during ALD, resulting in ambipolar devices
 - CP1010 is ineffective as an intermediate layer
- Controlled doping for p-type devices desired for CMOS
 - Less volatile p-type dopant for compatibility with ALD

18


Path Tracking Utilizing LiDAR Localization and Mapping

Itsui Yamayoshi
Department of Mechanical and Aerospace Engineering, UCLA

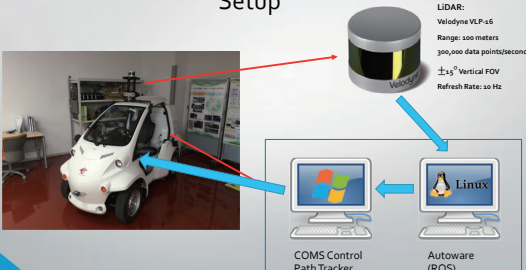
Advisor: Professor Tatsuya Suzuki
Graduate School of Engineering, Nagoya University

Introduction

- Autonomous Vehicle technology has been a subject of great interest. It has seen significant progress and development in the recent decades (i.e. Google/Tesla).
- Autonomous Vehicles have to perform function such as:
 - Localization / Sensing of Environment
 - Path Tracking



Setup



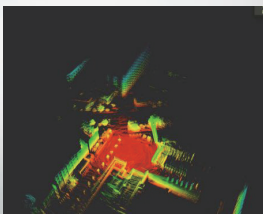
COMS Control Path Tracker Autoware (ROS)

Linux

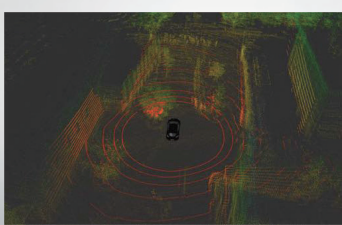
LIDAR:
Velodyne VLP-16
Range: 500 meters
300,000 data points/second
±15° Vertical FOV
Refresh Rate: 50 Hz

LiDAR Localization and Mapping

- For the LiDAR to obtain localization data, it must use an *a priori* known map.
- This map is generated beforehand by recording the LiDAR data as it is driven through the environment. Then, the data is post processed to build an accurate map.

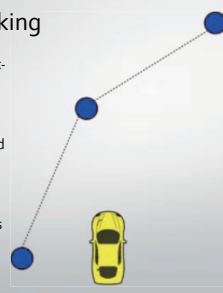


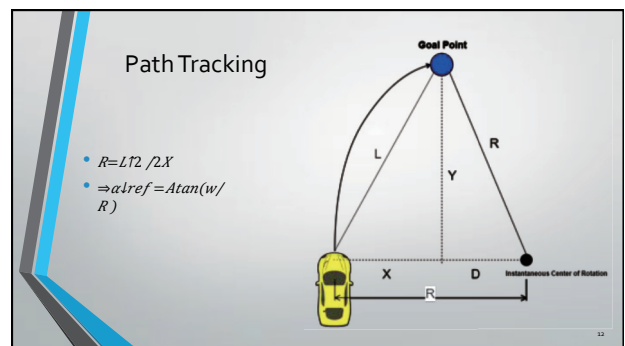
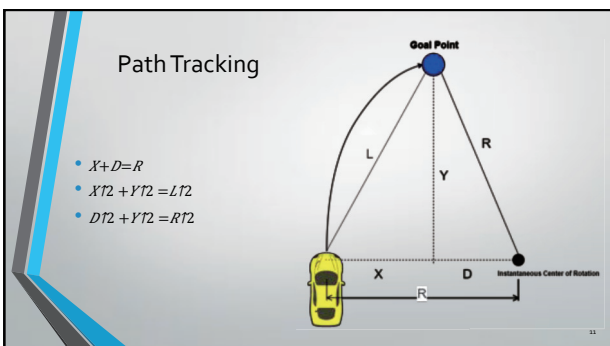
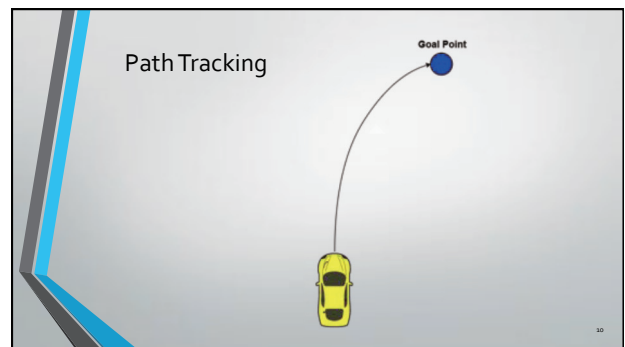
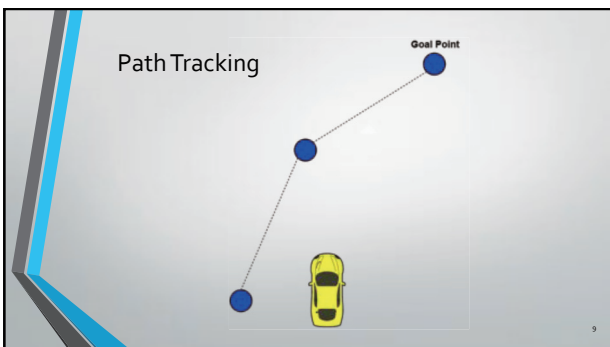
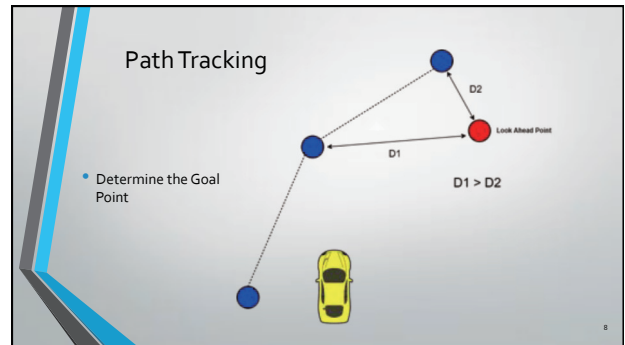
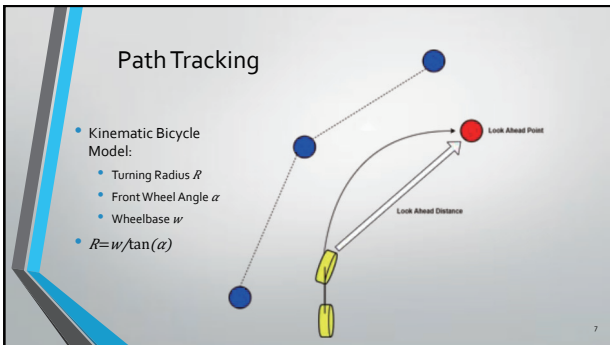
LiDAR Localization and Mapping



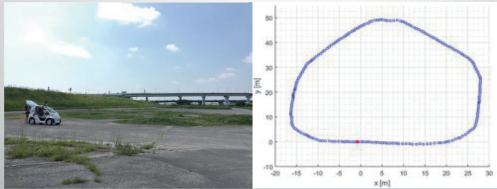
Path Tracking

- Calculate the Look-Ahead Position
- Determine a Goal Point on the path from the Look-Ahead Point
- Find the reference steering angle to drive the car towards the goal point





Experiment



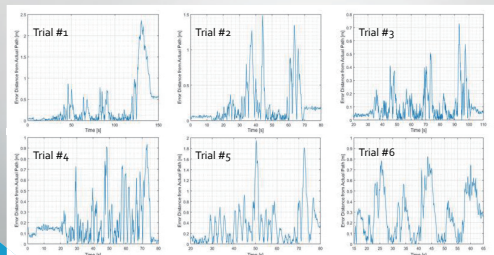
13

Experiment Video



14

Data



15

Results

Trial #	Speed (km/h)	Gain	Look-Ahead (m)	Maximum Error (m)
1	8	0.5	2	2.38
2	12	0.2	3	1.48
3	12	0.2	3	0.94
4	8	0.2	3	0.73
5	12	0.2	3	1.99
6	12	0.2	5	0.82

- Speed can have significant impact on the error and stability.
- Increasing the Look-Ahead distance improves smoothness of steering.

16

Conclusion

- Usage of LiDAR and NDT matching (Autware) to obtain localization data shows reliability in use for path tracking.
- Future work should include:
 - Developing a well suited PID control
 - Variable Look-Ahead Distance
 - More Testing

17

Acknowledgement

- Professor Suzuki
- Members of Suzuki Lab
- Special Thanks to Jason Liang and Professor Okuda for their time and effort helping me with the research.

18

References

- [1] Coulter, R.C., Implementation of the Pure Pursuit Tracking Algorithm, report within CMU-RI-TR-92-01 (1992).
- [2] Sneider, J.M., Autonomous Steering Methods for Autonomous Path Tracking, report within CMU-RI-TR-09-08 (2009).
- [3] Lundgren, M., Path Tracking of Miniature Robot, Master's Thesis, Dept. of Computer Science, Umea University (2009).
- [4] Giesbrecht, J., Mackay, D., Collier, J., Verret, S., Path Tracking for Unmanned Ground Vehicle Navigation, Defense Research and Development Canada (2005).
- [5] Hoffman, G.M., Tomlin, C.J., Montemero, M., Thrun, S., Autonomous Automobile Trajectory Tracking for Off-Road Driving, Controller Design, Experimental Validation and Racing, Proc. 26th Amer. Control Conf., pp. 2296-2301 (2007).
- [6] Wolcott, R.W., Eustice, R.M., Visual Localization within LIDAR Maps for Automated Urban Driving, Intelligent Robots and Systems (IROS 2014), 2014, IEEE/RSJ International Conference on, pp. 276-283 (2014).
- [7] Biber, P., The Normal Distributions Transform: A New Approach to Laser Scan Matching, *IEEE/RSJ International Conference on*, 2003, pp. 2743-2748 vol.3 (2003).
- [8] Morales, J., Martinez, J.L., Martinez, M.A., Mandow, A., Pure-Pursuit Reactive Path Tracking for Nonholonomic Mobile Robots with a 2D Laser Scanner, *EURASIP Journal on Advances in Signal Processing*, Volume 10 (2008).

Hasegawa Lab, Micro-Nano Systems Engineering

Intuitive User Interface For Surgical Tool Operation

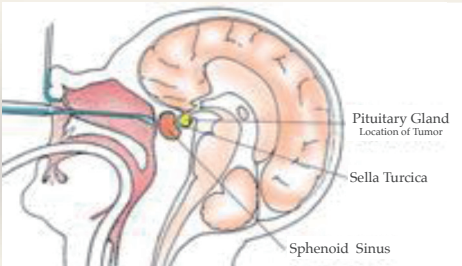
Chang Chih-Kang
Masters in Robotics Program,
University of Michigan

Outline

- ❖ Introduction
 - ❖ Endoscopic Transnasal Pituitary Surgery
 - ❖ Robotics Surgical Tool
- ❖ Research Content
 - ❖ Haptic Force Feedback
 - ❖ Tool Constraint
- ❖ Conclusion

2

Endoscopic Transnasal Pituitary Surgery



http://neurosurgery.ufl.edu/patient-care/diseases-conditions/pituitary-tumors/

3


Endoscopic Transnasal Pituitary Surgery

- ❖ Video (2:05-)
- ❖ <https://www.ypo.education/neurology/endoscopic-transnasal-transphenoidal-surgery-t167/video/>

4

Robotics Surgical Tool

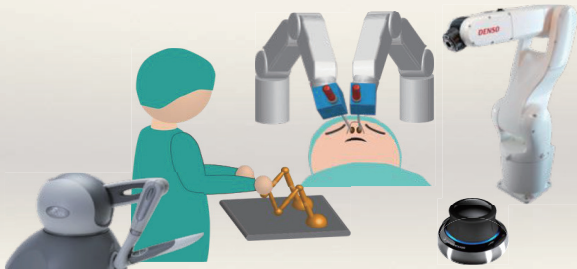
- ❖ Minimally invasive
- ❖ High dexterity
- ❖ High precision
- ❖ Ease for doctor
- ❖ Remote surgery



da Vinci

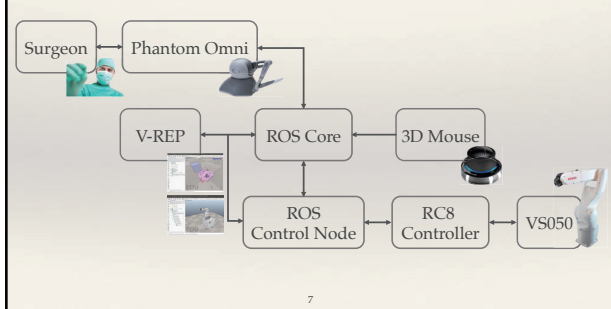
5

Surgical Tool Architecture



6

Surgical Tool Architecture



7

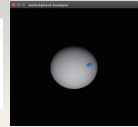
Haptic Technology

- ❖ Sense of touch
- ❖ Creation of virtual objects
- ❖ Remote control of machines and devices (telerobotics)

Spring Model

```

// Use Fkx to create a force vector that is away from the center of
// the sphere and proportional to the penetration distance, and scaled
// by the object stiffness.
// Hooke's law explicitly:
double k = sphereStiffness;
hdVector3d x = penetrationDistance*forceDirection;
hdVector3d f = k*x;
hdSetDouble(HD_CURRENT_FORCE, f);
  
```



8

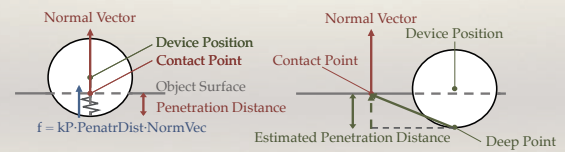
Phantom Omni

- ❖ 6 DOF positional sensing
- ❖ 3 DOF force feedback
- ❖ OpenHaptic



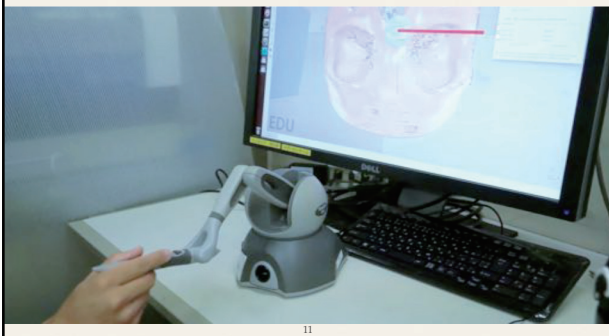
9

Haptic Force Feedback



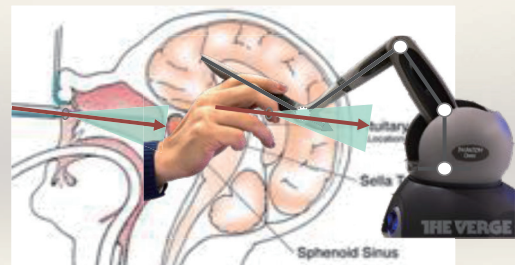
10

Result Video



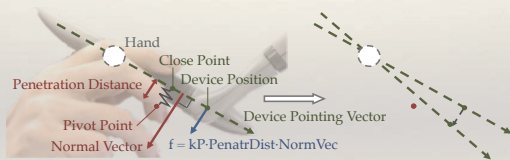
11

Tool Constraint



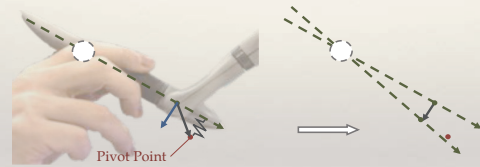
12

Tool Constraint



13

Tool Constraint



14

Result Video



15

Conclusion

- ❖ Haptic Force Feedback + Tool Constraint
- ❖ Future Work
 - ❖ Improve Haptic
 - ❖ Arm + Tool
 - ❖ Real Test

16

Thank you

Question?

TEMPERATURE DEPENDENT THERMAL-ELECTRICAL-STRUCTURAL FINITE ELEMENT ANALYSIS AROUND CRACK TIP UNDER HIGH CURRENT DENSITY ELECTROPULSING

Carlos Gámez
August 26, 2016

Supervisor: Prof. Yasuyuki Morita

UCLA NAGOYA UNIVERSITY

Presentation Outline

- Introduction
- Experimental Procedure
- Numerical Solution In Abaqus
 - Governing Equations
 - Material Properties
 - Interactions
 - Geometry And Mesh
 - Boundary Conditions and Loading
- XFEM Analysis (Damage Initiation)
- Results
- Conclusion

UCLA NAGOYA UNIVERSITY

Introduction

- Crack propagation is a failure mode that is frequently present in metal alloys.
- Electropulsing treatment is an efficient method to arrest cracks.
 - Uses high electrical current density in a short period of time (1.5ms).
 - Eliminates the stress concentration at the crack tip.
- Abaqus is used to calculate the temperature and stress field around the crack tip.

UCLA NAGOYA UNIVERSITY

Experimental Procedure

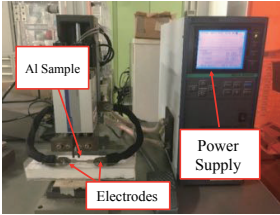


Fig. 1 Experimental Setup.

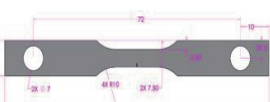


Fig. 2 All dimensions in mm.

- Al 6061-T6 sample
- 0.5mm thick by 5 mm tall
- A single-edge crack of 0.140mm wide and 1mm long

UCLA NAGOYA UNIVERSITY

Numerical Solution In Abaqus

Governing Equations

Joule Heating

(1) $P = \text{Joule heating power,}$
 $I = \text{Electric current}$
 $R = \text{Resistance}$

Heat Flow

(2) $\rho = \text{Density}$
 $C_p = \text{Specific Heat}$
 $k = \text{Thermal Conductivity}$
 $Q = \text{Heat Generation}$

Thermal Stress

(3) $\sigma = \text{Stress}$
 $E = \text{Young's modulus}$
 $\alpha = \text{Thermal Expansion Coefficient}$
 $\Delta T = \text{Change in Temperature}$

$P = \text{Joule heating power,}$
 $I = \text{Electric current}$
 $R = \text{Resistance}$

$\rho = \text{Density}$
 $C_p = \text{Specific Heat}$
 $k = \text{Thermal Conductivity}$
 $Q = \text{Heat Generation}$

$\sigma = \text{Stress}$
 $E = \text{Young's modulus}$
 $\alpha = \text{Thermal Expansion Coefficient}$
 $\Delta T = \text{Change in Temperature}$

UCLA NAGOYA UNIVERSITY

Numerical Solution In Abaqus

Material Properties

Material	T (°C)	k (W·m ⁻¹ ·K ⁻¹)	C _p (J·kg ⁻¹ ·K ⁻¹)	ρ (kg·m ⁻³)	E (GPa)	α (x10 ⁻⁶ ·K ⁻¹)
Al Alloy 6061-T6	0	161	917	2703	69.7	22.4
	98	177	978	2685	66.2	24.61
	201	192	1028	2657	59.2	26.6
	316	207	1078	2630	47.78	27.6
	428	223	1133	2602	31.72	29.6
	571	253	1230	2574	0	34.2

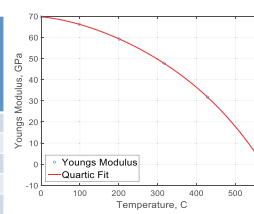


Fig. 3 Young's Modulus polynomial curve fitting, where $h_1 = -3.9e^{-10}$, $h_2 = 2.73e^{-7}$, $h_3 = -0.00021$, $h_4 = -0.017$, $h_5 = 69.7$.

UCLA NAGOYA UNIVERSITY

Numerical Solution In Abaqus

Interactions, Boundary Conditions and Mesh

Heat loss:
 -Natural convection
 -Radiation

- Four corners are fixed in the Z direction allow free expansion in the XY plane

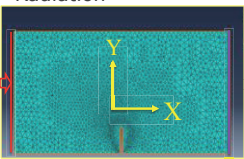
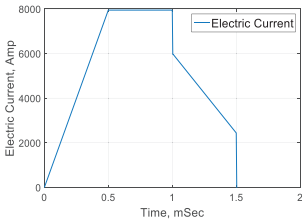


Fig. 4 Tet mesh. Global element size 0.0002m. Refine element size at crack tip of 2×10^{-5} m.

UCLA NAGOYA UNIVERSITY

Numerical Solution In Abaqus

Electrical Load



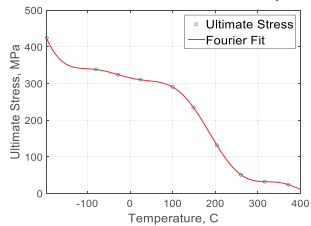
Max ECD is $3.2 \times 10^9 \text{ A/m}^2$

Fig. 5 Electric current profile obtained from the power supplied

UCLA NAGOYA UNIVERSITY

Numerical Solution In Abaqus

XFEM Analysis
 Damage Initiation Criteria:
 - Maximum Principal Stress.



The fracture energy, $G_{IC} = 24.2 \text{ kN/m}$, was used for the damage evolution criteria

Fig. 6 Ultimate tensile stress Fourier Fit.

UCLA NAGOYA UNIVERSITY

Results

Electric Current Density and Temperature Field.

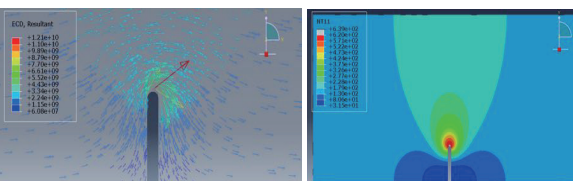


Fig. 7 Electrical Current Density Vectors at $t=1.0\text{ms}$

Fig. 8 Temperature field at $t=1.0\text{ms}$.

UCLA NAGOYA UNIVERSITY

Results

Stress Field.

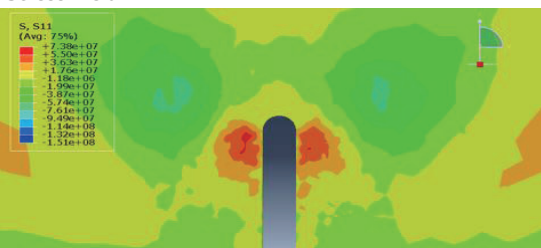


Fig. 9 Tensile Stress (X direction) at $t=1.0\text{ms}$

UCLA NAGOYA UNIVERSITY

Results

Melted Region.

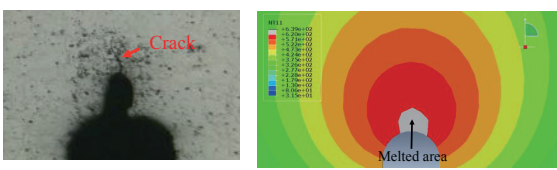
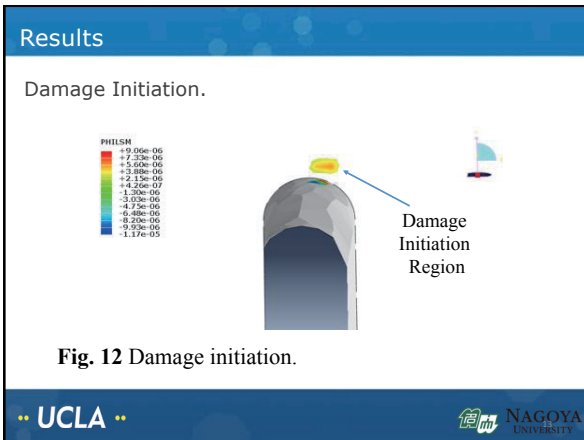


Fig. 10 Crack tip after electropulsing treatment. The melted area has an approximate diameter of 0.06mm.

Fig. 11 Melted area in grey, approximately 0.01mm difference in diameter between the experiment result.

UCLA NAGOYA UNIVERSITY



Conclusions

- The temperature-dependent numerical model calculates the Temperature and Stress fields accurately.
- The stress field is dependent on the temperature gradient field and the displacement boundary conditions.
- The experimental melted area agrees with the melted area obtained in the simulation.
- The damage initiation model needs to be more precise with the location and size of the failure zone.

UCLA NAGOYA UNIVERSITY

Acknowledgements

This work was supported by all the people involved in the JUACEP program, including Professor Ju, the Ju Lab and Lin Yang for their contributions to this work

¡Gracias!

UCLA NAGOYA UNIVERSITY

Ultra Precision Engineering Laboratory
(Prof. Shamoto Laboratory)

Study and Control of Chatter Vibrations in Milling Operation

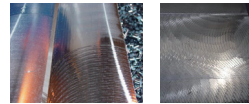
Sandeep Kumar Ingersal
(Guided by Assistant Professor Hayasaka & Prof. Shamoto)
JUACEP Program
Nagoya University - University of Michigan

Date: 08.26.2016

Background and Objective

Background

- Dies and molds have deep and narrow groove designs, where slender end mills are used for milling
- These end mills are subjected to **chatter vibration** which creates chatter marks on the machined surface.



Negative Effects of Chatter

- Poor Surface finish
- Excessive noise
- Disproportionate tool wear
- Reduced Metal Removal Rate
- High Production Cost

Objective

- To determine the effect of direction of cutting in the chatter stability in milling process

Milling Process

What kind of process is Milling?

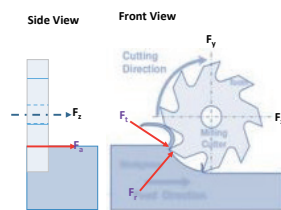
It's an intermittent cutting process with one or more teeth.

Forces Considered in Milling

- Tangential F_t
- Radial F_r
- Axial F_a

The components of these forces are added along

- Feed F_z
- Normal F_y
- Axial F_x

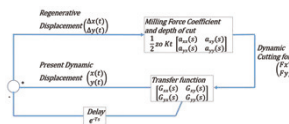
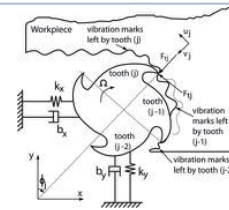


Chatter Vibrations in Milling

Regenerative Chatter

Cause:

The phase difference between the wave left by the previous teeth and the wave left by the current ones build up regenerative chatter



Mode-Coupling Chatter

Cause:

coupling of the vibrations and forces in two directions

No Chatter Condition – Stability Limit

Using Hammer Test, the transfer function of the system is found

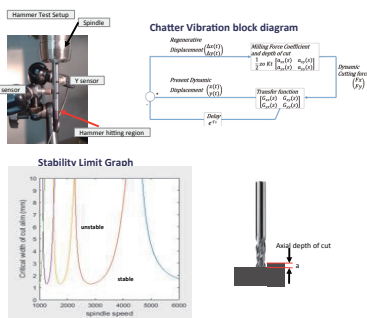
$$\text{Transfer Function } G(s) = Y(s) / F(s)$$

$G(s)$ -> displacement per unit force in frequency domain

By solving the equation obtained from Zero-Order Solution

$$\det([I - 1/2 K \alpha (1 - e^{-sT})] A_d) = 0$$

a_{crit} for different spindle speed n (or Time period T) is obtained for a dominant range of chatter frequency



Effect of Machine Design in Transfer Function

- Generally, the machine structure is not fully symmetric
- The transfer function changes in X & Y direction of the machine

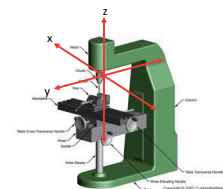
$$\text{Transfer function } \begin{bmatrix} G_{xx}(s) & G_{xy}(s) \\ G_{yx}(s) & G_{yy}(s) \end{bmatrix} \chi(s)$$

Direct Compliance Factors

- G_{xx} – X direction Vibration, impulse in X direction
- G_{yy} – Y direction Vibration, impulse in Y direction

Cross Compliance Factors

- G_{xy} – X direction Vibration, impulse in Y direction
- G_{yx} – Y direction Vibration, impulse in X direction



Though tools vibrates with very less amplitude perpendicular to the impact direction, the cross compliance G_{xy} and G_{yx} have an effect on Chatter

Analysis of Chatter Vibration

Cutting Tool Direction

- Transfer function matrix changes for different direction of cutting of the milling tool
- This in turn change the **stability limit** of the system

Direction of Cutting

Bottom Cut

Transfer function
 $\begin{bmatrix} G_{yy}(s) & G_{xy}(s) \\ G_{yx}(s) & G_{xx}(s) \end{bmatrix}$

Side Cut

Transfer function
 $\begin{bmatrix} G_{yy}(s) & -G_{lyx}(s) \\ -G_{lvy}(s) & G_{lx}(s) \end{bmatrix}$

Analytically predicted results

- Stability limit for Side and Bottom for the given machine
- Analytically, the stability limit for bottom cut >> side cut

The Side and Bottom lobes stability results
Immersion Angle = 40deg

$\begin{matrix} S \\ i \\ O \\ T \\ a \\ n \\ g \\ l \\ e \end{matrix}$

Experimental Validation

Purpose
 To validate the analytical results and effect of cross-components in the mode-coupling chatter

Details

- Down Milling process
- Uses variable pitch end mill cutter
- Sensors measure the vibration in x and y direction

Method

- A rectangular workpiece is machined in two different direction (side & bottom)
- Speed is fixed
- Axial depth of cut is varied from **0 to 0.6 mm**

Condition
 Spindle speed = 5600 min⁻¹
 Feed Rate = 342 m/min
 Immersion Angle = 40°

Experiment Setup

Experiment Results

Results

Inference

- The direction of cutting has an effect on the chatter stability
- The cross-compliance factors have an effect on stability
- High metal removal rate(MRR) can be performed in machining the effective side (or the effective direction)

a = 0.35mm

X direction

Y direction

a = 0.45mm

X direction

Y direction

a = 0.6mm

X direction

Y direction

Time-Dependent Hemodynamics in Stented Aneurysms

Ray Roman
 August 24, 2016
 JUACEP Independent Research

Basics

Basics

- Invasive treatments (e.g., coiling)
- Flow diversion treatment (e.g. pipeline)

2

Basics

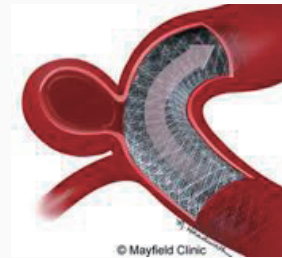


FIGURE 1: Flow diverter stent.

3

Basics

$$WSS = \mu \frac{du}{dr}$$

wall shear stress

$$AFI = \frac{WSS \cdot \overline{WSS}}{|WSS| + \overline{WSS}}$$

aneurysm formation index

4

Basics

- Successful?
- Motivation for research
- Goals: characterize flow, cause of rupture

5

Methods

Methods

- 💡 Idea: *four models—8 mm with(out) stent, 12 mm with(out) stent.*
- ⚙️ SolidWorks, Blender: *construct model*
- 💧 OpenFOAM: *run simulations*
- 📊 ParaView: *analyze results*

6

Methods

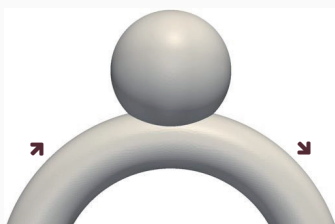


FIGURE 2: "Outside" configuration.

7

Methods

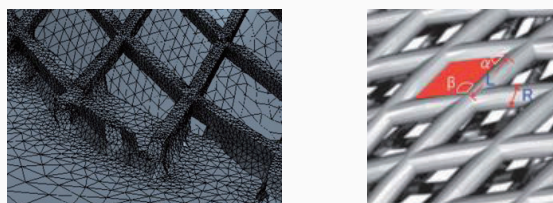


FIGURE 3: Visualizing the aneurysm + stent model.

8

Methods

The big questions

- ❓ Could the mechanical variation that is observed on aneurysm walls provide a hint about aneurysm rupture?
- ❓ Does it communicate any information about flow near the walls of an aneurysm?

9

Results

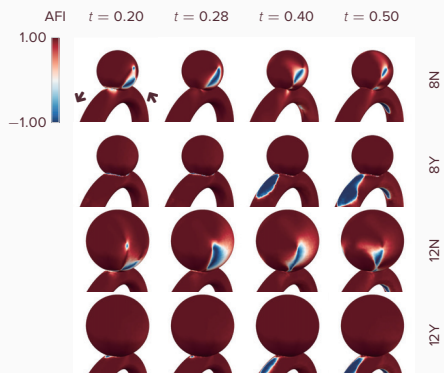


FIGURE 4: Aneurysm formation index results.

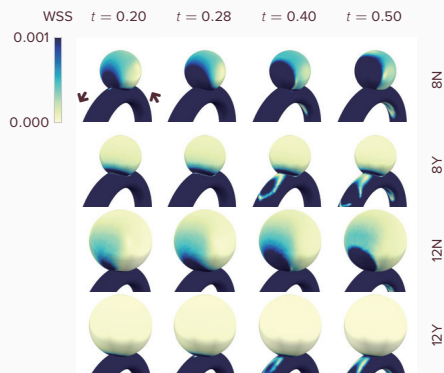


FIGURE 5: Wall shear stress results. Units in kilopascal.

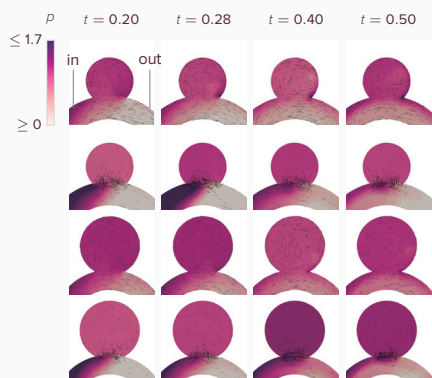


FIGURE 6: Center plane. Shading represents pressure, and pressure varies from case to case.

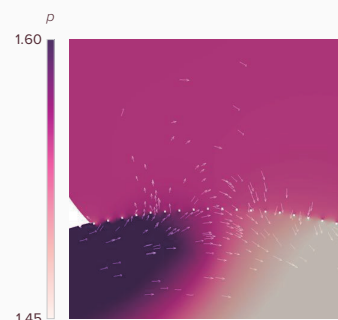


FIGURE 7: Center plane detail.

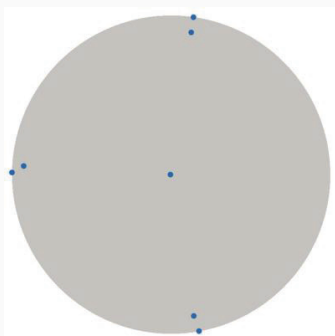


FIGURE 8: Sampled points. Left is proximal wall, right is distal wall.

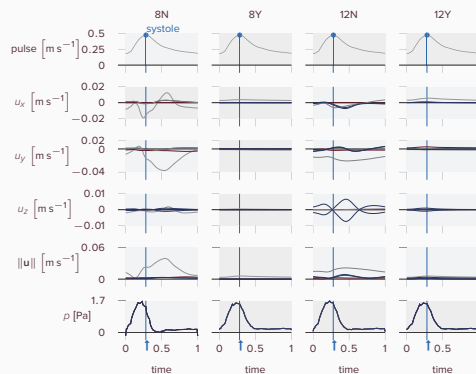


FIGURE 9: Time series of inner points.

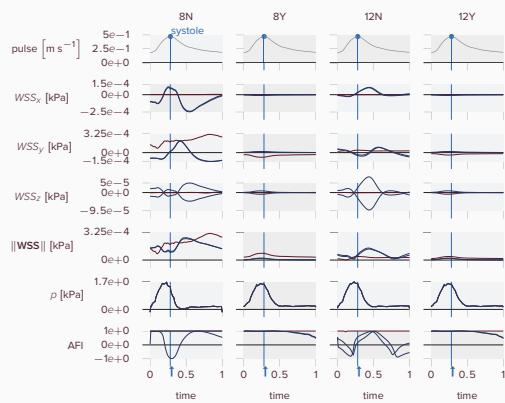


FIGURE 10: Time series of outer points.

Discussion

Main takeaways

- Pressure plays huge role (Bouillot et al., 2015).
- Internal flow patterns uninformative.
- Limitations?

17

Wrap up...

References

- Bouillot, P., Brina, O., Ouared, R., Lovblad, K.-O., Farhat, M., and Pereira, V. M. (2015). Hemodynamic transition driven by stent porosity in sidewall aneurysms. *Journal of Biomechanics*, 48(7):1300–1309.
- Diaz, O. and Rangel-Castilla, L. (2016). Endovascular treatment of intracranial aneurysms. In *Handbook of Clinical Neurology*, pages 1303–1309. Elsevier BV.
- Rinkel, G. J. E., Djibuti, M., Algra, A., and van Gijn, J. (1998). Prevalence and risk of rupture of intracranial aneurysms: A systematic review. *Stroke*, 29(1):251–256.

18

NAGOYA UNIVERSITY 原子力化学工学研究室

Experimental measurement and numerical analyses for the molten borosilicate glass with/without solid particles

XIAOJIN SHEN

Supervised by: Prof. Enokida, Prof. Sugiyama
17th JUACEP workshop
8/26/2016

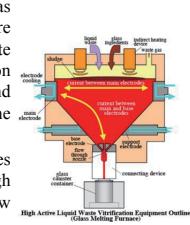
1

NAGOYA UNIVERSITY 原子力化学工学研究室

Background and Introduction

Vitrification is a widely used technology and has been applied for nuclear waste reprocessing for more than 40 years including high level nuclear waste (HLW) immobilisation. However during vitrification the crystallization of ruthenium dioxide (RuO₂) and other metal element like Pd-Te alloy can effect on the viscosity of the glassy melt.

The sedimentation of solid particles lead to troubles of local over-heating, electric energy loss, high viscous glass formation and unexpected low production rate of the vitrification.



2

NAGOYA UNIVERSITY 原子力化学工学研究室

Research Purpose

In order to investigate the rheological phenomenon influenced by those solid particles in the molten glass, there are two primary goals

- (1) to conduct the viscosity measurement of the molten glass for the original simulated glass obtained from CRIEPI (Central Research Institute of Electric Power Industry).
- (2) to simulate the local phenomenon in the melter for the glassy melt with/without solid particles by ANSYS/Fluent 16.2.

Extending upon on the previous work in Nuclear Chemical Engineering lab, which investigated the single-phase effect from spherical RuO₂ into the glass matrix.

3

NAGOYA UNIVERSITY 原子力化学工学研究室

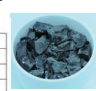
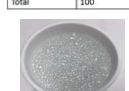
Material compositions

- White beads
- Original simulated glass of nuclear waste reprocessing from CRIEPI

Components	Fraction, wt%
Na ₂ O	4
SiO ₂	60
B ₂ O ₃	18.2
CaO	3.8
Al ₂ O ₃	6.4
ZnO	3.8
Li ₂ O	3.8
Total	100

Components	Fraction, wt%
SiO ₂	40.1
Na ₂ O	12.9
B ₂ O ₃	12.1
Al ₂ O ₃	4.65
Ni ₂ O ₃	2.95
CaO	2.92
Li ₂ O	2.56
ZnO	2.51
MnO	2.39
Ce ₂ O ₃	2.12
ZrO ₂	2.06
La ₂ O ₃	1.58
Gd ₂ O ₃	1.27
Fe ₂ O ₃	1.18

Components	Fraction, wt%
Cu ₂ O	1.12
Pb ₂ O ₃	0.84
BaO	0.63
NiO	0.56
RuO₂	0.53
Sr ₂ O ₃	0.35
Mn ₂ O ₃	0.34
PbO	0.32
Cr ₂ O ₃	0.31
SeO	0.23
Y ₂ O ₃	0.17
Rh ₂ O ₃	0.13
Te₂O₃	0.06
Total	96.9

4

NAGOYA UNIVERSITY 原子力化学工学研究室

Experimental Methodology

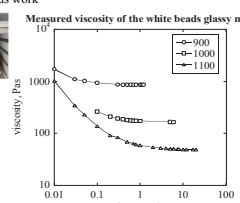
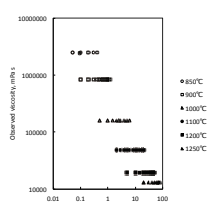
- To conduct the viscosity measurements of the borosilicate glass
 - Measured the viscosity for white beads in 900, 1000, 1100 °C to verify the previous measurement
 - Conducted XRD analyses and composition analyses for the modified simulated glass (Enriched/Purified) followed by thermal treatment of the original simulated glass in 1100 °C for 100 hours.
 - Measured the viscosity for enriched bottom and purified top glasses and compared the value with the mother glass
- To simulate the rheological phenomenon for the molten glass
 - Simulated the natural convection for white beads with/without RuO₂ in a square enclosure
 - Simulated the glassy melt flowing along an inclined plane for original simulated glass and the glass free of crystalline materials

5

NAGOYA UNIVERSITY 原子力化学工学研究室

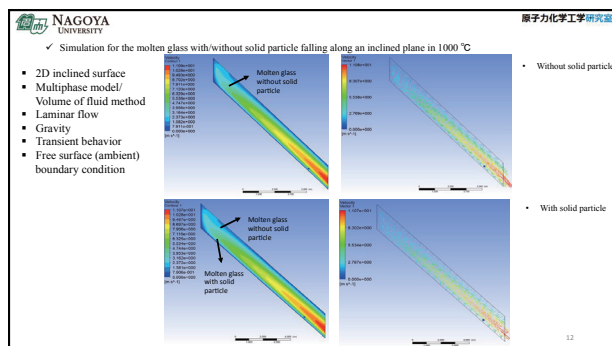
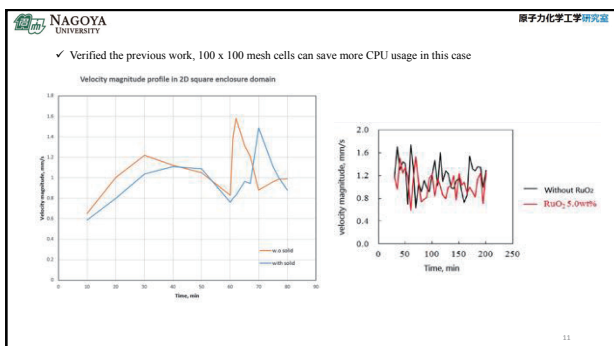
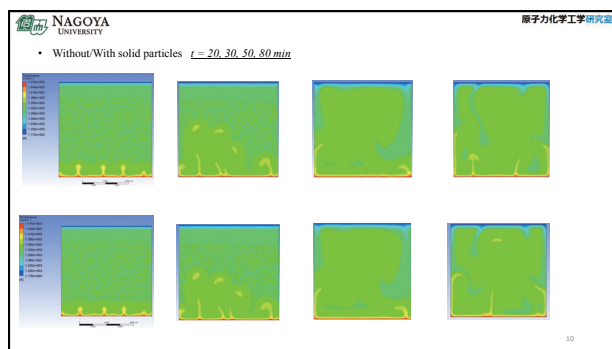
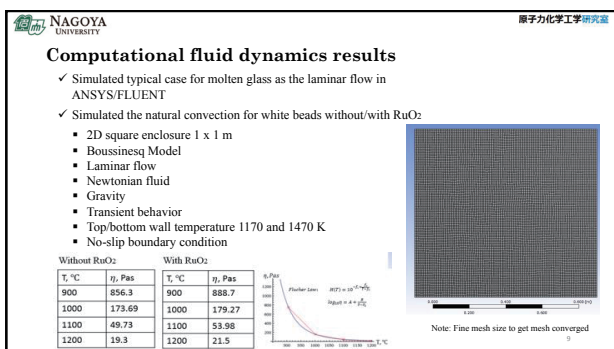
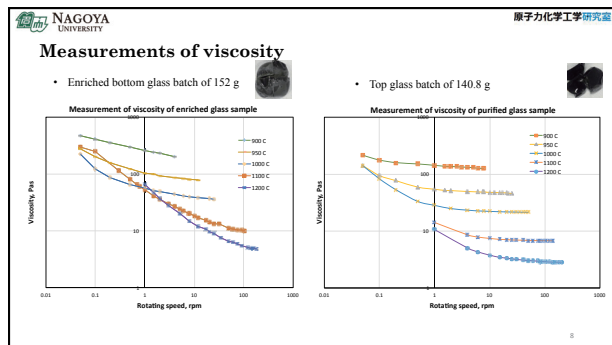
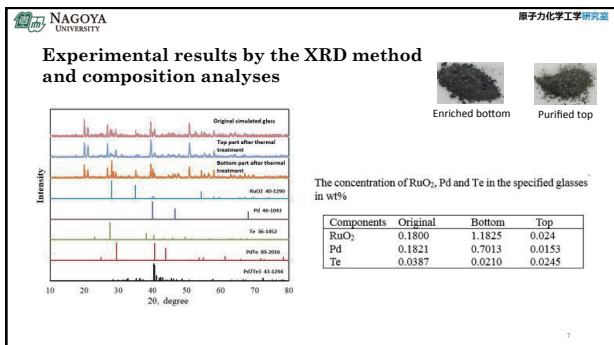
Measurements of viscosity for the white beads

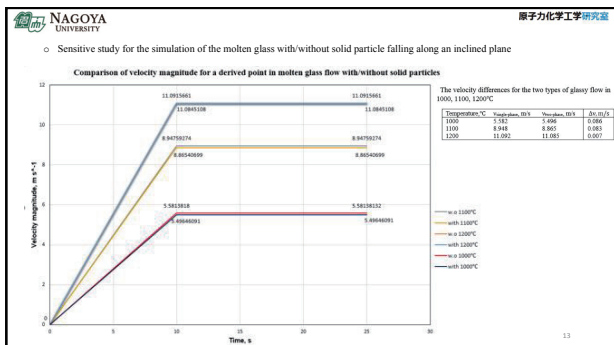
white beads batch of 200 g in 900, 1000, 1100 °C and verified the measurement result by the previous work

Note: The experimental data provided as the input material property for computational analyses

6





NAGOYA UNIVERSITY 原子力化学工学研究室

Conclusion and future work

- The white beads glassy melt without/with 5% RuO₂ can be treated as Newtonian fluid.
- The enriched bottom glass has shown as the Non-Newtonian fluid property.
- The viscosity gets increased caused from the increased concentration of RuO₂ and Pd-Te alloy.
- From the sensitivity study of the inclined plane, it has been shown that by increasing the operating temperature of the melter, the velocity variance for white beads glassy melt without/with 5% RuO₂ will become smaller.

o Experimental study:
 To investigate under which weight fraction of crystalline contents can make glassy melt as non-Newtonian fluid
 To investigate the single-phase effect from Pd-Te alloy into the glass matrix

o Numerical study:
 To simulate the physical phenomenon for the Non-Newtonian fluid

14

NAGOYA UNIVERSITY 原子力化学工学研究室

References

- [1] Yoshida, Master's thesis, (2015).
- [2] M. John Plodinec, RHEOLOGY OF GLASSES CONTAINING CRYSTALLINE MATERIAL, (1986).
- [3] NETL's non-Newtonian Multiphase Slurry Workshop Report, (2013).
- [4] Rokkasho Reprocessing Plant: Vitrification Problems Continue, CNIC.
- [5] Vinay Ramohalli Gopalrao, Jan-Aiso Lycklama à Nijeholla, Paul Bakkerb, Benno Haverkate, Development and validation of a CFD model predicting the backfill process of a nuclear waste gallery, (2011).
- [6] Sandia National Laboratories, Multiscale Models of Nuclear Waste Reprocessing: From the Mesoscale to the Plant-Scale, (2012).
- [7] Y.Enokida, Kayo Sawada, Takahiro Shimada, and Daisuke Hirabayashi, Formation Mechanisms of the Needle-shaped Crystals of Ruthenium Dioxide during Vitrification of Nitric Acid Solution Containing Nitrosyl Ruthenium Nitrate, (2011).
- [8] Vinit Khandelwal, Amit Dhiman, Laszlo Baranyi, Laminar flow of non-Newtonian shear-thinning fluids in a T-channel, (2014).

I would like to acknowledge my supervisors' help throughout the project and the special thank to my TA Uchimura's assistance for this project.
 Thanks for all labmates and friends' company in this program.

15

ESTIMATION IN THE DESIGN OF NONLINEAR CONTROL SYSTEMS

Julian Zhou

1

BACKGROUND

CONTROL THEORY:

The framework which governs dynamic systems closed under feedback

LINEAR DYNAMIC SYSTEM:

$$dx/dt = Ax + Bu$$

$$u = kx$$

NONLINEAR DYNAMIC SYSTEM:

$$dx/dt = f(x) + g(u)$$

$$u = kx$$

2

PROBLEM

NONLINEAR MECHANISM:

6-link Inverted Pendulum $(dx/dt = f(x) + g(u))$

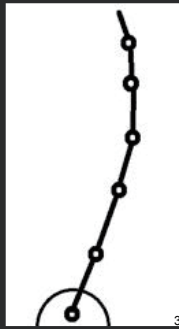
LINEAR CONTROL LAW:

Actuated base joint applies correction

proportional to encoder angles $(u = kx)$

BUT HOW BIG DO WE MAKE EACH LINK?

And on what basis would one design be better?



3

SOLUTION

COST FUNCTION

1. Maximize REGION OF ATTRACTION (ROA)

2. Minimize PEAK RESPONSE

MAXIMIZING THE COST FUNCTION

1. Grid search

2. Gradient methods

3. Genetic algorithm

4

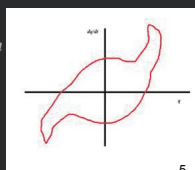
REGION OF ATTRACTION (ROA)

PHASE SPACE

Graphical representation of positions/velocities of all the degrees of freedom (DOF) of the system. N DOF \rightarrow $2N$ DIMENSIONAL PHASE SPACE.

REGION OF ATTRACTION

Portion of PHASE SPACE where nonlinear system is stable (all positions and velocities decay to 0).



5

ENLARGING THE ROA

DESIGN CONSTRAINT

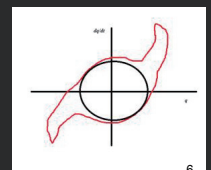
We want to estimate the ROA, but specifically the quasi-spherical part

LARGEST INTERIOR SPHERE

1. Grid search

2. Deterministic Bisection Search

3. Monte Carlo Bisection Search



6

MONTE CARLO BISECTION SEARCH (MCBS)

PEAK RESPONSE

LINEARIZATION:

$$dx/dt = f(x) + g(u) \quad \rightarrow \quad dx/dt = Ax + Bu$$

WHERE

$$A = df/dx \quad (x = 0)$$

$$B = g(0)$$

LINEARIZATION BECOMES WORSE AS SYSTEM DISEQUILIBRATES.
MINIMIZING PEAK RESPONSE SHOULD "HELP".

MINIMIZING PEAK RESPONSE

SOLVABLE WITH LINEAR MATRIX INEQUALITY

$$\min \kappa(P)$$

$$\kappa(P) = \lambda_{\max}(P) / \lambda_{\min}(P)$$

$$P(A+BK) + (A+BK)'P + 2\beta P < 0,$$

MUCH FASTER THAN MONTE CARLO BISECTION SEARCH
DOES NOT HAVE A CLEAR RELATIONSHIP WITH THE ROA

HOW TO SEARCH OPTIMIZATION SPACE?

max ROA or.... min PEAK RESPONSE

GRID SEARCH is on the order of |RESOLUTION|^6 or about 12 YEARS.
GRADIENT methods are not robust.
GENETIC ALGORITHMS are heuristic but amazing.

GENETIC ALGORITHM (GA)

(0. Randomly generate starting population.)

1. TEST population according to chosen cost function.
2. KILL bottom half of population by cost function.
3. BREED survivors via assortative mating.
4. REPRODUCE where children inherit traits from parents at random.
5. MUTATION to ensure genes do not become stagnant.
6. Go to step 1 (with mutated children as new population).

WATCH THE MOVIE

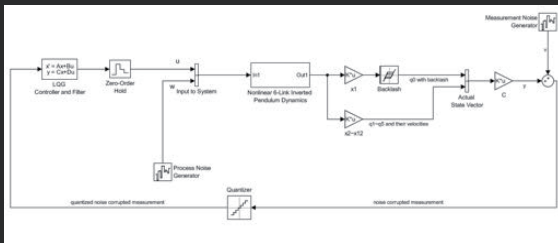
GENETIC ALGORITHM (GA) RESULTS

GA WITH MCBS: 1 DAY

GA WITH LMI: 3 MINUTES

SIMULATION OF 6-LINK INVERTED PENDULUM

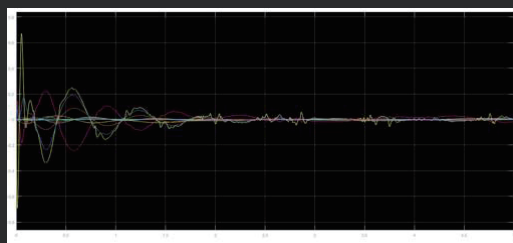
BLOCK DIAGRAM



13

SIMULATION RESULTS

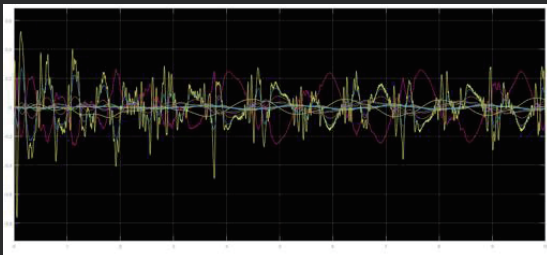
POSITIONS AND VELOCITIES OF JOINTS IN PENDULUM



14

SIMULATIONS ARE DOOMED TO SUCCEED

IF WE DECREASE THE ENCODER RESOLUTION/MOTOR DEADBAND...



15

CONCLUSIONS

1. *PEAK RESPONSE* as a design metric might be very useful proxy for ROA.
2. *QUANTIZATION* has a huge effect on robustness.
3. *OPTIMIZATION* is often unrealistic.

16

ACKNOWLEDGEMENTS

THANK YOU, JUACEP~
 THANK YOU, KATO SAN~

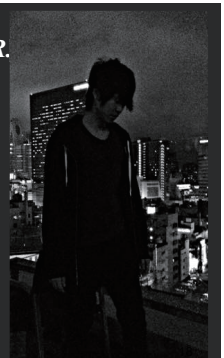
 THANK YOU, CSEL~
 THANK YOU, HARA SENSEI~
 THANK YOU, TSUBAKINO SENSEI~

17

SEE YOU LATER, SPACE ENGINEER.



HORIBE SAN
 HORIBE SAN
 HORIBE SAN
 HORIBE SAN
 HORIBE SAN
 HORIBE SAN



<3> Reports and Questionnaires on JUACEP

- (a) Findings through JUACEP
- (b) Questionnaires

(a) Findings through JUACEP

Findings through JUACEP

Name: Julian Zhou

Affiliation at home country : MAE UCLA

Participated program: Summer Course 2016

Research theme:

Probabilistic Methods in the Optimization of Nonlinear Control Systems

Advisor at Nagoya Univ.: Prof. Susumu Hara

Affiliation at Nagoya Univ.: Aerospace



I had a theory going into this experience that despite all of the “weird Japan” stuff that Americans always hear about that Japan would basically be exactly like America. And I was 100% right. The funny thing is that if you talk to anyone who has recently visited Japan they cannot stop going on about its ancient beauty, how elegant it is, how polite, shy, and eager to please its people are etc. It is like everyone agreed to be brainwashed by the same idiotic travel think piece.

You will find the same problems here that you find in America, or any other country. You will also find the same benefits. I can really only think of 3 essential differences. First, you can find cooler hoodies here. But that is just my taste in hoodies. Second, Japanese food is more available. Third, public transportation is better. Most importantly punk is great in Nagoya, just like it is everywhere, if you can find the right venues.

My point is that nothing I can say here should serve as an advertisement or criticism for visiting Nagoya or joining this program. You should go if you want to go. If you are like me, you would probably have a good time going. Also, Taka, my TA, was the best engineer I have ever worked with, so that was cool. Thanks for accepting me, JUACEP, say hi if you're ever in America.

Findings through JUACEP

Name: Carlos Alberto Gamez Villegas

Affiliation at home country: Mechanical and Aerospace Engineering,
Univerisy of California Los Angeles

Participated program: Summer Course 2016

Research theme: Temperature Dependent Thermal-Electrical-Structural Finite Element Analysis Around Crack Tip Under High Current Density Electropulsing.

Advisor at Nagoya Univ: Prof. Yasuyuki Morita

Affiliation at Nagoya Univ.: Mechanical Science and Engineering



I have never been outside of America, making this strip my first to a new continent. That is how my journey began, by visiting an entirely new continent. During my stay I was able to do multiple things in Japan. I was able to learn a little bit of Japanese (common phrases and also writing). My Japanese class helped me to understand Hiragana and Katakana, they don't look strange symbols to me anymore (my writing was not so good though). I learn also a lot of what makes Japanese culture so special. The coordinators of the program were keen to share their culture with us. They took us to Toyota Kaikan Museam, Toyota Factice and the Railway Park. We also build our own engine in one of our hands on workshops.

I was able to travel around as well. I visited Takayama, Gero, Shirakawa, Osaka, Nara, Kyoto and finally Tokyo. Every weekend was an adventure where I was able to taste the best food around and visit great landmarks of Japan. Sometimes the language barrier was difficult to overcome but all the people that we met did not give up on us, they were nice and patient. My lab mates always tried to include me in their celebrations, they were friendly and helpful. Overall, my all experiences had a great impression on me.

My experience on campus was memorable. Going to the gym so not as easy as I thought, I had to bring indoor shoes to enter it. The cafeteria is not full of food chains like the Food Courts in the United States. My relationship with my lab mates were pleasant. My limited Japanese and their limited English was an obstacle, but we were able to overcome it. In the academic side, I increased my knowledge on ABAQUS, now I am able to do a couple thermal-electric-structural analysis and export the results to do a failure analysis as well. With my new knowledge of XFEM in ABAQUS I am capable of simulating crack growth on 2D and 3D problems.

I'm almost done with my PhD program at UCLA and this trip influenced a lot on my formation as a PhD. The exchange of ideas between two different cultural backgrounds will help me to communicate better in the future. International collaboration is key to make leaps in our respective fields and making connections with people of other nations is not as difficult as I thought it was. I also learn more about ABAQUS, a tool that has a great value to a Mechanical Engineer.

I have must admit that I'm really happy that I was able to participate in the program. I was able to experienced great moments in Japan. I was happy the way we were treated by the staff and I also I was happy to have the opportunity to collaborate with people with a very different cultural background than mine. I was able to experience fist hand the Japanese culture at the same time I was able to conduct research. I recommend this program to anyone who wants to have a great balance of research and experience a new culture.

Findings through JUACEP

Name: Chen-Hsi Huang

Affiliation at home country (Dept & Univ): Materials department, UCLA

Participated program: Summer Course 2016

Research theme: Mechanical properties of lipid vesicle studied by
molecular dynamics simulations

Advisor at Nagoya Univ: Prof. Wataru Shinoda

Affiliation at Nagoya Univ. (Dept.): Applied chemistry



It is a very pleasant trip in Japan. I got more familiar about Japan culture. I visited many places including Nagoya, Kyoto, Nara, Matsumoto, Takayama, etc. I learnt the research style and lab life in Japan. The research style in Japan is not very different than the labs I have been worked in such as in Taiwan or US. The adviser and lab mates are very nice. I had a great time in the lab. I also learnt some Japanese, but I am still not able to use Japanese in communication. I'd probably need to take more Japanese courses to master it. Japanese are very polite. They are always concerned about making troubles to others. This is very different than in the US. Many cases when we say thank you in US become sumimasen in Japan. We also have more rules and take more serious in rules here in Japan.

The participation of JUACEP program makes me more familiar with Japan. For this, I'll definitely visit Japan again. Also, I'll consider apply for post-doc or jobs in Japan, but probably in bigger city such as Tokyo.

Japan, The Surprising Country

Name: Chang Chih-Kang

Affiliation at home country:

Robotics Program, University of Michigan

Participated program: Summer Course 2016

Research theme:

Intuitive user interface for surgical tool operation

Advisor at Nagoya Univ: Prof. Yasuhisa Hasegawa

Affiliation at Nagoya Univ.: Mechanical Engineering



Japan is a familiar and unfamiliar country for me. I am from Taiwan, where Japanese culture is very popular, and I have been in Japan for travel several times. However, this was my first time to stay in Japan for more than 2 weeks, and this time it was not only for fun.

Before I arrived, I was thinking about working as hard as possible to have a publication after 2 months (I heard someone really did this). However, the idea was soon blown away. Not only because I was assigned to a starting project which was impossible to have result in summer, but also because I was overwhelmed by the abundance of Japan. There were mountains, beaches, hot springs, world heritages and lots of other places where I could not stop myself from going. In 9 weekends I had, I have travelled for 5 of them and every time I was surprised by different spots I experienced. Just to list a part of them, the rustic shirakawago village relaxed my body, the royal Itsukushima Shrine moved my heart, and the sunrise on top of Mt. Fuji reminded me of the passion I had and pushed me to move on.

Let's come back to Nagoya. Though the research situation was not what I anticipated, I still made some process. One of my lab mates was from Peru and he spoke perfect English, while the other was Japanese who spoke poor English. It was very interesting to work with Japanese. Japanese people were very earnest. My lab mate would listen to me sincerely and tried his best to help. The results he showed on the meetings were highly completed even when it was just a weekly internal meeting. However, the academic environment seemed to be limited since everything was in Japanese and the students were not familiar with foreign materials.

During the 10-week program, besides gaining experience in research and technical skills, the biggest outcome was that I really enjoyed Japan. I travelled lots of fun places and knew some Japanese friends. I learned the delicate value of Japanese and practiced Japanese. Though I am not sure if I will be here again for study or work, I believe the international experience will bring me to a brighter future.

Findings through JUACEP

Name: Itsui Yamayoshi

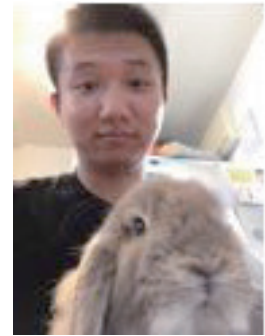
Affiliation at home country: Mechanical Engineering, UCLA

Participated program: Summer Course 2016

Research theme: Path Tracking using LIDAR Localization and Mapping

Advisor at Nagoya Univ: Prof. Tatsuya Suzuki

Affiliation at Nagoya Univ.: Mechanical Engineering



My experience in the JUACEP program has been a wonderful one. Being a Japanese born student who spent most of my life and education in the United States, it was a great and unique experience to be able to come to Japan and participate in research at a Japanese university and to immerse myself in the culture here. Although I was able to speak the language to a high level, I believe that I was able to garner a notable cultural education during my stay in Nagoya University. Through interactions with lab mates, professors, other JUACEP participants, and excursions that I participated in, I have improved my Japanese and have learned many new things about Japan that I did not know about before.

For the JUACEP program, I entered Professor Suzuki's lab to work on research using LIDAR to accomplish things such as SLAM (Simultaneous Localization and Mapping) and path tracking. I was able to work on and learn about many things I didn't know before. I learned Linux and ROS (Robotic Operating System) and learned to use them to receive data sent by the LIDAR. Then, I assisted in developing the communication between two computers so that the received data can be processed. From here, I worked with programs written in C# to accomplish the control of the COMS vehicle. Through all of this, I was able to accumulate new knowledge on programming, SLAM, and controls that I will be able to carry on to my future studies at UCLA.

Moreover, during my stay, I took the opportunity to attend some of the lectures taught at Nagoya University, including my own advisor's, and also attend the weekly seminars held by the lab. Although, I was not able to fully understand everything during lectures and seminars due to limitations in my Japanese, I believe that these experiences have cultivated a better foundation for me to work at a research or a professional environment in Japan for the future. On top of this, my interaction with other lab mates from both Japan and international backgrounds have fostered new friendships and memories that I will cherish.

In my time in Japan, I also had the fortune of traveling around outside of Nagoya. I was able to visit enthralling cities like Osaka, Kyoto, and Tokyo. I got to see the beautiful bamboo grove of Arashiyama, the shrine path filled with torii in Kyoto, the illuminated night life of Dotonbori, and the electrifying hubs of Shibuya, Roppongi, and Akihabara.

All in all, I have enjoyed my time in the program and appreciate the opportunity to be able to study, live, and travel in Japan. I would definitely recommend the program to those that are interested in Japan and want to see what life is like over here. I would also recommend it to anyone like me who may have been born in Japan but moved to another country and want to see what Japan is really like. Either way, it will be a terrific experience!

Findings through JUACEP

Name: Matthew Yee

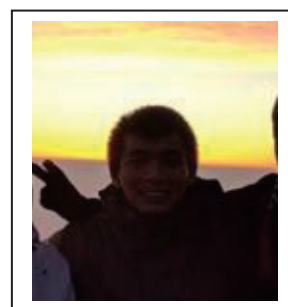
Affiliation at home country (Dept & Univ): UCLA Materials Science

Participated program: Summer Course 2016

Research theme: Carbon nanotube thin film transistors on flexible plastic substrates

Advisor at Nagoya Univ: Prof. Yutaka Ohno

Affiliation at Nagoya Univ. (Dept.): Electrical Engineering



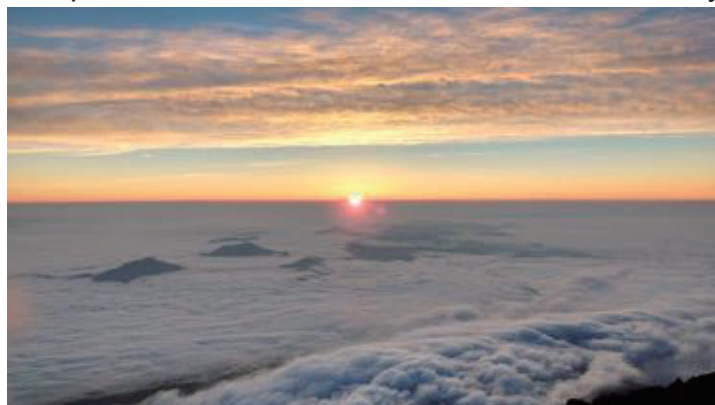
I've had an amazing time this summer while staying in Japan. It really was a unique experience to live in a foreign country and really be immersed into the culture through my research, Japanese course, and travels.

My research was with Professor Ohno working on carbon nanotube thin film transistors. This was an unfamiliar topic for me, but my TA was extremely helpful and patient with me and taught me everything I needed to know for my project. It was a lot of fun to get to know all of the different members of my lab. Sometimes there was a language barrier since their English and my Japanese left a lot to be desired, but all of them really made an effort to befriend me and make me welcome during my time here.

Nagoya was also a great city to live in. Although it isn't as big or iconic as cities such as Tokyo, Osaka, or Kyoto, it is still filled with a lot of interesting and fun places. Even in ten weeks, I feel as if there is still so much more of the city for me to see. The food in the city was also amazing and the Hitsumabushi was one of the best meals I've ever had.

I also had the chance to travel around Japan a little bit. I went to Kyoto, Osaka, Tokyo, and was even able to climb Mt. Fuji to see the sunrise from the summit. The trains and buses in Japan made it really easy to get around and it was actually pretty fun to ride the trains through the countryside.

It's hard to believe that the summer is almost over. I feel like I've been able to do so many different things and learn so much about Japanese language and culture, but there are also so many things that I still want to do. JUACEP has allowed me to make new friends, explore Japan, and learn about the culture and I am very thankful for that.



A Sizzling Summer Overseas

Name: Raymond Roman

Affiliation: Department of Mechanical & Aerospace Engineering, UCLA

Participated program: Summer Course 2016

Research theme: Effects of Stenting on Aneurysm Hemodynamics

Advisor at Nagoya Univ: Prof. Ito

Affiliation at Nagoya Univ: Mechanical Science & Engineering



Recently I spoke with a friend about how our lives were different five years ago versus today. I, for one, did not imagine I would spend my summer of 2016 in Japan of all places. In that span of time, I did not envision that I would spend quality time learning the Japanese language, much less spending an extraordinary summer overseas. I never even imagined that one of my summers while still in school would be spent in Nagoya finding beer gardens, making daily trips to Lawson, and expanding my Japanese speaking abilities with friendly strangers. I am immensely grateful to the JUACEP program for allowing me to breathe in the Japanese culture and experience it firsthand.

There were a couple cultural differences that were most apparent to me when arriving to Japan. The first thing that floored me when stepping off the subway was the cleanliness of Japanese streets, and actually every public place imaginable. Finding immaculately kept streets or roadways is unheard of and laughably unachievable in the booming metropolises across the Great Pacific. The other thing that struck me was the sheer density of Japanese convenience stores in a Japanese square kilometer. When learning about Japan, I somehow managed to gloss over the fact that Lawson convenience stores and 7 Eleven comprised the backbone of the average Japanese town. It seemed kind of fantastical to be able to get inexpensive snack foods that truthfully I've only ever really seen in anime.

My ten weeks in the JUACEP program was primarily filled with research. My research topic, under the guidance of Professor Ito, fused together the fields of physiology and fluid dynamics to investigate the precise behavior of blood when treating aneurysms with flow diverter stents. I took courses in biology for my bachelor's degree, so studying fluid dynamics through the lens of its clinical significance was probably the most interesting and eye-opening aspect of the research I performed. My approach to this research was through computational simulations, so learning the ins and outs of various computational software and gathering data for analysis ensured the ten weeks went by very quickly.

The Toyota factory tour also enriched my experience in the JUACEP program. Normally classrooms do not provide much in the way of hands-on participation, but the Toyota factory tour augmented my perspective of mechanical engineering and translated hundreds of pages of textbook material into things I can actually perceive.

Beyond my scholarly duties, my sightseeing explorations, though limited, were packed with quality. The most unforgettable one was visiting the Nagashima Spa Land amusement park where my thirst for ultimate thrill was happily quenched. While I've gone to plenty of amusement parks in the United States, thrill rides and coasters of the Japanese pedigree are light years ahead of what we have stateside. Riding the Steel Dragon 2000—the second fastest roller coaster in Japan!—was something of another world. I'm pretty sure it catapulted me into another dimension.

One lesson I unintentionally learned was that ten weeks is not enough time to explore the beauty and magnificence of the Land of the Rising Sun. I regret not exploring enough while staying these ten weeks; however, Nagoya seemed to have it all for me in the way of big town—small town vibes. It may have been the blindsiding humidity that aggrandized my summer torpor, but I personally lavished in exploring Nagoya and its quirks and novelties. Although I will return home when the sun sets on the Summer 2016 JUACEP program, I will definitely visit Japan again in the future (though probably during a season with less brutal weather).

Findings through JUACEP

Name: Sandeep Kumar Ingersal

Affiliation at home country: University of Michigan

Participated program: Summer Course 2016

Research theme: Study and control of chatter vibrations in milling operation

Advisor at Nagoya Univ: Prof. Shamoto

Affiliation at Nagoya Univ.: Ultra Precision Engineering Laboratory, Mechanical Science Dept.



I didn't hold any high expectation for the JUACEP program when I accepted it. I believe even if I had carried high expectations, the program would have met those definitely. There are two ways to experience a country. You land up with your bunch of friends or family, stay there for a fortnight, visit places and carry the memories created within your small circle. The other way (called the traveler way) is to stay in that place, talk to local people, live with them, feel their culture and learn their language where you create memories mainly through personal interaction with the local people rather than visiting tourist attractions. The latter provides the chance to create a healthy bonding and relationship with a country. The program almost equaled the latter one and it's the same way I wanted it to experience too. Being in the research program, I got the opportunity to work in the laboratory with all the Japanese Students and it kept me away from interacting with people I knew or know the language I speak. I value it as an important experience in this program.

Except to get fluent with the Japanese language, I felt 10 weeks of time were sufficient to experience the Japanese culture, to make friends and to visit important places. Japanese people were very courteous and friendly, and I felt that all the places in Japan were very welcoming for a foreigner because of its culture. Learning Japanese language during the first month of program was helpful in speaking common Japanese phrases with your lab mates and to the public. It helped us to get more social with the Japanese and enjoy our rest of the stay. My stay in the International Dorm was great and it had excellent facilities. I couldn't ask for anything better for the price we paid during our stay. I also visited world heritage places like Kyoto, Nara, Shirakawago.

Academically, the program showed a higher standard too. Nagoya University, being famous in Japan for its research, the research environment I experienced was testimony to its claim. My laboratory professors were very helpful and they framed a curriculum for me to follow which helped me to go in the right pace and right direction to make the best out of my research. I also did experiments with my lab mates to learn the concepts related to my research. Since I was working in an Industrial research project, I also had a chance to visit the AISIN factory to visually experience the technical problem at the field which is related to my research.

Overall, I had a great experience in Japan. I have gained some cross-cultural experience and have enriched by academic knowledge through my research experience in Japan. This study-abroad experience would not just stay on my resume but something that would influence me in my personal development process. Arigato Gozaimas!!

Findings through JUACEP

Name: Xiaojin Shen

Affiliation at home country: Nuclear Engineering and Radiological Science, University of Michigan

Participated program: Summer Course 2016



Research theme: Experimental measurement and numerical analysis for

the molten borosilicate glass with or without solid particles

Advisor at Nagoya Univ: Prof. Enokida and Associate Prof. Sugiyama

Affiliation at Nagoya Univ.: Quantum Science and Energy Engineering

JUACEP program motivates me to learn more about the nuclear waste reprocessing in the future study. I am very grateful that I was admitted to stay at Nuclear Chemical lab this summer supervised by Professor Enokida and Sugiyama. When I just entered this lab, I remembered that there were three undergraduate students working hard in front of their working desks. When they saw me, they smiled kindly. You may feel that they were too shy to introduce themselves in English directly, however after one week to fit in my labmate could start to talk with me and even gave me some help without asking, for example they taught me how to lock the door of our lab if I am the last person leave from the lab, some basic rules followed in our lab, or shared with me some Japanese cookies or sweets. The working atmosphere around this lab is hospitable. The relationship between our labmates and my host professor is very friendly. My host professor always makes jokes on one of my labmate Souta to have healthy food instead of cup ramen, and what's more since I came to this lab to study, every Monday morning seminar of our lab was held in English instead of Japanese. Thanks for the Japanese class, after this program in spite of the limited vocabulary storage, I am able to express myself in a few Japanese accurately and I will continue to study Japanese in the future and keep the friendships with my host professor and the labmates.

For the research side, I extended my potential involved the research related with nuclear waste reprocessing. I and my TA Uchimura are working on this project, even though our study has not finished to tell the whole story yet, we tried our best to investigate how the solid particles effected on viscosity of the borosilicate glassy melt. My research is related both with the experimental measurement and the computational fluid dynamics analysis, since I have little experience before with the composition analysis followed by alkaline fusion and X-Ray Diffraction method, my TA Uchimura helped me a lot with the experimental side, such as we diluted our glass samples together for more than ten times and helped me created the calibration curves for ruthenium and other Pd/Te metal elements, moreover, each glass samples for 50 milligrams was obtained from a homogenized discretized layer of the simulated borosilicate glass 900 grams, in the term of *homogenized* here, it needed a huge hammer work to crack the glass from block into the powder so that we did the hammer work in turn. Almost every week we arranged a meeting with my host professor Enokida, therefore my project was moving fast and productive. Finally, we made a breakthrough that we detected the ruthenium dioxide as one of the components in the glass powder we used successfully. Besides the experimental measurement, I simulated the inclined plane domain as a local interest for the nuclear waste melter in ANSYS/Fluent, another professor Sugiyama also gave me a lot of comments to accomplish my work. All in all, I am enthusiastic to do the research at Nuclear chemical lab. Our research needs time and patient, efforts and reflection to find the beauty of glasses.

Last but not least, the travel experience in Japan makes me to see this world more clearly. My host professor arranged a trip for me to Kyoto with my TA and Souta to join the Gion Matsuri festival. And during the Bon Holiday, I with my program friend climbed Mt.Fuji and attended the Hanabi Festival at the Suwa lake. You might probably be attracted by the colorful Japan – Green, yellow and blue... I found how small I was when I up to the top of the Mt.Fuji, I found the high civilian responsibility of Japanese when I got *lost*. I found how the firework beautiful in Japan, and it was the best firework show I have ever seen, you may appraise the art and elegance created from Japan. I

(b) Questionnaires

For Q1-4, we asked the same questions BEFORE and AFTER the program.

Q.1: Are you interested in studying at a Japanese university for PhD?



Q.2: Are you interested in working at a Japanese company in USA?



Q.3: Are you interested in working at a Japanese company in Japan?



Q.4: Are you interested in working at a non-Japanese company in Japan?



Q.5: In what did you find difficulty? What could be improved?

[Language barrier]

- As I already have English as a second language, Japanese was hard to me with memorizing new words and new writing system, although I really enjoyed.
- The hardest part of the program was adjusting to the new research topic. Although I had taken courses and performed research that was relevant to my topic, it was still difficult due to the language difference.
- Japanese class is very difficult.
- I wish there would be an intermediate Japanese course, as I believe that would have helped me improve my communicating abilities. Therefore, if there could be a class targeted at intermediate learners (provided there are enough Japanese language students at that ability for future programs), then that would probably be beneficial.

[Communication opportunity]

- I think that having a few more group activity or excursions would have been good. It was a great time for everybody to take a day off and hang out, talk to the JUACEP advisors, participate and experience new and interesting things.
- A bit lonely to live at the dorm and to go for shopping, since the amount of engineering female student is too limited.
- I hope that this program can provide more open lectures which are taught in English.

[Research circumstances]

- Academically, the program might fail if there is no strict curriculum or research agenda followed during the program. Fortunately, in my laboratory I had good support and academic assistance and I was also given a curriculum to follow. Because of that, I was able to learn much during my short period of stay. I hope all the professors to provide a curriculum or research agenda to the students to make the academic part of the program interesting and challenging. Though, students cannot contribute much to the research during this short stay but they can definitely learn something new out from their research here.

[Financial]

- If travelling expense is covered, it would encourage more students to participate in the program.

Q.6: Write comments freely.

- I especially liked the trip to Toyota. It was fun and informative.
- The 10-week program is well structured, we have time to do research and also have time for ourselves and enjoy the country.
- It was a great experience; it is going to help me in the professional level as well as the personal level.
- The Engine dis/assembly was great. Hope there are more such activities or excursion every two weeks until the end of the program but not just in the first month.
- Nice host professor I have, and the JUACEP program administrators, too.
- The excursion is a normal tour and we can do the same things by ourselves. I was looking for more unique and private tour which bring us to places where normal public could not enter or where I can make network.
- Although I needed so much help for pretty much everything due to language barrier, my lab members were kind and patient with me willing to help me out.
- During the excursion, I enjoyed the Toyota factory, but JR museum didn't interest me so much. It was repetitive and time allocation there was too long.
- Instead of three-hour train museum exploring, other museum or another factory would be a better alternative. (But keep the beer garden! That was excellent!)
- This was a wonderful program, and I am very grateful to have participated. I will definitely recommend this program to my classmates back at US.
- Please conduct many social events for the JUACEP students to bring in more interaction with the Japanese students other than the Laboratory environment.

<4> Appendix

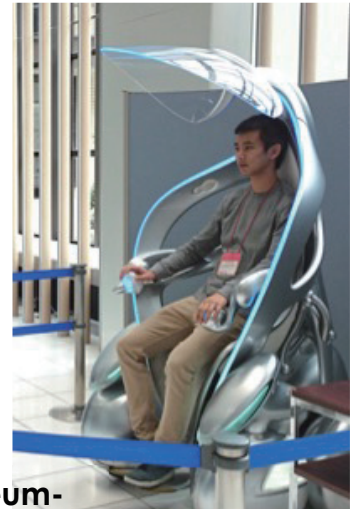
- (a) Photo Collection
- (b) Handout Materials

(a) Photo collection

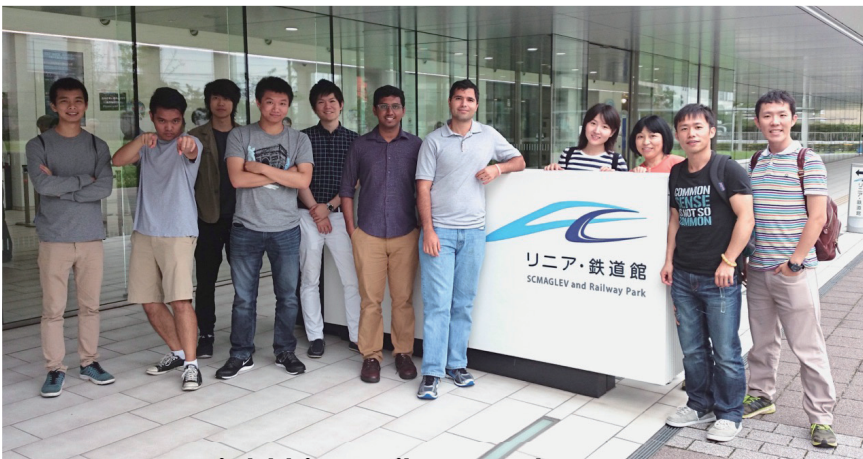
-Orientation & Luncheon with lab members-



-Disaster Mitigation Research Center tour-



-Field trip- Toyota Kaikan Museum-



-Field trip- Railway Park

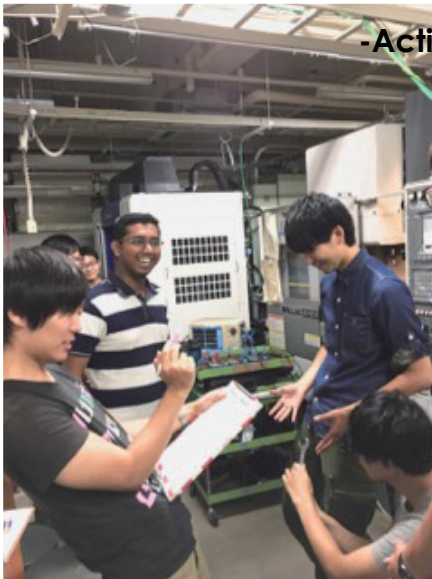


-Field trip- BBQ at Nayabashi Fish Market

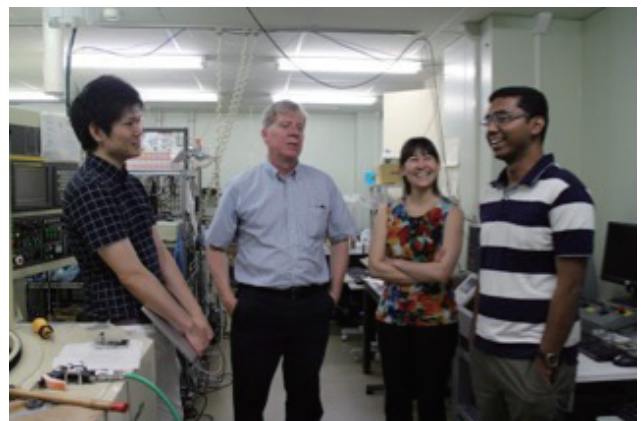
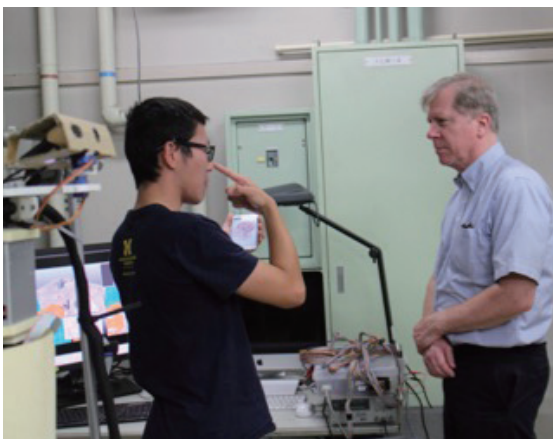
-Meet-up with Nagoya students-



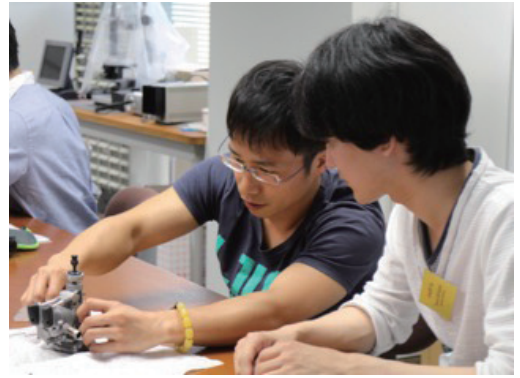
-Activities with the lab members-



-With UM visitors-

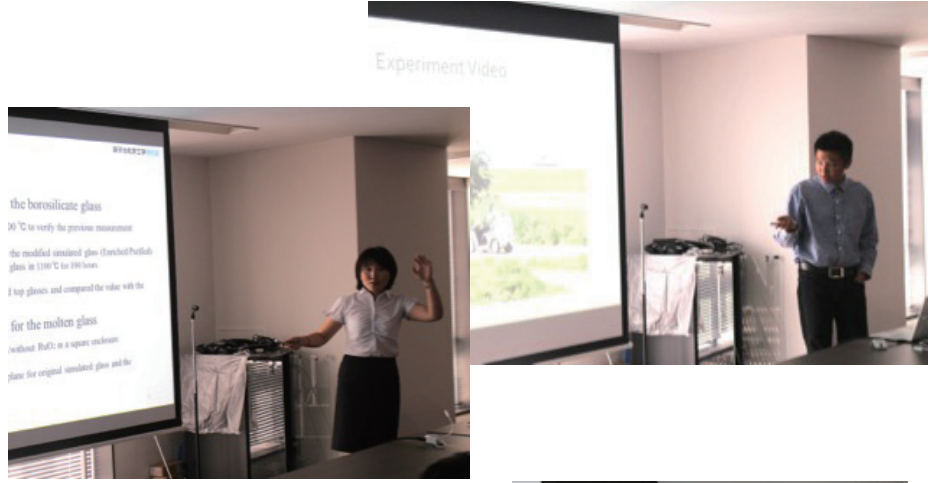


-Hands-on exercise for Internal Combustion Engine



-The 17th Workshop-





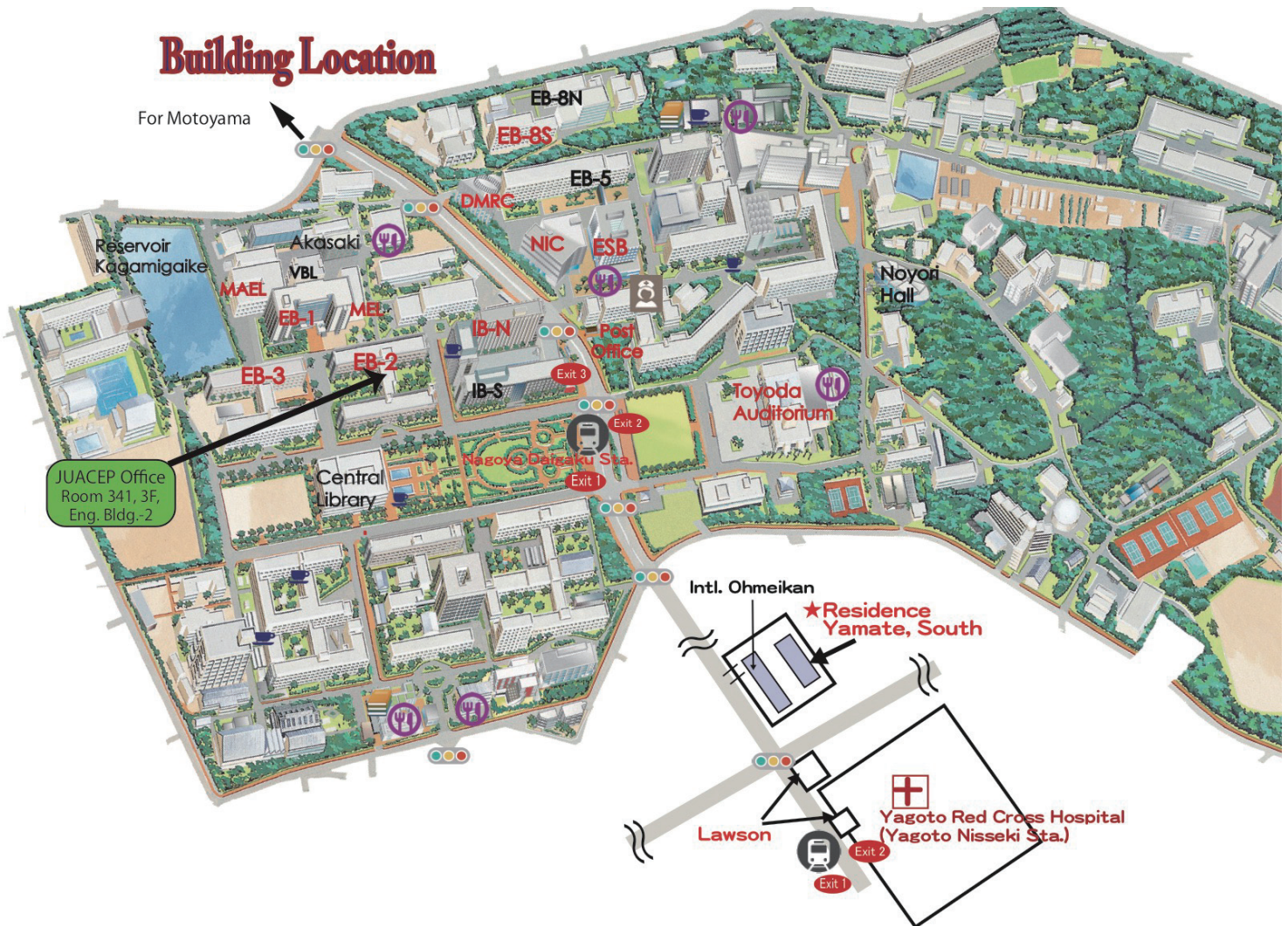
-Completion ceremony-



-Farewell party-



(b) Handout materials



Bldg. icon on the map	Building name (in Japanese)	Important places for JUACEP	Lab locations for JUACEP students
EB-1	Engineering Building 1 (Kougakubu ichi-gou-kan)		for Chen-Hsi
EB-2	Engineering Building 2 (Kougakubu ni-gou-kan)	JUACEP Office, Room 341, 3F	for Itsui, Carlos, Bonan, and Sandeep
EB-3	Engineering Building 3 (Kougakubu san-gou-kan)	Japanese Class, Room 441, 4F, 9:30am	for Matthew
EB-8S	Engineering Building 8 South (Kougakubu hachi-gou-kan, minami-kan)		for Xiaojin
MAEL	Mechanical & Aerospace Engineering Lab. (Kikai kouku jikkentou)		for Chih-Kang
MEL	Mechanical Engineering Lab. (Kikai jikkentou)		for Raymond
ESB	Engineering & Science Building (E-S kan)	Orientation of June 17, 1F	
NIC	National Innovation Complex (Nic)	17th Workshop of Aug. 26 at the Meeting Room, 3F	
IB-N	Integrated Building North (I-B Kita-kan)	Hands-on Execicis of July 20 & 21 at Creation Plaza, 10F, 1:00pm	
DMRC	Disaster Mitigation Research Center (Gensai-kan)	Facility tour of June 21, 1:00pm in front of the building	
Toyoda Auditorium	(Toyoda koudou)	Meeting point for the Field Trip of June 29, 9:00am	
Post Office		Money change, Money withdrawal, Postal affairs	
	Cafeteria/Convenience Shop		
	Café		
	Book Store		
	Subway Station	Nagoya Univ.: Nagoya Daigaku Station Dormitory Yamate: Yagoto Nisseki Station	
	Health Administration Office	Open hours: 9:00-12:00, 13:00-17:00, Mon.-Fri. (052)789-3970	

Mandatory Submittals

★ All of following templates are downloadable at

<http://www.juacep.engg.nagoya-u.ac.jp/downloads/index.html>

1. (For all students) JUACEP Independent research report

See Appendix-1.

Deadline: **August 23, 2016**

Submittal to... juacep-office@engg.nagoya-u.ac.jp

2. (For all students) JUACEP Research presentation slides

We will collect your PowerPoint slides at the workshop site, **Aug. 26, 2016**.

Evaluation: your final score is calculated by the points of the research report and the presentation at the workshop evaluated by your Nagoya Supervisor;

Research report (1~50pts.) + Presentation (1~50pts.) 100~90=S, 89~80=A, 79~70=B, 69~60=C, 59~0= fail

You will be officially awarded credits of Nagoya University and the transcript is airmailed to your home university in September 2016.

Important:

- (a) JUACEP will publish the participants' research reports and the presentation slides in the website and booklet. Please ask your supervisor if it is allowed to publish to the public and let us know the result.
- (b) UM students MUST transfer the credits to ME590/Engr591 and submit the transcript to JUACEP Office as soon as possible.

3. (For all students) Findings through JUACEP

See Appendix-2.

Deadline: **August 18, 2016**

Submittal to... juacep-office@engg.nagoya-u.ac.jp

Please write freely about your experience in Japan inserting pictures.

4. (For Scholarship students) JASSO Scholarship obligatory reports, H-2 & H-3

See Appendix-3 and -4.

Deadline: **August 18, 2016**

Submittal to... juacep-office@engg.nagoya-u.ac.jp

• H-2 "Completion report of "Student exchange support program"

Please write more than half of each column as it is required, then submit it without signature. We will request your autograph at a later date.

• H-3 "Questionnaire"

※ For H-2 and H-3, it is advised you leave out personal information which you do NOT want to share with the public as there is a possibility your report will be appeared on the JASSO website.

Campus Life Information

Housing

International Residence Yamate

Address: 165 Takamine-cho, Showa-ku, Nagoya 466-0811, Japan

Phone: (052) 835-5575 (Office) Office manger: Ms. Akiko Narita

Free WiFi is available.

Please follow the residential guidelines.

PC & ID

Student ID Card

A student ID card is issued. It will let you into the university libraries, and with the card you may borrow books from the library. The card lets you get student discounts at museums, theatres and so on.

Use of PCs on Campus See P.18 and P.19

Wireless Internet connection (NUWNET) is available on campus as far as your Nagoya University ID is effective. But at the beginning, you have to access to 'Information and Communications Headquarters' (<https://ist.nagoya-u.ac.jp/>) using your ID and a default password that are shown in the card delivered at the orientation, then take the online Information Security Training and pass the test. To pass the test, you must score at least 80% or repeat the test until you clear 80%. **Please do all of required steps described in the web like changing password, otherwise acquired wireless connection will expired in a week.**

University Security Department Warning

Copyright infringement using P2P software is prohibited. University has been strongly warning to all of faculty, staff and students not to use P2P software like Gntella, Share, Winny, WinMX, Xunlei, and so on. It can be easily detected and reflects discredit on University and oneself who used it.

Please never use P2P in University, nor PC in which P2P is installed accessing to University network.

Medical and Health Care

1. Medical Services

If you suffer from continuous headaches, a loss of appetite, or you cannot sleep well, etc., you should seek the advice of a doctor before the condition gets worse. These symptoms may be a sign of fatigue or exhaustion. They may also be psychological or psychosomatic symptoms, which are treatable by specialist doctors. In addition to taking care of your own health, please

pay attention to your friends' health and encourage them to see a doctor, if they are feeling unwell.

(1) The Health Administration Office See Building Location map.

Students can undergo physical examinations, receive health advice, first-aid and arrange psychiatric counseling at this facility. There is no charge for using any of these services. Appointments are necessary for psychiatric counseling services. Please call the office, Tel: (052) 789-3970

[Office Hours for Health Services]

Treatment	Time	Mon	Tue	Wed	Thu	Fri
Physical Examinations & First-Aid	10:00 - 11:30	○	○	○	○	○
	13:30 - 16:30	○	○	○	○	○
Psychiatric Counseling	10:00 - 12:00	○	○	○	○	○
	13:30 - 16:30	○	○	-	○	○

(2) Calling an Ambulance

Telephone 119 or press the RED button on a public phone for connection, free of charge. Although it is possible to speak English, it would probably be helpful for you to say the following: **“Kyuukyusha (ambulance) wo onegai shimasu. Basho wa (your location) desu.”** (I am calling for an ambulance. I am at...location.) This number is also used for requesting fire engines (**shoubousha**).

2. Precautions for Food Poisoning and Infectious Diseases

Great care should be taken with regard to eating habits during the extreme summer weather in Japan. To avoid food spoilage, check the expiration date before buying food, apply heat to raw foods and be careful not to keep food in the refrigerator for an excessive amount of time. To guard against food poisoning, always wash culinary items with hot water. Also follow the basic hygienic rules to avoid being infected.

World Health organization: <http://www.who.int/en/>

Student Life

1. Refuse Disposal at Nagoya University

A sorting system for refuse disposal is used at Nagoya University. There are trash bins for “combustible refuse”, “incombustible refuse”, and recycle bins for “empty bottles”, “empty cans”, and “PET bottles” all over campus. Papers or magazines are collected by recycle companies. Used paper products such as used copy paper are collected and recycled. Students are kindly

requested to be mindful when they throw away their rubbish and to use the correct bins to help waste reduction and the reuse of recyclable materials.

Also please follow the manners ruled in each laboratory.

2. Public Transportation of Nagoya City

(1) MANACA is a pre-paid pass that can be used for subway/ city bus/ most of train companies through Japan. It is also used at convenience shops, vending machines, some restaurants, and so on.

(2) ONE-DAY TICKETS allow for unlimited rides of city traffic for a day. One-day tickets for all bus, subway, and bus & subway routes are available. Ticket, Donichi-Eco-Kippu, that can be used on Saturdays, Sundays, holidays and the 8th of every month can be also purchased. These tickets include a discounted admission fee for some tourist facilities in Nagoya city such as Nagoya Castle or the Tokugawa Museum.

They can be purchased at any subway station. For further information, refer to the website: <http://www.kotsu.city.nagoya.jp/> (Japanese)

(3) Besides the city-running transportation, trains and buses of JR, Meitetsu, Aonami will make your movement easier.

Useful Links:

The following websites provide information on available transport services, time-tables, etc..

HYPERDIA: <http://www.hyperdia.com/en/>

3. If involved in a traffic accident.

If you are involved in a traffic accident, remain calm and do the following:

1. If anyone is injured, dial 119 for an ambulance.
2. Move any dangerous including vehicles, off the road to prevent other accidents.
3. Report the accident immediately, even if it is small, to a nearby police station and obtain a report of the accident.
4. Write down the license plate number of the car concerned as well as the name, address and age of the driver, after requesting to see his/her driver's license.
5. If there are witnesses, write down their names, addresses and telephone numbers.
6. Make detailed notes of the accident and take photographs, if possible.
7. See a doctor, even if you think that you are all right, because sometimes symptoms can take time to occur.
8. Consult your insurance company as soon as possible.

4. Compliance with Japanese Law

During their stay in Japan, any student who commits a crime, misdemeanor or any other illegal act, will be subject to legal procedures according to Japanese Law. Nagoya University also takes strict disciplinary measures against students who commit crimes or misdemeanors, and may expels them from university.

(1) Prohibition of Narcotics

In Japan, the possession and sale, for personal use or otherwise, of all narcotics and any illegal substances are strictly prohibited. If offered, refuse them. If leaving Japan temporarily, never agree to look after a stranger's luggage at the airport.

(2) Drinking and Smoking Restrictions

In Japan, people aged under 20 are not allowed to drink or smoke. Smoking is not allowed in many places, including stations, public facilities and within the campus. Nagoya city has special zones where smoking on the street is banned. If found smoking there, you will be fined.

Driving a car, riding a motorcycle or bicycle after drinking any amount of alcohol is a serious offence in Japan, and can also cause accidents. Never drive after drinking. Those who accept a ride in a car that is driven by a drunk driver or those who offer alcohol to a driver are all subject to punishment under Japanese law.

(3) Others

Whilst inside a shop, removing product wrappers, price tags or putting products into pockets or bags before actually paying for them may be treated as an attempt to shoplift in Japan. Talking loudly on your mobile phone or chatting loudly with friends in public places, such as on a train, can cause disturbance in Japan.

5. Safety Guide

Japan is not as safe as most people think. There is the risk of crime anywhere in the world, including Japan. Please pay attention to safety and security for yourself and your belongings in any scenes as you do in the US.

6. Culture shock

Although “culture shock” is generally understood as a temporary shock felt when confronted by different cultural customs, ways of thinking and behavior patterns, it actually refers to a psychological state of depression caused by a succession of failure experiences in unfamiliar social situations. Culture shock is temporary and everybody goes through it to some extent in the process of cultural adaptation. General symptoms of culture shock include negative feelings such as: losing self confidence, feeling depressed, attributing all failure to yourself, feeling that nobody understands you, feeling inadequate, etc. Accordingly, you may lose all motivation to talk with Japanese people or to attend classes. Most of these psychological reactions are, again, very natural in the process of cultural adaptation. Please take time to cope with each single event in your life, and you will be able to overcome these emotions sooner or later.

7. Differences in “Academic Culture”

It is widely accepted that different values, behavioral and communication patterns exist from culture to culture. However, we often fail to realize that there are also differences in “academic culture”, such as expected roles of academic advisers and students, classroom communication, evaluation criteria, etc. Such differences can also be a major cause of your stress. For example, the relationship between academic adviser and advisee is considered particularly important at the graduate level education in Japan. Some knowledge of the Japanese academic culture will help you achieve your goal more smoothly.

8. Cope with Stress

If you feel pressured by stress or lose confidence in your ability to study, you should think about releasing yourself from these negative emotions. Achieving good results in your studies may take a certain amount of time, and ought to be viewed as an accumulative process. Sometimes, you will need to take a break. If you feel tired, do not push yourself too hard and try to enjoy some of your favorite foods, recreation, and physical exercise. It is also recommended that you talk with your friends, academic adviser, or international students advisors/counselors. Moreover, please do not consider the process of cultural adaptation solely as a cause of stress; you can learn tremendously about various cultures, including your own, from this process.

< Visit the office of ECIS Advising & Counseling Services >

If you feel that you cannot deal with stress or feel a sense of isolation or frustration, do not hesitate to ask for help from international counselors at the ECIS Advising & Counseling Services. There is an international student counselor who will support your personal and psychological concerns. A discussion with an international student counselor can help achieve a useful perspective on culture shock and insights into Japanese culture.

ECIS Advising & Counseling Services (7th floor, West Wing of IB Bldg.)

<http://www.isa.provost.nagoya-u.ac.jp/en/>

9. Harassment

Nagoya University has set up a Harassment Consultation Center to prevent and eliminate the occurrence of any kinds of harassment, such as sexual harassment and academic harassment. Professional counselors deal with inquiries with utmost respect for their clients’ feelings and wishes. For English language consultation, you may visit the representative at the Education Center for International Students (ECIS). All consultation will be kept confidential.

Nagoya University Harassment Consultation Center (Appointments by fax or E-mail)

Tel: (052) 789-5806 (9:30-16:00)

Fax: (052) 789-5968

E-mail: sh-help@adm.nagoya-u.ac.jp

URL: <http://www.sh-help.provost.nagoya-u.ac.jp/> Contact persons at each School (including ECIS)

Hospitals around Nagoya University (English acceptable)

Nagoya Daini Red Cross Hospital (Yagoto Nisseki)

Address: 2-9 Myoken-cho, Showa-ku, Nagoya

Tel: (052) 832-1121

Mon-Fri: 8:00-11:00

Closed on Sat, Sun, holidays

Watanabe Clinic

Address: 1F Nikkou Yamate-dori Building, 3 -9-1 Yamate-dori, Showa-ku, Nagoya

Tel: (052)861-3450

Mon-Sat: 9:00-11:30

Mon, Wed-Fri: 16:00-17:30

Closed on Sun, holidays

Kai Clinic

Address: 32-2 Myoken-cho, Showa-ku, Nagoya

Tel: (052)836-9136

Mon-Sat: 9:00-12:00

Mon-Wed, Fri: 18:00-20:30

Closed on Sun, holidays

Yamate Dermatologist

Address: 2-9-1 Yamate-dori, Showa-ku, Nagoya

Tel: (052)836-4115

Mon, Tue, Thu-Sat: 9:30-12:30

Mon, Tue, Thu, Fri: 16:30-19:30

Sat: 14:30-17:30

Closed on Wed, Sun, holidays

Fujimi Dentist

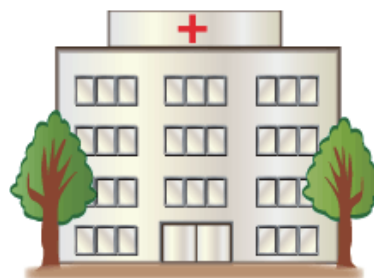
Address: 139 Yagotohujimi, Showa-ku, Nagoya

Tel: (052)835-3200

Mon-Wed, Fri, Sat: 9:30-12:30

Mon-Wed, Fri, Sat: 14:00-19:00

Closed on Thu, Sun, holidays



Copyright © JUACEP 2016 All Rights Reserved
Published in January 2017

Leading members of JUACEP

Professor Noritsugu Umehara

Professor Yang Ju

Associate Professor Yasumasa Ito

Japan-US Advanced Collaborative Education Program (JUACEP)

Graduate School of Engineering

Nagoya University  名古屋大学
NAGOYA UNIVERSITY

Furo-cho, Chikusa-ku, Nagoya 464-8603, Japan

JUACEP@engg.nagoya-u.ac.jp

<http://www.juacep.engg.nagoya-u.ac.jp>

